

SELF-SIMILAR FINITE-TIME BLOWUPS WITH SINGULAR PROFILES OF THE GENERALIZED CONSTANTIN–LAX–MAJDA MODEL: THEORETICAL AND NUMERICAL INVESTIGATIONS

DE HUANG¹, JIAJUN TONG², AND XIUYUAN WANG³

ABSTRACT. We investigate novel scenarios of self-similar finite-time blowups of the generalized Constantin–Lax–Majda model with a parameter a , which are induced by a new setting where the smooth initial data satisfy certain derivative degeneracy condition. In this setting, our numerical study reveals distinct self-similar blowup behaviors depending on the sign of a . For $a > 0$, we observe one-scale self-similar blowups with regular profiles that have not been found in previous studies. In contrast, for $a \leq 0$, we discover a novel two-scale self-similar blowup scenario where the outer profile converges to a singular function at the blowup time while the inner profile remains regular on a much smaller scale. Correspondingly, an a -parameterized family of singular self-similar profiles with explicit expressions are constructed for $a < 0$ and shown to match nicely with the limiting profiles obtained in numerical simulation. In particular, for the specific case of $a = 0$, we rigorously prove the convergence of the outer profile to an explicit singular function in self-similar coordinates. Furthermore, we demonstrate the two-scale nature of the blowup in this scenario by showing that the local inner profile behavior around the singularity point of the outer profile is governed by a traveling wave on a smaller scale. To support this observation, we rigorously establish the existence of such traveling wave solutions via a fixed-point method.

1. INTRODUCTION

We consider the 1D generalized Constantin–Lax–Majda (gCLM) equation

$$\omega_t + a u \omega_x = u_x \omega, \quad u_x = \mathbf{H}(\omega), \quad (1.1)$$

for $x \in \mathbb{R}$, where $\mathbf{H}(\cdot)$ denotes the Hilbert transform on the real line. This equation is a 1D model for the vorticity formulation of the 3D incompressible Euler equations, proposed to study the competitive relation between advection and vortex stretching. In particular, ω models the vorticity, and the nonlinear terms $u \omega_x$ and $u_x \omega$ model the advection term and the vortex stretching term, respectively. The 3D Biot-Savart law that recovers the velocity from the vorticity is modeled by $u_x = \mathbf{H}(\omega)$, which has the same scaling as the original Biot-Savart law.

The fundamental question on the global regularity of the 3D Euler equations with smooth initial data of finite energy remains one of the most challenging open problems in fluid dynamics. It is widely believed that the vortex stretching effect has the potential to induce an infinite growth of the vorticity in finite time. The first construction of a (stable) self-similar finite-time blowup for the 3D incompressible Euler equations on \mathbb{R}^3 was established by Elgindi [Elg21] in the axisymmetric setting from $C^{1,\alpha}$ initial velocity for sufficiently small α (with stability of the blowup discussed in [EGM21]). Under some change of variables, the $C^{1,\alpha}$ regularity of the solution gives rise to a small coefficient α in the advection term that weakens its effect, which is similar to the role of the parameter a in (1.1). Later, Chen and Hou [CH22, CH25] employed rigorous computer-assisted proof to show for the first time that the 3D vortex stretching can actually dominate the advection and lead to an asymptotically self-similar finite-time singularity from smooth initial data in the presence of a solid boundary. Recently, Cordoba et al. [CMZZ25] also constructed a finite-time blowup of the axisymmetric incompressible Euler equations

¹ School of Mathematical Sciences, Peking University. Email: dhuang@math.pku.edu.cn.

² Beijing International Center for Mathematical Research, Peking University. E-mail: tongj@bicmr.pku.edu.cn.

³ School of Mathematical Sciences, Peking University. Email: wangxiuyuan@stu.pku.edu.cn.

from $C^{1,\alpha}$ initial velocity for small α . Instead of relying on self-similarity, they constructed the finite-time blowup in a novel way by manipulating an infinite cascade of vorticity. However, whether a finite-time singularity can happen for the 3D incompressible Euler equations from smooth initial data in the free space \mathbb{R}^3 still remains open. Nevertheless, Hou and Huang [HH22] presented numerical evidence of a potential self-similar finite-time blowup of the 3D Euler equations from smooth initial data. In particular, the self-similar solution they discovered exhibits a two-scale feature in the sense that the outer profile becomes more and more singular while the local inner profile remains smooth on a much smaller spatial scale. The mechanism of this self-similar blowup has not been fully understood. Therefore, it is still worthwhile to explore more sophisticated mechanisms that lead to novel self-similar finite-time blowups from smooth initial data for simplified models of the 3D Euler equations such as the gCLM model.

The original version of (1.1) with $a = 0$ was proposed by Constantin, Lax and Majda [CLM85] to demonstrate that a non-local vortex stretching term can lead to finite-time blowup in the absence of advection. Later, De Gregorio [DG90] included an advection term $u\omega_x$ back in the equation (known as the De Gregorio model) and conjectured the occurrence of a finite-time singularity none the less. As a generalization, Okamoto, Sakajo and Wunsch [OSW08] introduced the real parameter a to modify the effect of advection in the competition against vortex stretching. Hence, equation (1.1) is also referred to as the Okamoto–Sakajo–Wunsch (OSW) model.

Motivated by the long-standing problem on finite-time blowup of the 3D incompressible Euler equations, finite-time singularity formation of the gCLM model for a wide range of a has been studied extensively in the literature. In view of the scaling property of equation (1.1), we are particularly interested in finite-time blowups that take the self-similar form

$$\omega(x, t) = (T - t)^\lambda \cdot \bar{\Omega} \left(\frac{x}{(T - t)^\gamma} \right), \quad (1.2)$$

where $\bar{\Omega}$ is referred to as the self-similar profile, and λ, γ are the scaling factors. Plugging the ansatz into (1.1), assuming that $\bar{\Omega}$ is sufficiently regular, and taking $t \rightarrow T^-$ yields that the only possible non-zero value for λ is -1 , which corresponds to the quadratic non-linearity in vortex stretching. The value of γ determines the spatial feature of the blowup: A positive γ corresponds to a spatially focusing blowup at $x = 0$, while a negative γ corresponds to an expanding blowup. The existence of self-similar finite-time blowups of (1.1) have been established for a wide range of the parameter a in the literature [CC09, EJ20, LSS21, Che20, CHH21, HTW23, HQWW24, WBM⁺25]. Note that an exact self-similar solution as in (1.2) means that the initial condition $\omega(x, 0)$ is already a rescaling of the self-similar profile $\bar{\Omega}$, which is not favorable if $\bar{\Omega}$ is not smooth or does not decay sufficiently fast in the far field. In order to construct singularity formation for more general initial data (especially for smooth ones), we need to study self-similar finite-time blowups in an asymptotic sense that

$$\omega(x, t) = (T - t)^{-1} \cdot \Omega \left(\frac{x}{(T - t)^\gamma}, t \right), \quad (1.3)$$

where $\Omega(X, t) \rightarrow \bar{\Omega}(X)$ as $t \rightarrow T^-$ for some exact self-similar profile $\bar{\Omega}$. More rigorously, we say that ω develops an asymptotically self-similar blowup (with $\lambda = -1$) at some finite time $T \in (0, +\infty)$, if

$$\lim_{t \rightarrow T^-} (T - t) \cdot \omega((T - t)^\gamma X, t) = \bar{\Omega}(X)$$

for some $\gamma \in \mathbb{R}$ and some (limit) profile function $\bar{\Omega}$. Naturally, an asymptotically self-similar blowup requires not only the existence of a profile $\bar{\Omega}$ but also its stability in some sense. One common way to accomplish this is by applying a time-dependent change of variables that transforms the gCLM equation (1.1) into a dynamic equation of the profile $\Omega(X, t)$ and then studying the evolution and potential convergence of $\Omega(X, t)$. This approach is usually referred to as the dynamic rescaling method.

Stability of self-similar profiles of the gCLM model has been established in a few special cases; see [EGM21, CHH21, Che20]. We refer to [EJ20] and [HQWW24] for a more comprehensive review on related results.

It is worth noticing that stable self-similar blowup profiles of the gCLM model that have been obtained in previous research so far are interiorly smooth or at worst Hölder continuous. This naturally raises the question whether the gCLM equation can also develop self-similar finite-time blowups with singular profiles (not in L^∞) from smooth initial data. We remark that earlier works typically assume that the initial solution $\omega_0 = \omega(\cdot, 0)$ is odd symmetric (which helps to locate the blowup at the symmetry point $x = 0$) and has non-zero derivative at the expected blowup point, i.e. $\omega'_0(0) \neq 0$. We will refer to such initial data as *non-degenerate* initial data in the sequel. In contrast, we call an initial datum *degenerate* if ω has zero first derivative at the eventual blowup point. *The main purpose of this paper is to find out whether and how self-similar blowups can develop from degenerate initial data and in what ways they are different from those in the non-degenerate case.*

Our numerical investigation in this problem reveals a whole new picture of more complicated blowup behavior of the gCLM model (1.1). For $a > 0$, we observe that smooth degenerate initial data could lead to asymptotically self-similar finite-time blowups with undiscovered regular profiles that share the same type of derivative degeneracy as the initial data. As far as we know, such degenerate self-similar profiles of the gCLM model have not been reported in the literature before. More interestingly, for $a \leq 0$, we find that *smooth degenerate initial data can lead to asymptotically self-similar finite-time blowups with singular profiles* in the sense that the profile $\Omega(X, t)$ in (1.3) not only still converges in some sense but also becomes infinitely large at a certain point as $t \rightarrow T^-$ (therefore $\bar{\Omega}$ not in L^∞). This new self-similar blowup phenomenon is remarkably different from all the previously studied self-similar blowups with non-degenerate initial data and therefore broadens our understanding of finite-time singularity formation for models of the Euler equations. In Figure 1.1, we compare the formation of a regular self-similar profile (Figure 1.1(c)) in the development of a blowup to that of a singular self-similar profile (Figure 1.1(d)). Note that an asymptotically self-similar blowup of the form (1.3) with a singular (limit) profile implies that, even though the overall blowup of ω is at the scale of $(T - t)^{-1}$, the maximum of $|\omega|$ actually blows up much faster than $(T - t)^{-1}$, which is not typical in view of the quadratic non-linearity of the equation. Such non-typical growth of ω in the gCLM model has been rigorously constructed in [HQW25] for $a = 0$ and is now observed for all $a < 0$.

At the theoretical level, we construct a family of singular self-similar profiles $\bar{\Omega}_a$ with explicit expressions parameterized by a for $a \leq 0$, each of which gives an exact self-similar solution of the form (1.2) (though in this case ω can only be understood as a weak solution). For the special case $a = 0$, we can additionally prove the convergence of the profile function $\Omega(X, t)$ to the self-similar profile $\bar{\Omega}_a$. As for all $a < 0$, our numerical simulation further shows that, with a particular setting of the initial data (that will be made clearer in Section 2), the profile $\Omega(X, t)$ in (1.3) will converge to $\bar{\Omega}_a$ as $t \rightarrow T^-$. With the explicit expressions of $\bar{\Omega}_a$ in hand, it is possible to follow the methods in [EGM21, CHH21, Che20] to theoretically prove the stability of $\bar{\Omega}_a$ and therefore rigorously establish asymptotically self-similar finite-time blowups with singular profiles for all $a < 0$. We will leave this to future works.

Moreover, for $a \leq 0$, if we zoom in around the singularity point of the (outer) profile $\Omega(X, t)$, we observe another inner (smaller) scale of the solution with an inner profile. That is, the solution has a two-scale behavior. Let the larger scale be denoted by $(T - t)^\gamma$, and let the trajectory of the maximum point of $|\omega|$ be given by $x = r(t)(T - t)^\gamma$ for some function $r(t)$. Zooming in around that point, we observe that the inner profile after properly rescaled in magnitude remains regular on a secondary spatial scale denoted by $(T - t)^{\hat{\gamma}}$ with some $\hat{\gamma} > \gamma$. In other words, for $x = r(t)(T - t)^\gamma + O((T - t)^{\hat{\gamma}})$

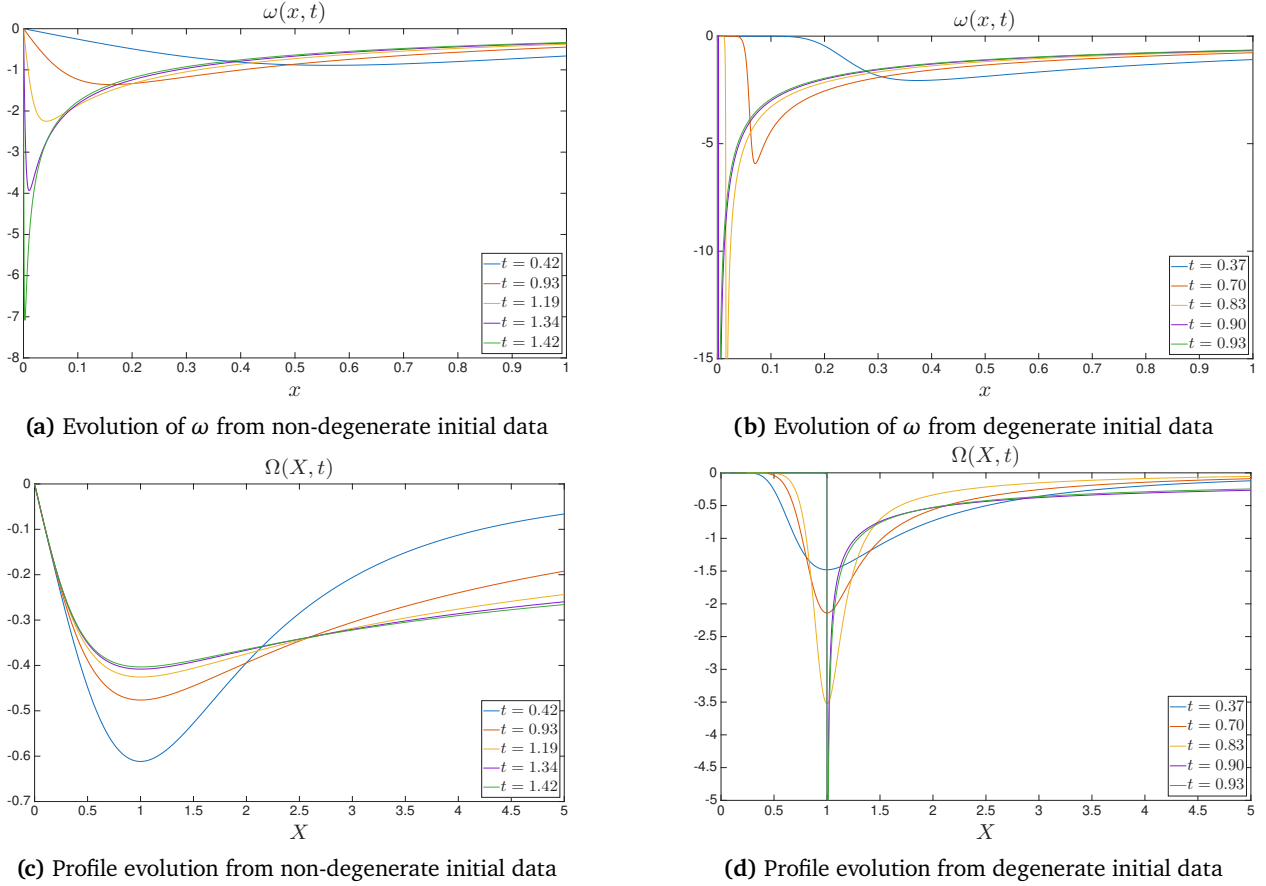


Figure 1.1: First row: Evolution of ω (in original spatial coordinate) for $a = -1$ (a) with non-degenerate odd-symmetric initial data and (b) with degenerate odd-symmetric initial data, respectively. Second row: Corresponding evolution of the profile (in dynamically rescaled coordinate) for $a = -1$ (c) with non-degenerate odd-symmetric initial data and (d) with degenerate odd-symmetric initial data, respectively. A regular profile arises from non-degenerate initial data, while a singular profile with singularities at $X = \pm 1$ arises from degenerate initial data. Here $X = x/(T - t)^\nu$ is the dynamically rescaled spatial variable. Only the parts for $x \geq 0$ (or $X \geq 0$) are plotted due to the odd symmetry.

the solution behaves like

$$\omega(x, t) = (T - t)^{\hat{\lambda}} \left(\widehat{\Omega} \left(\frac{x - r(t)(T - t)^\nu}{(T - t)^\nu} \right) + o(1) \right) \quad (1.4)$$

for some regular inner profile $\widehat{\Omega}$ and some $\hat{\lambda} < -1$. The observation $\hat{\lambda} < -1$ indicates that the maximum of $|\omega|$ grows faster than $(T - t)^{-1}$, i.e. $\lim_{t \rightarrow T^-} (T - t) \cdot \|\omega(\cdot, t)\|_{L^\infty} = +\infty$, which is sometimes referred to as a Type II blowup in the literature. By a formal asymptotic analysis, we show that the inner profile (if exists) must be an exact traveling wave solution of the gCLM model (1.1). To support our observation and analysis of this two-scale blowup phenomenon, we also prove the existence of such traveling wave solutions for all $a < 1$ via a fixed-point approach. We remark that for the original CLM model ($a = 0$), the two-scale self-similar blowup (1.4) has been rigorously established in [HQW25]. However, how the outer profile Ω behaves as $t \rightarrow T^-$ was not discussed in [HQW25] but will be rigorously addressed in this paper. Moreover, this two-scale self-similarity setting (1.4) was also adopted in [HH22] for understanding the numerically observed potential two-scale self-similar blowup of the axisymmetric incompressible Euler equations in \mathbb{R}^3 . In fact, locally self-similar blowups with two-scale features

as in (1.4) have been studied and established as Type II blowups in other PDE systems such as the Keller–Segel system [CGMN23] and the semilinear heat equation [dPMWZ20, dPLM⁺20]. We hope that our numerical simulation of self-similar blowups with singular profiles and two-scale feature will in the future turn into a rigorous proof and in the end help us construct finite-time blowups of the incompressible Euler equations from smooth initial data in \mathbb{R}^3 .

The main contributions of this paper are the followings.

(1) Theoretical aspect:

- For the case $a = 0$ with degenerate initial data, we prove the convergence of the (outer) profile to an exact singular function under certain assumptions and normalization conditions, thereby establishing an asymptotically self-similar blowup in the form of (1.3) with a singular profile in this case. (Theorem 2.4 and Corollary 2.5)
- For $a < 0$, we construct a family of exact self-similar solutions in the form of (1.2) with explicit singular profiles $\bar{\Omega}_a$ parameterized by a . (Theorem 2.6)
- We prove the existence of traveling wave solutions for the gCLM model for all $a < 1$ using a fixed-point method. (Theorem 2.7)

(2) Numerical aspect:

- For $a > 0$, we show that degenerate initial data can lead to self-similar finite-time blowups with regular profiles that have the same type of degeneracy.
- For $a < 0$, we show that degenerate initial data can lead to self-similar finite-time blowups with singular profiles. In a particular setting, we show that the profile converges to $\bar{\Omega}_a$.
- We provide numerical evidence of the two-scale behavior of self-similar blowups for $a < 0$ with degenerate initial data, and we show that the inner profile on a smaller scale converges to a traveling wave solution.

The remainder of this paper is organized as follows. In Section 2, we introduce the dynamic rescaling framework, review previous results on self-similar blowups with non-degenerate initial data, and present new blowup scenarios involving singular profiles arising from degenerate initial data. We also discuss the multiscale structure of these solutions and show that the inner profile converges to a traveling wave. Section 3 proves that for $a = 0$ with odd degenerate initial data, the profile converges to an exact singular solution under certain assumptions. Section 4 details the numerical computations and convergence analysis for one-scale blowups from degenerate initial data when $a > 0$. Section 5 presents numerical evidence that, for $a < 0$, degenerate initial data can lead to finite-time blowup with a singular self-similar profile. Section 6 investigates the associated two-scale behavior for $a < 0$, including a comparison between numerically extracted inner profiles and traveling wave solutions, as well as a scaling analysis of the two-scale blowup. In Section 7, we prove the existence of traveling wave solutions for the gCLM model using a fixed-point method and derive regularity and tail estimates for these solutions. Finally, technical lemmas and details of the numerical implementation are provided in the appendices.

2. DYNAMIC RESCALING FORMULATION AND SELF-SIMILAR BLOWUPS OF THE GCLM MODEL

We first review the dynamic rescaling method and its application to self-similar finite-time blowups of the gCLM model (1.1). Based on this method (and its variation), self-similar blowups with non-degenerate odd symmetric regular profiles have been found for a wide range of parameter a . We then introduce novel self-similar blowup scenarios of the gCLM model arising from degenerate initial data (to be clarified later). Most interestingly, when $a \leq 0$, this new class of self-similar blowups are featured by singular self-similar profiles and locally two-scale behavior.

Before we proceed, we clarify how to recover u from ω in the gCLM equation (1.1). The first step is to determine u_x from ω by the Hilbert transform:

$$u_x(x, t) = \mathbf{H}(\omega)(x, t) = \frac{1}{\pi} \text{P.V.} \int_{\mathbb{R}} \frac{\omega(y, t)}{x - y} dy. \quad (2.1)$$

Then we recover u from u_x by integrating. One way to do this is to formally write

$$u(x, t) = -(-\Delta)^{-1/2} \omega(x, t) = \frac{1}{\pi} \int_{\mathbb{R}} \log|x - y| \omega(y, t) dy$$

which, however, may not be well-defined if ω does not decay fast enough at infinity. An alternative way is to fix a point x_0 where $u(x_0, t) = 0$ for all time t , which gives

$$u(x, t) = \int_{x_0}^x H(\omega)(y, t) dy = \int_{\mathbb{R}} \ln \left| \frac{x - y}{x_0 - y} \right| \omega(y, t) dy.$$

In particular, when ω is odd, a natural choice (as commonly used in previous works) is to set $x_0 = 0$, thus making u also an odd function. We remark that the choice of x_0 does not essentially affect the behavior of the solution; that is, solutions with the same initial data but different choices of x_0 are equivalent under a time-dependent translation. We will rigorously argue this in Appendix A. Therefore, for simplicity, we fix $x_0 = 0$ throughout this paper, which yields

$$u(x, t) = \int_{\mathbb{R}} \ln \left| \frac{x - y}{y} \right| \omega(y, t) dy. \quad (2.2)$$

2.1. Self-similar finite-time blowup via the dynamic rescaling method. One important way to study and construct self-similar finite-time blowups is by considering the dynamic rescaling formulation. The idea of dynamic rescaling was introduced in [LPSS88, MPSS86] to study self-similar blowups of the nonlinear Schrödinger equations. A combination of the dynamic rescaling method and the method of computer-assisted proof has been successfully applied to proving self-similar finite-time blowups with smooth initial data for the De Gregorio model [CHH21] ((1.1) with $a = 1$), the 1D Hou–Luo model [CHH22], and the 3D axisymmetric incompressible Euler equations with boundary [CH22, CH25].

We will explain in detail how to apply the dynamic rescaling method to studying self-similar finite-time blowups of the gCLM model (1.1). To be specific, we consider the following time-dependent change of variables

$$\omega(x, t) = C_\omega^{-1} \Omega(C_l x, \tau(t)) \quad (2.3)$$

where

$$C_\omega(\tau) = \exp \int_0^\tau c_\omega(s) ds, \quad C_l(\tau) = \exp \int_0^\tau c_l(s) ds \quad (2.4)$$

are cumulative scaling factors representing the magnitude blowup of ω and the spatial scale of the blowup, respectively. The relation between the dynamic rescaling time τ and the physical time t will be determined soon below. This change of variables rescales the solution with the hope that the profile function Ω will have a more stable behavior if the dynamic rescaling factors $c_\omega(\tau)$ and $c_l(\tau)$ are chosen properly, e.g. via some normalization conditions. Through this change of variables, studying the self-similar finite-time blowup of $\omega(x, t)$ boils down to studying the evolution of the $\Omega(X, \tau)$. In fact, substituting (2.3) into the gCLM equation (1.1) yields

$$C_\omega^{-1} \Omega_\tau \tau_t - c_\omega C_\omega^{-1} \Omega \tau_t + c_l C_\omega^{-1} X \Omega_X \tau_t + a C_\omega^{-2} U \Omega_X = C_\omega^{-2} U_X \Omega,$$

where $X = C_l x$, $U_X = H(\Omega)$, and in view of (2.2),

$$U(X, \tau) = \int_{\mathbb{R}} \ln \left| \frac{X - Y}{Y} \right| \Omega(Y, \tau) dY. \quad (2.5)$$

Simplifying the above equation gives

$$(\Omega_\tau + c_l X \Omega_X - c_\omega \Omega) \tau_t = C_\omega^{-1} (U_X \Omega - a U \Omega_X).$$

To balance the profile equation, it remains to define the dynamic rescaling time τ by

$$\tau'(t) = C_\omega(\tau)^{-1} = \exp \int_0^\tau -c_\omega(s) ds, \quad (2.6)$$

which implicitly determines the relation between physical time t and the dynamic rescaling time τ . With this definition of τ , we arrive at the famous dynamic rescaling equation of the gCLM model

$$\Omega_\tau + (c_l X + a U) \Omega_X = (c_\omega + U_X) \Omega, \quad U_X = \mathbf{H}(\Omega). \quad (2.7)$$

We remark that (2.7) is completely equivalent to (1.1) under the change of variables given by (2.3), (2.4), and (2.6) with the same initial condition $\Omega(X, 0) = \omega(x, 0)$. We will use Ω_0 and ω_0 to denote initial data in what follows.

We are also particularly interested in steady state solutions to (2.7) that satisfy the self-similar profile equation

$$(\bar{c}_l X + a \bar{U}) \bar{\Omega}_X = (\bar{c}_\omega + \bar{U}_X) \bar{\Omega}, \quad \bar{U}_X = \mathbf{H}(\bar{\Omega}), \quad (2.8)$$

where \bar{U} is related to $\bar{\Omega}$ as in (2.5). One can easily verify that if $(\bar{\Omega}, \bar{c}_l, \bar{c}_\omega)$ is a solution to (2.8), then it gives an exact self-similar finite-time blowup solution to the gCLM model in the form of (1.2) with $\lambda = -1$ and $\gamma = -\bar{c}_l/\bar{c}_\omega$. Note that if $(\bar{\Omega}(X), \bar{c}_l, \bar{c}_\omega)$ is a solution to (2.8), then

$$(\alpha \bar{\Omega}(\beta X), \alpha \bar{c}_l, \alpha \bar{c}_\omega) \quad (2.9)$$

is also a solution for any $\alpha \in \mathbb{R}, \beta > 0$, which indicates that this equation admits two degrees of freedom. Hence, in order to uniquely identify the profile up to rescaling, we need to impose two normalization conditions to fix these two degrees of freedom.

Moreover, if under some normalization conditions the solution tuple (Ω, c_l, c_ω) converges to a steady state $(\bar{\Omega}, \bar{c}_l, \bar{c}_\omega)$ of (2.7) as $\tau \rightarrow +\infty$, then the solution $\omega(x, t)$ would blowup in an asymptotically self-similar manner (1.3). We demonstrate this more precisely by the following proposition.

Proposition 2.1. *Assume the solution (Ω, c_l, c_ω) to (2.7) converges to a steady state $(\bar{\Omega}, \bar{c}_l, \bar{c}_\omega)$ (a solution of (2.8)) with $\bar{c}_\omega < 0$ as $\tau \rightarrow +\infty$. In particular, assume the convergence of Ω is locally uniform, the limiting profile $\bar{\Omega}$ is continuous, and the scaling factors c_l, c_ω converge sufficiently fast such that*

$$\int_0^{+\infty} |c_l(\tau) - \bar{c}_l| d\tau < +\infty, \quad \int_0^{+\infty} |c_\omega(\tau) - \bar{c}_\omega| d\tau < +\infty.$$

Then the solution $\omega(x, t)$ develops an asymptotically self-similar blowup at the origin in the sense that

$$\lim_{t \rightarrow T^-} (T - t) \cdot \omega((T - t)^\gamma X, t) = \frac{1}{|\bar{c}_\omega|} \bar{\Omega}(C_0 X)$$

for some constant $C_0 > 0$, where $\gamma = -\bar{c}_l/\bar{c}_\omega$ and $T < +\infty$ is the finite blowup time given by

$$T = \int_0^{+\infty} \left(\exp \int_0^\tau c_\omega(s) ds \right) d\tau.$$

Proof. By the assumption on the convergence of $c_\omega(\tau)$, we have

$$C_\omega(\tau) = \exp \left(\bar{c}_\omega \tau + \int_0^\tau c_\omega(s) - \bar{c}_\omega ds \right) \lesssim \exp(\bar{c}_\omega \tau).$$

It follows that the physical time t as a function of dynamic rescaling τ given by (2.6) has a finite limit

$$T := \lim_{\tau \rightarrow +\infty} t(\tau) = \int_0^{+\infty} t_\tau(\tau) d\tau = \int_0^{+\infty} \tau_t^{-1}(\tau) d\tau = \int_0^{+\infty} C_\omega(\tau) d\tau < +\infty.$$

Then by L'Hospital's rule we can compute that

$$\lim_{t \rightarrow T^-} \frac{C_\omega(\tau)}{T-t} = - \lim_{t \rightarrow T^-} \frac{(C_\omega)_\tau}{t_\tau} = - \lim_{t \rightarrow T^-} c_\omega(\tau) = - \lim_{\tau \rightarrow +\infty} c_\omega(\tau) = -\bar{c}_\omega > 0,$$

i.e. $C_\omega(\tau) \sim -\bar{c}_\omega(T-t)$ as $t \rightarrow T^-$. Moreover, by the assumption on the convergence of c_l, c_ω , we have

$$\begin{aligned} \lim_{t \rightarrow T^-} C_l \cdot (T-t)^\gamma &= \lim_{t \rightarrow T^-} C_l \cdot \left(\frac{C_\omega}{-\bar{c}_\omega} \right)^\gamma \\ &= (-\bar{c}_\omega)^{-\gamma} \lim_{t \rightarrow T^-} C_l \cdot C_\omega^\gamma \\ &= (-\bar{c}_\omega)^{-\gamma} \exp \int_0^{+\infty} (c_l(\tau) + \gamma c_\omega(\tau)) d\tau \\ &= (-\bar{c}_\omega)^{-\gamma} \exp \int_0^{+\infty} ((c_l(\tau) - \bar{c}_l) + \gamma(c_\omega(\tau) - \bar{c}_\omega)) d\tau \\ &=: C_0 > 0. \end{aligned}$$

Here $\gamma = -\bar{c}_l/\bar{c}_\omega$. Recall, in view of the change of the variables in (2.3) and (2.4), we have

$$(T-t) \cdot \omega((T-t)^\gamma X, t) = \frac{T-t}{C_\omega} \cdot \Omega(C_l \cdot (T-t)^\gamma X, \tau(t)).$$

Therefore

$$\lim_{t \rightarrow T^-} (T-t) \cdot \omega((T-t)^\gamma X, t) = \lim_{t \rightarrow T^-} \frac{T-t}{C_\omega} \cdot \Omega(C_l \cdot (T-t)^\gamma X, \tau(t)) = -\frac{1}{\bar{c}_\omega} \bar{\Omega}(C_0 X),$$

since the convergence of Ω is locally uniform. \square

As a remark, the assumptions on the convergence of Ω and on the regularity of $\bar{\Omega}$ in Proposition 2.1 can be weakened (e.g. only in L^2 sense), and a similar conclusion (also in a weaker sense) can be derived with some extra technical effort. We state the proposition in the presented form only for demonstration purpose.

One can see from Proposition 2.1 that the magnitude blowup of ω is always at the scale of $(T-t)^{-1}$ regardless of the particular values of $\bar{c}_\omega, \bar{c}_l$ (as long as $\bar{c}_\omega < 0$). What matters is the ratio $\gamma = -\bar{c}_l/\bar{c}_\omega$ that determines the spatial shrinking rate of the solution, rather than the individual values of $\bar{c}_\omega, \bar{c}_l$. Moreover, the asymptotically self-similar blowup behavior of ω is governed by a rescaling of the limiting profile $\bar{\Omega}$, regardless of the specific form of the initial data. Nevertheless, the finite blowup time T relies on the initial condition.

Guided by Proposition 2.1, the problem of finding asymptotically self-similar blowups can be decomposed into two steps:

- (1) Finding a steady state of the dynamic rescaling equation (2.7).
- (2) Proving the stability of the steady state.

In general, it is not easy to theoretically construct exact self-similar profiles, let alone proving their stability. A more promising way to investigate the existence and stability of self-similar profiles is to solve the dynamic rescaling equation (2.7) numerically, and the key point is to appropriately impose normalization conditions to ensure the convergence of the profile Ω . Recall that the profile equation (2.8) admits two degrees of freedom due to its scaling property (2.9). Hence, we need to impose two normalization conditions to fix these two degrees of freedom, which in general also determine how the two variables $c_l(\tau), c_\omega(\tau)$ depend on the profile $\Omega(X, \tau)$ dynamically.

In previous studies on the blowup of the gCLM model, the initial condition ω_0 is usually chosen to be an odd function with negative derivative at the origin, i.e. $\omega'_0(x) \sim -c$ for some $c > 0$. In view of (2.2), u_0 is also an odd function. This odd-symmetry of ω is then preserved by the gCLM equation (1.1)

for all t up to the blowup time, and so is the sign of $\omega_x(0, \tau)$. Therefore, one common normalization condition is to fix the slope of Ω at the blowup point, i.e. $\Omega_x(0, \tau) = \Omega_x(0, 0)$ for all $\tau > 0$, which easily leads to

$$c_l(\tau) = c_\omega(\tau) + (1 - a)U_x(0, \tau). \quad (2.10)$$

This settles one degree of freedom. Nevertheless, we still need to determine another normalization to settle the second degree of freedom. While the first normalization condition (2.10) is commonly used in previous studies, the second normalization condition may differ from case to case, since the stability of the dynamic rescaling equation may heavily depend on the concrete choice of the normalization conditions.

2.2. A short survey of existing results. In this subsection, we review some existing results on self-similar finite-time blowups of the gCLM model (1.1). Some of these self-similar blowups were constructed using the dynamic rescaling method, for which we will also mention their dynamical normalization conditions. We again emphasize that in all results below, the self-similar profile $\bar{\Omega}$ is odd symmetric and has a non-zero derivative at $X = 0$ (non-degenerate in our terminology).

- For the case $a = 0$, the gCLM model (1.1) reduces to the original CLM model [CLM85], and a self-similar blowup solution was first found in [EJ20] with

$$\bar{\Omega}_0(X) = -\frac{4X}{1 + 4X^2}, \quad H(\bar{\Omega}_0)(X) = \frac{2}{1 + 4X^2}, \quad \gamma = 1.$$

Here the subscription “0” corresponds to $a = 0$, not the initial condition. The stability of this profile was proved in [EGM21] and [CHH21] along with the existence of asymptotic blowup for small $|a|$. Especially, the proof in [CHH21] is based on the dynamic rescaling method with one of the normalization conditions chosen as (2.10) and the other one as

$$c_\omega(\tau) = 1 - U_x(0, \tau).$$

- For the case $a = 1/2$, an exact self-similar blowup solution was first found in [Che20] and [LSS21] independently, with the self-similar profile and the scaling factor given by

$$\bar{\Omega}_{1/2}(X) = -\frac{\sqrt{3/8}X}{(3/8 + X^2)^2}, \quad H(\bar{\Omega}_{1/2})(X) = \frac{3/8 - X^2}{(3/8 + X^2)^2}, \quad \gamma = \frac{1}{3}.$$

In [Che20], the stability of this profile and the existence of asymptotically self-similar blowups for a close to $1/2$ were also proved via the dynamic rescaling method, and the normalization conditions are chosen to be (2.10) plus the second one as

$$c_\omega(\tau) = \frac{5}{3} - U_x(0, \tau).$$

- For the case $a = 1$, the gCLM model (1.1) reduces to the De Gregorio model [DG96], and (2.10) directly leads to $\gamma = -1$. The existence and stability of a compactly supported self-similar profile $\bar{\Omega}_1$ was obtained in [CHH21] using a combination of the dynamic rescaling method and a computer-assisted proof. In addition to (2.10), the second normalization condition was imposed as

$$c_l(\tau) = -\frac{U(L, \tau)}{L},$$

where $x = \pm L$ are the two boundary points of the compact support of $\bar{\Omega}_1$. More recently, [HTW23] constructed infinitely many compactly supported self-similar profiles (all with $\gamma = -1$) for the De Gregorio model as eigenfunctions of a linear compact operator, where the leading eigenfunction coincides with $\bar{\Omega}_1$ up to rescaling.

- Recently, a general existence result of interiorly smooth self-similar profiles for all $a \leq 1$ was established in [HQWW24] using a unified fixed-point argument. To be specific, for each a , an

exact self-similar profile $\bar{\Omega}_a$ is constructed as the fixed point of a certain nonlinear map. The profiles above for $a = 0, 1/2, 1$ are special cases in this family. They also provided theoretical estimation on a critical value a_c that divides focusing self-similar blowups and expanding ones, the existence of which was first numerically observed in [LSS21].

- Remarkably, a universal singular self-similar profile for all values of a was constructed in [CC09] in a closed form

$$\bar{\Omega}(X) = -\mathbf{1}_{\{-1 < X < 1\}} \frac{X}{\sqrt{1-X^2}}, \quad H(\bar{\Omega})(X) = \begin{cases} 1 - \frac{X}{\sqrt{X^2-1}}, & X > 1, \\ 1, & X \in (-1, 1), \\ 1 + \frac{X}{\sqrt{X^2-1}}, & X < -1, \end{cases}$$

with an a -dependent scaling factor $\gamma = \gamma_a = -a$. Note that this singular profile $\bar{\Omega}$ is distinct from those numerically observed and explicitly constructed in this paper. However, no evidence has been found that an asymptotically self-similar blowup of the form (1.3) with this singular profile $\bar{\Omega}$ can emerge from smooth initial data.

- Besides, a family of C^α self-similar blowup profiles was found in [EJ20] for $\alpha \in \{1/n : n \in \mathbb{N}\}$ and $|a| < \epsilon_0/\alpha$ with some small uniform constant ϵ_0 . For $a = 0$, each of these profiles can be explicitly written as

$$\bar{\Omega}^{(\alpha)}(X) = -\frac{\sin\left(\frac{\alpha\pi}{2}\right) \operatorname{sgn}(X)|X|^\alpha}{1 + 2 \cos\left(\frac{\alpha\pi}{2}\right) |X|^\alpha + |X|^{2\alpha}}, \quad H(\bar{\Omega}^{(\alpha)})(X) = \frac{1 + \cos\left(\frac{\alpha\pi}{2}\right) |X|^\alpha}{1 + 2 \cos\left(\frac{\alpha\pi}{2}\right) |X|^\alpha + |X|^{2\alpha}}$$

with a scaling factor $\gamma = \gamma_\alpha = 1/\alpha$. For general values of a , C^α self-similar profiles were constructed by power series expansion with respect to a . Later this result was improved in [Zhe23] by releasing the restriction $\alpha \in \{1/n : n \in \mathbb{N}\}$, but still requiring that $a\alpha \ll 1$.

- It is worth mentioning that modern techniques built on neural network architectures and training schemes have recently been developed to discover new self-similar blowups for the 3D Euler equations and related models [WLGSB23, WBM⁺25]. In particular, they numerically discovered a stable self-similar profile plus multiple unstable self-similar profiles for the Córdoba–Córdoba–Fontelos model that corresponds to the case $a = -1$. The stable one numerically coincides (up to rescaling) with that obtained in [HQWW24] by a fixed-point method, though the uniqueness of which has not been established.

2.3. Novel self-similar finite-time blowups with degenerate initial data. Note that all stable self-similar profiles constructed so far are odd functions of X and have a non-zero derivative at the origin. Correspondingly, the initial data must also have a non-zero derivative at the origin, since the sign of the derivative at the origin is preserved by the equation. Such initial data will be referred to as *non-degenerate* initial data in the sequel. It is then natural to ask whether self-similar finite-time blowups can develop from more degenerate initial data and how they differ from those arising from non-degenerate data. As stated in the introduction, the main purpose of this paper is to investigate this problem. To be specific, we investigate novel scenarios where the solution may develop a finite-time singularity at the origin while the initial condition ω_0 satisfies $\omega'_0(0) = 0$. In what follows, we call a solution ω or a profile Ω *degenerate* if its first derivative in space is zero at the origin. Specifically, we consider two kinds of degenerate initial data:

Assumption 2.2 (Odd-symmetric degenerate case). The initial solution ω_0 (or the initial profile Ω_0) satisfies

- Odd symmetry: $\omega_0(-x) = -\omega_0(x)$;
- Degeneracy: $\omega'_0(0) = 0$;
- Sign property: $\omega_0(x) \leq 0$ for all $x > 0$.

Assumption 2.3 (Half-line degenerate case). The initial solution ω_0 (or the initial profile Ω_0) satisfies

- Supported inside the positive half-line \mathbb{R}_+ : $\omega_0(x) = 0$ for all $x \leq 0$;
- Degeneracy: $\omega'_0(0) = 0$;
- Sign property: $\omega_0(x) \leq 0$ for all $x > 0$.

In addition to the above assumptions, we also assume that the initial data ω_0 satisfies suitable regularity and decay conditions (for instance, $\omega_0 \in H^1(\mathbb{R})$), so that the corresponding Hilbert transform (2.1) and its antiderivative (2.2) can be well defined.

Finite-time singularity formation from degenerate initial data has been studied for the special case $a = 0$ in a recent work [HQW25], where they proved that degenerate initial data can lead to self-similar finite-time blowups with a two-scale feature. In this paper we perform a systematic numerical study on finite-time blowups with degenerate initial data for a larger range of a . Our numerical simulation reveals novel self-similar blowup scenarios that are not only essentially different from those in the non-degenerate case but also have qualitatively distinct behaviors for $a > 0$ and for $a \leq 0$.

2.3.1. Regular self-similar profiles for $a > 0$. In the case $a > 0$, our numerical simulation indicates that odd-symmetric degenerate initial data (Assumption 2.2) can lead to ordinary self-similar finite-time blowups but with new regular profiles. These blowups exhibit similar behavior observed in the previous non-degenerate setting as in [EJ20, Che20, LSS21, CHH21, HQWW24], in the sense that the limiting self-similar profiles are regular and smooth in the interior of their support. Nevertheless, novelty lies in that these new profiles satisfy the same derivative degeneracy property as the initial data, a feature that has not been discovered and studied in the previous non-degenerate setting.

The behavior of the scaling factor γ in this scenario also differs from that in the non-degenerate case. Firstly, for each single $a > 0$, the value of γ not only depends on whether the corresponding profile is non-degenerate or degenerate but also on the vanishing order of the (limit) profile at the origin. Here the vanishing order (which is preserved by the profile equation (2.7)) of a profile $\Omega(X)$ is defined as the smallest integer k such that $\partial_X^k \Omega(0) \neq 0$. Secondly, the critical value a_c as the transition point of the sign of γ also depends on the vanishing order of the profile. As reported in [LSS21], in the non-degenerate case, a critical value $a_c \approx 0.689$ was numerically found to separate focusing self-similar blowups ($\gamma > 0$) from expanding ones ($\gamma < 0$). However, in the degenerate case with e.g. vanishing order $k = 3$, we have identified two critical values $a_{c,1} \approx 0.233$ and $a_{c,2} \approx 0.751$ such that $\gamma > 0$ for $a \in (0, a_{c,1}) \cup (a_{c,2}, +\infty)$ while $\gamma < 0$ for $a \in (a_{c,1}, a_{c,2})$. Moreover, the limiting self-similar profile starts to be compactly supported when a increasingly passes through $a_{c,1}$ and then transitions from a stable one to an unstable one when a increases through $a_{c,2}$. Detailed numerical results supporting these observations are presented in Section 4.

2.3.2. Singular self-similar profiles for $a \leq 0$. Things become more interesting when $a \leq 0$. In contrast to the non-degenerate setting, our numerical simulations suggest that for $a \leq 0$, degenerate initial data satisfying Assumption 2.2 or Assumption 2.3 lead to self-similar blowups with singular profiles. As we can see in Figure 1.1, profile evolution observed in the degenerate setting is qualitatively much distinct from that in the non-degenerate setting. Specifically, the magnitude of the profile $\Omega(X, \tau)$ becomes unbounded at a certain point in $[0, +\infty)$ as $\tau \rightarrow +\infty$, while elsewhere the profile converges to some limiting function. In other words, $\Omega(X, \tau)$ converges to a singular function as $\tau \rightarrow +\infty$. The location of the singularity point in the profile can be predetermined by imposing a normalization condition that will be explained later.

More precisely, we observe the following phenomenon for $a < 0$: as the solution evolves, the profile develops a sharp front near $X = \pm 1$ in the odd-symmetry case under Assumption 2.2 (or near $X = 1$ in the half-line case under Assumption 2.3) under our normalization conditions. The part of the profile in $(-1, 1)$ in the odd-symmetry case (or in $(0, 1)$ in the half-line case) flattens in time and asymptotically

vanishes, while the part beyond eventually converges to a spatially decaying tail extending to the far field with an algebraic decay rate. Notably, the profile behaviors in the odd-symmetry case and in the half-line case are quite qualitatively similar, only differing primarily in their limiting tail decay rates as $X \rightarrow +\infty$. Corresponding numerical results and analysis for $a < 0$ are presented in Section 5.

In addition to numerical evidence, we can in fact rigorously prove in the special case $a = 0$ that the profile solution $\Omega(X, \tau)$ to the dynamic rescaling equation (2.7) converges to a singular function as $\tau \rightarrow +\infty$. The following theorem describes such convergence in the odd-symmetry case.

Theorem 2.4. *Let $\Omega(X, \tau)$ be a solution to the dynamic rescaling equation (2.7) for $a = 0$ with smooth initial data Ω_0 satisfying Assumption 2.2 (the odd-symmetry case). Moreover, assume $\Omega_0(X) < 0$ for $X > 0$ and*

$$\limsup_{X \rightarrow 0^+} \left| \frac{X\Omega_0'(X)}{\Omega_0(X)} \right| < +\infty.$$

Without loss of generality, consider the normalization conditions

$$H(\Omega)(0, \tau) \equiv H(\Omega_0)(0) = 2, \quad H(\Omega)_{XX}(0, \tau) \equiv H(\Omega_0)_{XX}(0) = 4,$$

which yield constant scaling factors

$$c_l(\tau) \equiv \bar{c}_l = \frac{1}{2}, \quad c_\omega(\tau) \equiv \bar{c}_\omega = -1.$$

Then, as $\tau \rightarrow +\infty$, the solution $\Omega(X, \tau)$ converges to a singular limiting profile $\bar{\Omega}$ given by

$$\bar{\Omega}(X) = -\pi(\delta(X-1) - \delta(X+1)), \quad H(\bar{\Omega})(X) = \frac{2}{1-X^2},$$

in the sense that

$$\lim_{\tau \rightarrow +\infty} \Omega(X, \tau) = \bar{\Omega}(X), \quad \lim_{\tau \rightarrow +\infty} H(\Omega)(X, \tau) = H(\bar{\Omega})(X), \quad \text{for } X \neq \pm 1,$$

and for any test function $\varphi \in C_c^\infty(\mathbb{R})$,

$$\lim_{\tau \rightarrow +\infty} \int_{-\infty}^{+\infty} \Omega(X, \tau) \varphi(X) dX = -\pi(\varphi(1) - \varphi(-1)).$$

The proof of Theorem 2.4 is delayed to Section 3. As a remark, the degeneracy condition in Theorem 2.4, i.e. $\limsup_{X \rightarrow 0^+} |X\Omega_0'(X)/\Omega_0(X)| < +\infty$, is satisfied by any initial data with a finite vanishing order at the origin. Also note that, due to the sign property and the degeneracy property of the initial data Ω_0 , the normalization conditions in Theorem 2.4 are possible since

$$H(\Omega_0)(0) = -\frac{1}{\pi} \int_{\mathbb{R}} \frac{\Omega_0(X)}{X} dX, \quad H(\Omega_0)_{XX}(0) = -\frac{2}{\pi} \int_{\mathbb{R}} \frac{\Omega_0(X)}{X^3} dX.$$

A similar result can be proved if the odd symmetry is replaced by the half-line condition, which is in fact a consequence of the above theorem.

Corollary 2.5. *Let $\Omega(X, \tau)$ be a solution to the dynamic rescaling equation (2.7) for $a = 0$ with initial data Ω_0 satisfying Assumption 2.3 (the half-line case). Moreover, assume $\Omega_0(X) < 0$ for $X > 0$ and*

$$\limsup_{X \rightarrow 0^+} \left| \frac{X\Omega_0'(X)}{\Omega_0(X)} \right| < +\infty.$$

Without loss of generality, consider the normalization conditions

$$H(\Omega)(0, \tau) \equiv H(\Omega_0)(0) = 2, \quad H(\Omega)_X(0, \tau) \equiv H(\Omega_0)_X(0) = 2,$$

which yield constant scaling factors

$$c_l(\tau) \equiv \bar{c}_l = 1, \quad c_\omega(\tau) \equiv \bar{c}_\omega = -1.$$

Then, as $\tau \rightarrow +\infty$, the solution $\Omega(X, \tau)$ converges to a singular limiting profile $\bar{\Omega}$ given by

$$\bar{\Omega}(X) = -2\pi\delta(X - 1), \quad H(\bar{\Omega})(X) = \frac{2}{1 - X},$$

in the sense that

$$\lim_{\tau \rightarrow +\infty} \Omega(X, \tau) = \bar{\Omega}(X), \quad \lim_{\tau \rightarrow +\infty} H(\Omega)(X, \tau) = H(\bar{\Omega})(X), \quad \text{for } X \neq 1,$$

and for any test function $\varphi \in C_c^\infty(\mathbb{R})$,

$$\lim_{\tau \rightarrow +\infty} \int_{-\infty}^{+\infty} \Omega(X, \tau) \varphi(X) \, dX = -2\pi\varphi(1).$$

The proof of Corollary 2.5 is also delayed to Section 3.

As for $a < 0$, we have unfortunately not been able to prove the convergence of the profile $\Omega(X, \tau)$. However, we have found a family of explicit singular self-similar profiles in the half-line case (Assumption 2.3) for $a < 0$.

Theorem 2.6. *For any $a < 0$, the self-similar profile equation (2.8) admits an exact solution $(\bar{\Omega}_a, \bar{c}_{l,a}, \bar{c}_{\omega,a})$ given by*

$$\bar{\Omega}_a(X) = -\sin(\pi\mu) \frac{\mathbf{1}_{\{X>1\}}}{|1 - X|^\mu}, \quad \bar{c}_{l,a} = 1 - a, \quad \bar{c}_{\omega,a} = -1,$$

where $\mu = 1/(1 - a)$.

The proof follows from direct verification and is provided in Appendix B. In Section 5, we will provide strong evidence that, for each $a < 0$, solutions to (2.7) in the half-line degenerate case (Assumption 2.3) converge to the exact steady state given in Theorem 2.6 under appropriate normalization conditions. Besides, it is also an interesting problem whether one can construct exact singular self-similar profiles in the odd-symmetry case for all $a < 0$, which we leave for future studies.

2.4. Two-scale feature of self-similar blowups with singular profiles. The extra singularity formation in the profile $\Omega(X, \tau)$ in self-similar coordinates indicates that the solution may exhibit a two-scale behavior. In order to understand this two-scale feature, we introduce a secondary, smaller scale to resolve the inner profile. Recall that the outer scale, namely the ordinary self-similar scaling, is captured by $(T - t)^\gamma$. We also assume the trajectory of the maximum point of $|\omega|$ is given by $x(t) = r(t)(T - t)^\gamma$ for some function $r(t)$ such that the limit $\lim_{t \rightarrow T^-} r(t)$ exists. If we zoom into the neighborhood of $x(t)$ on a smaller spatial scale $(T - t)^{\hat{\gamma}}$ for some $\hat{\gamma} > \gamma$, we may observe a finer behavior of the solution in the form

$$\omega(x, t) = (T - t)^{\hat{\lambda}} \left(\hat{\Omega} \left(\frac{x - r(t)(T - t)^\gamma}{(T - t)^{\hat{\gamma}}} \right) + o(1) \right), \quad (2.11)$$

where $\hat{\Omega}$ denotes the inner profile, as opposed to the outer profile $\Omega(X, \tau)$. The validity of this two-scale ansatz relies on whether a secondary scale $(T - t)^{\hat{\gamma}}$ actually exists and captures the characteristic width of the shrinking peak of the outer profile. Fortunately, our numerical simulation has identified such a secondary scale for some $\hat{\gamma} > \gamma$ when the outer profile forms a singularity for $a < 0$. Moreover, we find that the inner profile $\hat{\Omega}$ remains smooth for all time and converges as $t \rightarrow T^-$ (or as $\tau \rightarrow +\infty$).

As mentioned in the introduction, two-scale self-similar finite-time blowups of the form (2.11) with degenerate initial data have been rigorously established in [HQW25] for the special case $a = 0$, where the inner profile $\hat{\Omega}$ is proved to be a traveling wave solution to the physical equation (1.1) with $a = 0$. Below we argue that for a general $a < 0$, if the two-scale ansatz (2.11) is in fact valid, then the inner profile $\hat{\Omega}$ must also be a traveling wave solution to the original physical equation (1.1).

Let us first assume that $r(t)$ is a constant r , as we can always achieve this by properly stretching the outer profile Ω in space. Substituting this two-scale ansatz (2.11) into the gCLM equation (1.1) yields

$$-\hat{\lambda}(T-t)^{\hat{\lambda}-1}\widehat{\Omega} + (T-t)^{\hat{\lambda}-1}\widehat{\Omega}_X \left(\hat{\gamma}X + r\gamma(T-t)^{\gamma-\hat{\gamma}} \right) + a(T-t)^{2\hat{\lambda}}\widehat{U}\widehat{\Omega}_X = (T-t)^{2\hat{\lambda}}\widehat{U}_X\widehat{\Omega},$$

which leads to

$$(T-t)^{-1} \left(-\hat{\lambda}\widehat{\Omega} + \hat{\gamma}X\widehat{\Omega}_X \right) + (T-t)^{\gamma-\hat{\gamma}-1}r\gamma\widehat{\Omega}_X = (T-t)^{\hat{\lambda}} \left(\widehat{U}_X\widehat{\Omega} - a\widehat{U}\widehat{\Omega}_X \right),$$

where

$$X = \frac{x - r(T-t)^\gamma}{(T-t)^\gamma}, \quad \widehat{U}_X = H(\widehat{\Omega}).$$

Note that as $t \rightarrow T^-$, the term $(T-t)^{\gamma-\hat{\gamma}-1}r\gamma\widehat{\Omega}_X$ dominates the left-hand side of the equation under the two-scale assumption $\hat{\gamma} > \gamma$. Therefore, to balance the equation of $\widehat{\Omega}$, we must have

$$\hat{\lambda} = \gamma - \hat{\gamma} - 1,$$

which also implies that the maximum of $|\omega|$ blows up faster than the overall blowup rate $(T-t)^{-1}$ on the outer scaling. Then taking the limit $t \rightarrow T^-$ yields the steady equation of $\widehat{\Omega}$ as

$$(r\gamma + a\widehat{U})\widehat{\Omega}_X = \widehat{U}_X\widehat{\Omega}, \quad (2.12)$$

which in fact describes the profile of a traveling wave solution to the original gCLM model (1.1).

To support the two-scale ansatz (2.11) and our asymptotic analysis above, we perform the following two additional studies. Firstly, we rigorously prove in Section 7 the existence of a traveling wave solution to (1.1) (whose profile is a solution to (2.12)) via a fixed-point method for all $a < 1$. This fixed-point method also leads to a numerical fixed-point iteration that generates a traveling wave profile up to high accuracy (see Appendix C.3). Secondly, for $a < 0$, we perform in Section 6 a comparison between the inner profile $\widehat{\Omega}$ obtained by numerically solving the dynamic rescaling equation (2.7) and the traveling wave profile obtained by the fixed-point iteration, showing that they match well with each other.

2.5. Traveling wave solutions. As argued above, the inner profile $\widehat{\Omega}$ in a two-scale self-similar blowup (2.11), if exists, must be a traveling wave solution to the gCLM model (1.1). This in turn leads to the question of whether such traveling wave solutions exist. To be specific, we look for traveling wave solutions to (1.1) of the form

$$\omega(x, t) = \bar{\omega}(x - rt), \quad (2.13)$$

where $\bar{\omega}$ is the traveling wave profile (and also the initial solution), the absolute value $|r|$ represents the traveling speed, and the sign of r indicates the traveling direction. Substituting (2.13) into the gCLM model (1.1) yields

$$(au - r)\bar{\omega}_x = \bar{u}_x\bar{\omega},$$

where $\bar{u}_x = H(\bar{\omega})$. One may immediately notice that this equation is identical to (2.12) up to change of notations and possible sign flipping. Using a similar fixed-point method as in [HQWW24], we can actually prove that traveling wave solutions exist for any $a \in (-\infty, 1)$, with the profile $\bar{\omega}$ being non-zero on \mathbb{R} for $a \leq 0$ but compactly supported for $a \in (0, 1)$.

Theorem 2.7. *For any $a \in (-\infty, 1)$, the generalized Constantin–Lax–Majda model admits a traveling wave solution of the form (2.13) (up to rescaling), where $\bar{\omega}$ is a non-negative even function such that $\bar{\omega}(x)$ is smooth in its support and non-increasing on $[0, +\infty)$, $\bar{\omega}(\sqrt{s})$ is convex in s for $s > 0$, $\bar{\omega}(0) > 0$, $\bar{\omega}''(0) < 0$, and*

$$r = r_a = -\frac{2\bar{\omega}(0)}{\pi\bar{\omega}_{xx}(0)} \int_0^{+\infty} \frac{\bar{\omega}(0) - \bar{\omega}(x)}{x^2} dx > 0.$$

Moreover, the following holds depending on the sign of a :

- $a \in (0, 1)$: $\bar{\omega}$ is compactly supported on $[-L_a, L_a]$ for some $L_a > 0$.
- $a = 0$: $\bar{\omega}(x) = 1/(1 + x^2)$.
- $a < 0$: $\bar{\omega}(x) > 0$ on \mathbb{R} , and there exist some $\bar{C}_a, \tilde{C}_a > 0$ such that, for all $|x| \geq 1$,

$$\bar{C}_a x^{-1/(1+|a|)} \leq \bar{\omega}(x) \leq \tilde{C}_a x^{-1/(1+|a|)}.$$

A detailed proof of Theorem 2.7, which consists of a series of intermediate lemmas, will be elaborated in Section 7.

3. CONVERGENCE TO SINGULAR PROFILES OF THE DYNAMIC RESCALING EQUATION FOR $a = 0$

When $a = 0$, the gCLM model (1.1) reduces to the original Constantin–Lax–Majda (CLM) model

$$\omega_t = u_x \omega, \quad u_x = \mathbf{H}(\omega), \quad (3.1)$$

Correspondingly, the dynamic rescaling equation (2.7) simplifies to

$$\Omega_\tau + c_l X \Omega_X = c_\omega \Omega + U_X \Omega. \quad (3.2)$$

It has been rigorously proved in [HQW25] that odd degenerate initial data can lead to multi-scale self-similar finite-time blowups for the CLM model (3.1). However, the convergence of the outer profile has not been established yet. In this section, we supplement their result by providing proofs for Theorem 2.4 and Corollary 2.5, establishing that the outer profile converges to a singular function under appropriate conditions.

Proof of Theorem 2.4. For notational simplicity, we will use x, t for X, τ and write $F = \Omega, G = \mathbf{H}(\Omega)$ in this proof. We also denote $F_0 = F(\cdot, 0), G_0 = G(\cdot, 0)$. By the odd symmetry and degeneracy of the initial data Ω_0 , we have

$$F_0(0) = 0, \quad F'_0(0) = 0, \quad F''_0(0) = 0, \quad \lim_{x \rightarrow 0} \frac{|F_0(x)|}{|x|^3} < +\infty.$$

Note that the odd symmetry and degeneracy of the initial datum are preserved by the dynamic rescaling equation (3.2), i.e.

$$F(x, t) = F(-x, t), \quad F_x(0, t) = F_{xx}(0, t) = 0, \quad \text{for all } t \geq 0.$$

By applying the Hilbert transform to the whole equation (3.2), we obtain a system of (F, G) as

$$\begin{aligned} F_t + c_l x F_x &= c_\omega F + FG, \\ G_t + c_l x G_x &= c_\omega G + \frac{1}{2}(G^2 - F^2). \end{aligned}$$

We have used the fact that $\mathbf{H}(F\mathbf{H}F) = (\mathbf{H}(F)^2 - F^2)/2$. Moreover, it is straightforward to check that the prescribed normalization conditions

$$G(0, t) \equiv G(0, 0) = 2, \quad G_{xx}(0, t) \equiv G_{xx}(0, 0) = 4,$$

determine the scaling factors c_l, c_ω as

$$c_l(t) \equiv \frac{1}{2}, \quad c_\omega(t) \equiv -1.$$

We thus obtain the dynamic system

$$\begin{aligned} F_t + \frac{1}{2}xF_x &= -F + FG, \\ G_t + \frac{1}{2}xG_x &= -G + \frac{1}{2}(G^2 - F^2), \\ G(0, t) &= 2, \quad G_{xx}(0, t) = 4. \end{aligned}$$

Note that the relation $G = \mathbf{H}(F)$ is preserved by this system. If we define $h = F + iG$, then this complex-valued function solves

$$h_t + \frac{1}{2}xh_x = -h - \frac{i}{2}h^2, \quad h(0, t) = 2i, \quad h_{xx}(0, t) = 4i.$$

Now consider the characteristic trajectories

$$X(x, t) = xe^{t/2}, \quad x \in \mathbb{R}.$$

Denote $h_0 = h(\cdot, 0)$. Then, along a characteristic $X(x, t)$, $h(X(x, t), t)$ solves

$$\frac{Dh}{Dt} = -h - \frac{i}{2}h^2,$$

which yields

$$h(X(x, t), t) = \frac{h(x, 0)}{e^t + \frac{i}{2}(e^t - 1)h(x, 0)} = \frac{h_0(x)}{e^t + \frac{i}{2}(e^t - 1)h_0(x)}.$$

By reversing the characteristics, we obtain

$$h(x, t) = \frac{h_0(xe^{-t/2})}{e^t + \frac{i}{2}(e^t - 1)h_0(xe^{-t/2})},$$

that is,

$$\begin{aligned} F(x, t) &= \frac{4e^t F_0(xe^{-t/2})}{(e^t - 1)^2 F_0(xe^{-t/2})^2 + (2e^t - (e^t - 1)G_0(xe^{-t/2}))^2}, \\ G(x, t) &= \frac{4e^t G_0(xe^{-t/2}) - 2(e^t - 1)(F_0(xe^{-t/2})^2 + G_0(xe^{-t/2})^2)}{(e^t - 1)^2 F_0(xe^{-t/2})^2 + (2e^t - (e^t - 1)G_0(xe^{-t/2}))^2}. \end{aligned}$$

Note that we have assumed $F_0(x) < 0$ for all $x > 0$, and thus $F(x, t)^2 + G(x, t)^2 < +\infty$ for any finite $t \geq 0$. Besides, recall that we have

$$\lim_{x \rightarrow 0} \frac{|F_0(x)|}{|x|^3} < +\infty, \quad G_0(0) = 2, \quad \lim_{x \rightarrow 0} \frac{G_0(x) - G_0(0)}{x^2} = \frac{1}{2}(G_0)_{xx}(0) = 2.$$

Under these assumptions, we may further assume that

$$|G_0(x) - (2 + 2x^2)| \leq Ax^4, \quad |x| \leq 1,$$

for some finite constant $A > 0$. Then, it can be easily verified that, for any compact set $S \subset \mathbb{R} \setminus \{\pm 1\}$, and for any sufficiently large t satisfying

$$x^2 e^{-t} \leq \min \left\{ 1, \frac{|x^2 - 1|}{2(1 + Ax^2)} \right\}, \quad \forall x \in S,$$

there exists some constant $C > 0$ (only depending on F_0, G_0) such that

$$|F(x, t)| \leq Ce^{-t/2} \cdot \frac{|x|^3}{|1 - x^2|^2}, \quad \left| G(x, t) - \frac{2}{1 - x^2} \right| \leq Ce^{-t} \cdot \frac{(1 + x^2)^2 x^2}{|1 - x^2|^3}, \quad x \in S. \quad (3.3)$$

In particular, for each $x \neq \pm 1$, we have

$$\lim_{t \rightarrow +\infty} F(x, t) = 0 = \bar{\Omega}(x), \quad \lim_{t \rightarrow +\infty} G(x, t) = \frac{2}{1-x^2} = H(\bar{\Omega})(x).$$

In fact, one can see from the calculation above that the convergence of $F(x, t)$ roots in the fact that $e^t F_0(xe^{-t/2})$ converges to 0 as $t \rightarrow +\infty$, which is true only when the vanishing order of $F_0(x)$ at $x = 0$ is strictly higher than 2. This reveals the essential difference between non-degenerate data and degenerate data in their blowup behaviors.

Next, we show that $F(x, t)$ converges to $\bar{\Omega}(x) = -\pi(\delta(x-1) - \delta(x+1))$ in the weak sense. By odd symmetry we only need to consider $x \geq 0$. For any compactly supported test function $\varphi \in C_c^\infty(\mathbb{R}_+)$, we consider the integral decomposition

$$\int_0^{+\infty} F(x, t) \varphi(x) dx = \int_{|x-1| \leq \epsilon} F(x, t) \varphi(x) dx + \int_{|x-1| > \epsilon, x \geq 0} F(x, t) \varphi(x) dx =: I_\epsilon(t) + J_\epsilon(t),$$

for some sufficiently small but fixed $\epsilon \in (0, 1)$. We can use (3.3) to obtain

$$|J_\epsilon(t)| \leq C \frac{e^{-t/2}}{\epsilon^2}.$$

The constant C may vary from line to line but is always independent of t and ϵ . Let us write

$$G_0(x) = 2 + 2x^2 q(x),$$

where q is a smooth even function such that $q(0) = 1$, $|q(x) - 1| \leq Cx^2$ and $|q'(x)| \leq C|x|$ for $|x| \leq 2$. We then rewrite $I_\epsilon(t)$ as

$$\begin{aligned} I_\epsilon(t) &= \int_{1-\epsilon}^{1+\epsilon} \frac{4e^t F_0(xe^{-t/2}) \varphi(x)}{(e^t - 1)^2 F_0(xe^{-t/2})^2 + (2e^t - (e^t - 1)G_0(xe^{-t/2}))^2} dx \\ &= \int_{1-\epsilon}^{1+\epsilon} \frac{4e^t F_0(xe^{-t/2}) \varphi(x)}{(e^t - 1)^2 F_0(xe^{-t/2})^2 + 4(1 - x^2(1 - e^{-t})q(xe^{-t/2}))^2} dx \\ &= \frac{1}{(1 - e^{-t})^2} \cdot \int_{1-\epsilon}^{1+\epsilon} \frac{-4\varphi(x)}{1 + 16 \left(\frac{1 - x^2(1 - e^{-t})q(xe^{-t/2})}{2(1 - e^{-t})\eta(x, t)} \right)^2} \cdot \frac{1}{\eta(x, t)} dx, \end{aligned}$$

where

$$\eta(x, t) := -e^t F_0(xe^{-t/2}).$$

Note that $\eta(x, t) > 0$ for all $x > 0$ and $t \geq 0$. Moreover, by the degeneracy assumption that $\lim_{x \rightarrow 0} |F_0(x)|/|x|^3 < +\infty$, we have

$$\eta(x, t) < Ce^{-t/2}, \quad x \in [1 - \epsilon, 1 + \epsilon].$$

Next, define

$$Y(x, t) := \frac{x^2 q(xe^{-t/2}) - (1 - e^{-t})^{-1}}{2\eta(x, t)}, \quad x \in [1 - \epsilon, 1 + \epsilon].$$

Note that by the properties of q , we have

$$Y(1 + \epsilon, t) \geq (c_0 \epsilon - Ce^{-t}) e^{t/2}, \quad Y(1 - \epsilon, t) \leq -(c_0 \epsilon - Ce^{-t}) e^{t/2}, \quad (3.4)$$

for some constant $c_0 > 0$. In particular, when t is sufficiently large, $Y(1 + \epsilon, t) > 0$ and $Y(1 - \epsilon, t) < 0$. We can also compute that

$$Y_x(x, t) = \frac{xq(xe^{-t/2})}{\eta(x, t)} + \frac{x^2 e^{-t/2} q'(xe^{-t/2})}{2\eta(x, t)} - \frac{x^2 q(xe^{-t/2}) - (1 - e^{-t})^{-1}}{2\eta(x, t)} \cdot \frac{\eta_x(x, t)}{\eta(x, t)}$$

$$= \frac{1}{\eta(x, t)} \left(1 + (x-1)q(xe^{-t/2}) + (q(xe^{-t/2}) - 1) + \frac{x^2 e^{-t/2} q'(xe^{-t/2})}{2} \right. \\ \left. - \frac{x^2 q(xe^{-t/2}) - (1 - e^{-t})^{-1} \cdot x \eta_x(x, t)}{2x} \cdot \frac{x \eta_x(x, t)}{\eta(x, t)} \right).$$

Note that by the assumption

$$\limsup_{x \rightarrow 0} \left| \frac{x F'_0(x)}{F_0(x)} \right| < +\infty,$$

we have

$$\left| \frac{x \eta_x(x, t)}{\eta(x, t)} \right| = \left| \frac{x e^{-t/2} F'_0(xe^{-t/2})}{F_0(xe^{-t/2})} \right| \leq C, \quad x \in [1 - \epsilon, 1 + \epsilon].$$

It follows that, for all $x \in [1 - \epsilon, 1 + \epsilon]$ and for sufficiently large t ,

$$|\eta(x, t) Y_x(x, t) - 1| \leq C(\epsilon + e^{-t}). \quad (3.5)$$

In particular, there exists some $t_0 > 0$ and some $\epsilon_0 \in (0, 1)$ such that, for $t > t_0$ and for $x \in [1 - \epsilon, 1 + \epsilon] \subset [1 - \epsilon_0, 1 + \epsilon_0]$,

$$Y_x(x, t) > \frac{1}{2\eta(x, t)} > 0.$$

This means for any $t \geq t_0$, $Y(x, t)$ as a function of $x \in [1 - \epsilon, 1 + \epsilon]$ admits an inverse function $x = X(y, t)$ for $y \in [Y(1 - \epsilon, t), Y(1 + \epsilon, t)]$. Using $x = X(y, t)$ as a change of variable, we may continue the calculation of $I_\epsilon(t)$ as

$$I_\epsilon(t) = \frac{1}{(1 - e^{-t})^2} \cdot \int_{1-\epsilon}^{1+\epsilon} \frac{-4\varphi(x)}{1 + 16 \left(\frac{1-x^2(1-e^{-t})q(xe^{-t/2})}{2(1-e^{-t})\eta(x, t)} \right)^2} \cdot \frac{1}{\eta(x, t)} dx \\ = \frac{1}{(1 - e^{-t})^2} \cdot \int_{Y(1-\epsilon, t)}^{Y(1+\epsilon, t)} \frac{-4\varphi(X(y, t))}{1 + 16y^2} \cdot \frac{1}{\eta(x, t) Y_x(X(y, t), t)} dy.$$

Note that

$$\pi = \int_{\mathbb{R}} \frac{4}{1 + 16y^2} dy = \int_{Y(1-\epsilon, t)}^{Y(1+\epsilon, t)} \frac{4}{1 + 16y^2} dy + \int_{\mathbb{R} \setminus [Y(1-\epsilon, t), Y(1+\epsilon, t)]} \frac{4}{1 + 16y^2} dy.$$

Then, using (3.4), (3.5), and the smoothness of φ , we can derive that

$$|I_\epsilon(t) - (-\pi\varphi(1))| \leq \left| \int_{Y(1-\epsilon, t)}^{Y(1+\epsilon, t)} \left(\frac{(1 - e^{-t})^{-2}}{\eta(x, t) Y_x(X(y, t), t)} \varphi(X(y, t)) - \varphi(1) \right) \frac{4}{1 + 16y^2} dy \right| \\ + \left| \int_{\mathbb{R} \setminus [Y(1-\epsilon, t), Y(1+\epsilon, t)]} \frac{4\varphi(1)}{1 + 16y^2} dy \right| \\ \leq C \left(\epsilon + e^{-t} + \frac{e^{-t/2}}{c_0\epsilon - Ce^{-t}} \right).$$

Finally, we obtain

$$\left| \int_0^{+\infty} F(x, t) \varphi(x) dx - (-\pi\varphi(1)) \right| \leq |I_\epsilon(t) - (-\pi\varphi(1))| + |J_\epsilon(t)| \\ \leq C \left(\epsilon + e^{-t} + \frac{e^{-t/2}}{c_0\epsilon - Ce^{-t}} + \frac{e^{-t/2}}{\epsilon^2} \right).$$

In particular, for t sufficiently large such that $e^{-t} \ll \epsilon^6$, we have

$$\left| \int_0^{+\infty} F(x, t) \varphi(x) dx - (-\pi \varphi(1)) \right| \leq C\epsilon.$$

Since $\epsilon \in (0, 1)$ can be arbitrarily small, it follows that

$$\lim_{t \rightarrow +\infty} \int_0^{+\infty} F(x, t) \varphi(x) dx = -\pi \varphi(1).$$

This completes the proof. \square

Proof of Corollary 2.5. This corollary follows directly from Theorem 2.4 via a change of variable. Let $\Omega(X, \tau)$ be a solution to (2.7) for $a = 0$ that satisfies all assumptions and normalization conditions of Corollary 2.5. Specifically, Ω solves the dynamic rescaling equation

$$\Omega_\tau + c_l X \Omega_X = (c_\omega + H(\Omega)) \Omega$$

with $c_l = 1$ and $c_\omega = -1$. Define

$$\tilde{\Omega}(X, \tau) := \operatorname{sgn}(X) \cdot \Omega(X^2, \tau).$$

It is not hard to see that, if the initial condition $\Omega_0(x) = \Omega(x, 0)$ satisfies Assumption (2.3) (half-line case), then the new initial condition $\tilde{\Omega}_0(x) = \tilde{\Omega}(x, 0)$ satisfies Assumption (2.2) (odd-symmetry case). It also holds that

$$\limsup_{X \rightarrow 0} \left| \frac{X \tilde{\Omega}'_0(X)}{\tilde{\Omega}_0(X)} \right| = 2 \limsup_{X \rightarrow 0} \left| \frac{X^2 \Omega'_0(X^2)}{\Omega_0(X^2)} \right| = 2 \limsup_{X \rightarrow 0^+} \left| \frac{X \Omega'_0(X)}{\Omega_0(X)} \right| < +\infty.$$

Moreover, one can easily use the formula of the Hilbert transform to verify that

$$H(\tilde{\Omega})(X, \tau) = H(\Omega)(X^2, \tau).$$

As an immediate consequence, $\tilde{\Omega}(X, \tau)$ solves the corresponding dynamic rescaling equation

$$\tilde{\Omega}_\tau + \tilde{c}_l X \tilde{\Omega}_X = (\tilde{c}_\omega + H(\tilde{\Omega})) \tilde{\Omega}$$

with $\tilde{c}_l = c_l/2 = 1/2$ and $\tilde{c}_\omega = c_\omega = -1$, and it satisfies the normalization conditions

$$H(\tilde{\Omega})(0, \tau) \equiv H(\tilde{\Omega}_0)(0) = H(\Omega_0)(0) = 2,$$

$$H(\tilde{\Omega})_{XX}(0, \tau) \equiv H(\tilde{\Omega}_0)_{XX}(0) = 2H(\Omega_0)_X(0) = 4.$$

That is, the solution $\tilde{\Omega}$ satisfies all assumptions and normalization conditions of Theorem 2.4. Therefore, the convergence result of Corollary 2.5 readily follows from the convergence result of Theorem 2.4. \square

4. NUMERICAL RESULTS WITH DEGENERATE INITIAL DATA FOR THE $a > 0$

In this section, we present numerical results obtained from dynamic rescaling simulations of the gCLM model (1.1) with degenerate initial data in the case $a > 0$. Recall that the dynamic rescaling equation is given by

$$\Omega_\tau + (c_l X + aU) \Omega_X = (c_\omega + U_X) \Omega, \quad U_X = H(\Omega), \quad U(0) = 0. \quad (4.1)$$

As discussed in Section 2, (4.1) is equivalent to the original gCLM equation (1.1) via time-dependent scaling transformations. Furthermore, the convergence of the profile solution would imply that the original gCLM equation develops a finite-time singularity in a self-similar manner. Therefore, we simulate the dynamic rescaling equation (4.1) to investigate potential self-similar blowup of the gCLM model with degenerate initial data.

It is straightforward to verify that the dynamic rescaling equation (4.1) preserves the vanishing order of the solution at the origin. Numerically, however, directly evolving (4.1) with degenerate initial

data is delicate, since round-off and discretization errors tend to destroy the high-order degeneracy near $X = 0$. To deal with this issue, we factor out the prescribed vanishing order by introducing

$$f(X, \tau) = \frac{\Omega(X, \tau)}{X^k},$$

where k is the vanishing order of the initial data Ω_0 at the origin, and we instead evolve f via

$$f_\tau + (c_l X + aU) f_X = \left(c_\omega + U_X - k \left(c_l + a \frac{U}{X} \right) \right) f,$$

where $U_X = \mathbf{H}(X^k f)$. To uniquely determine the scaling factors c_l and c_ω , we must impose two normalization conditions. Since the model preserves the degeneracy of the initial data, a natural normalization condition is to fix the value of f at the origin at 1, i.e.

$$f(0, \tau) = \lim_{X \rightarrow 0} \frac{\Omega(X, \tau)}{X^k} \equiv -1.$$

For the second normalization condition, we fix the location of the minimum of Ω at $X = 1$ by imposing

$$\Omega_X(1, \tau) \equiv 0.$$

In this section, we focus on odd-symmetric smooth initial data (Assumption 2.2). In fact, under odd symmetry, the vanishing order k of Ω must be an odd natural number and is preserved for all time by the equation. Throughout this section, we take the initial condition of f as

$$f_0(X) = -\frac{3}{3 + kX^{k+3}},$$

so that $\Omega_0(X) = X^k f_0(X) = -3X^k / (3 + kX^{k+3})$. This choice satisfies the normalization conditions at $\tau = 0$, namely $f_0(0) = -1$ and $\Omega'_0(1) = 0$. We defer the implementation details of the dynamic rescaling simulations to Appendix C.

In the remainder of this section, we first demonstrate the convergence of the dynamic rescaling simulations using the case $a = 0.5$ and $k = 3$ as an illustrative example. We then present numerical results for various values of $a > 0$ with a fixed vanishing order $k = 3$, followed by results for different vanishing orders $k \geq 3$ with a fixed $a = 0.5$. Finally, we provide a comprehensive table summarizing the scaling factors c_l, c_ω and the spatial shrinking rate $\gamma = -c_l/c_\omega$ for different combinations of $a > 0$ and $k \geq 3$.

4.1. Convergence of profiles. Below we present illustrative numerical results demonstrating convergence of the dynamic rescaling method for the case $a = 0.5$ with vanishing order $k = 3$. Figure 4.1 shows the evolution of the rescaled profile $\Omega(X, \tau)$ and $f(X, \tau)$. The condition $f(0) = -1$ is preserved throughout the computation, confirming that the prescribed degeneracy at the origin is maintained numerically. We declare convergence when the residual of (4.1) falls below 1.5×10^{-8} , and denote the resulting steady state by $\bar{\Omega}$. As illustrated in Figure 4.1, the limiting profile $\bar{\Omega}$ is regular and smooth in the interior of its support and vanishes at the origin with the same order as the initial data. In particular, this profile differs from previously studied self-similar blowup profiles, which typically exhibit linear vanishing at $X = 0$.

The convergence of the scaling factors c_l, c_ω , and the spatial shrinking rate $\gamma = -c_l/c_\omega$ is shown in Figure 4.2. These quantities stabilize as $\Omega(X, \tau)$ approaches the steady state, supporting the formation of a one-scale self-similar blowup in this setting.

4.2. Numerical results for different $a > 0$ with a fixed vanishing order $k = 3$. Here we present the numerical results of the dynamic rescaling simulations for different $a > 0$ with a fixed vanishing order $k = 3$ for the initial data. The scaling factors of the steady state for $0.1 \leq a \leq 1.5$ are listed in Table 4.1, and the corresponding self-similar profiles are plotted in Figure 4.3. Note that due to the scaling

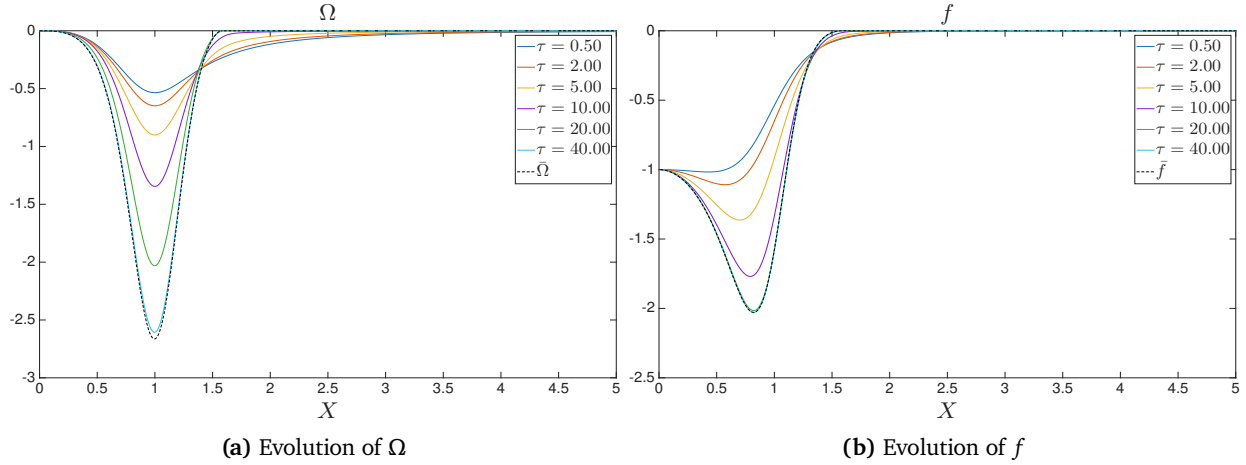


Figure 4.1: Convergence of the profile for $a = 0.5$ and $k = 3$. (a) Evolution of the rescaled profile $\Omega(X, \tau)$ at different times. The dashed line plots the final steady state $\bar{\Omega}$, of which the residual has dropped below 1.5×10^{-8} . (b) Evolution of $f(X, \tau)$, related to $\Omega(X, \tau)$ by $f(X, \tau) = \Omega(X, \tau)/X^k$. The preservation of $f(0) = 1$ throughout the evolution demonstrates that the degeneracy of the solution at the origin is maintained numerically.

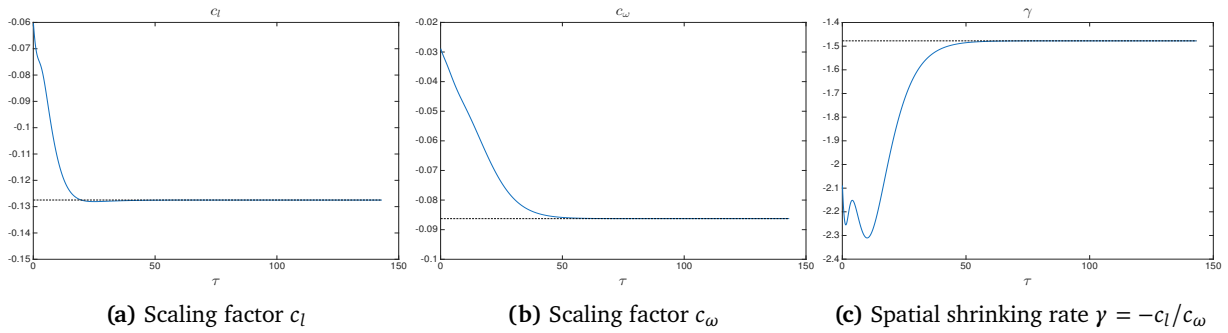


Figure 4.2: Convergence of the scaling factors for $a = 0.5$ and $k = 3$. The stabilization of c_l , c_ω , and γ as τ increases supports convergence towards a one-scale self-similar blowup.

invariance property (2.9), the precise values of \bar{c}_l and \bar{c}_ω depend on the normalization conditions and are thus not intrinsic. The physically relevant quantity is the ratio $\bar{\gamma} = -\bar{c}_l/\bar{c}_\omega$, which determines the spatial shrinking rate of the solution.

Lushnikov et al. [LSS21] performed direct numerical simulations of the gCLM model (1.1) and found evidence of self-similar finite-time blowup arising from smooth initial data for a wide range of the parameter a . They observed a critical value $a_c \approx 0.6891$ such that for $a < a_c$, the self-similar profile is supported on the whole real line and the blowup is focusing (i.e., $\gamma > 0$), while for $a > a_c$, the self-similar profile is compactly supported and the blowup is expanding (i.e., $\gamma < 0$).

Our numerical results for degenerate initial data suggest a similar phenomenon, but with different critical values. As shown in Table 4.1, there exists a critical value $a_{c,1} \in (0.232931, 0.232932)$ across which \bar{c}_l changes sign from positive to negative. This corresponds to a transition of the self-similar profile from being smooth and supported on the whole real line to being compactly supported. Such critical value $a_{c,1}$ differs from the a_c reported in [LSS21]; we conjecture this discrepancy arises from the different vanishing order of the initial data at the origin.

Moreover, we identify a second critical value $a_{c,2} \in (0.751405, 0.751406)$ at which c_ω changes sign from negative to positive. This indicates a transition from blowup to non-blowup in the original gCLM

a	0.1	0.2	0.232931	0.232932	0.3	0.4	0.5
\bar{c}_l	1.0888	0.0691	6.4688×10^{-7}	-9.7142×10^{-7}	-0.0717	-0.1135	-0.1288
\bar{c}_ω	-3.8668	-0.8357	-0.6055	-0.6055	-0.3479	-0.1718	-0.0872
\bar{y}	0.2816	0.0827	1.0683×10^{-6}	-1.6043×10^{-6}	-0.2061	-0.6604	-1.4771
a	0.6	0.7	0.751405	0.751406	0.8	0.9	1
\bar{c}_l	-0.1345	-0.1364	-0.1364	-0.1364	-0.1365	-0.1360	-0.1352
\bar{c}_ω	-0.0399	-0.0108	-5.8090×10^{-8}	1.3080×10^{-7}	0.0084	0.0217	0.0314
\bar{y}	-3.3734	-12.6465	-2.3481×10^6	1.0429×10^6	16.2599	6.2550	4.2996
a	1.1	1.2	1.3	1.4	1.5		
\bar{c}_l	-0.1345	-0.1338	-0.1334	-0.1332	-0.1331		
\bar{c}_ω	0.0388	0.0446	0.0492	0.0531	0.0565		
\bar{y}	3.4658	3.0034	2.7094	2.5058	2.3563		

Table 4.1: Scaling factors of the steady state for $0.1 \leq a \leq 1.5$ with fixed vanishing order $k = 3$. We observe two critical values: $a_{c,1} \in (0.232931, 0.232932)$, where c_l changes sign from positive to negative, and $a_{c,2} \in (0.751405, 0.751406)$, where c_ω changes sign from negative to positive.

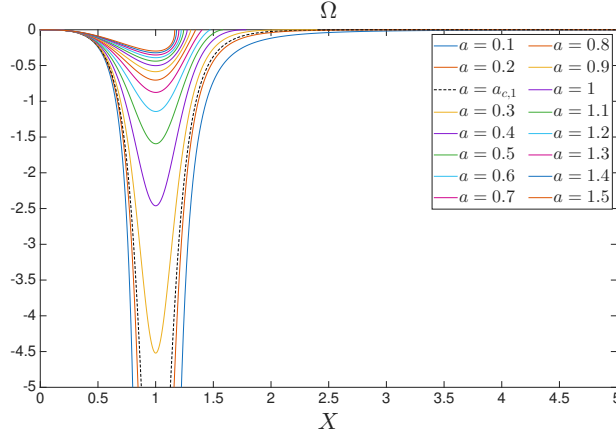


Figure 4.3: Steady states of the profile $\bar{\Omega}(X)$ for $0.1 \leq a \leq 1.5$ with fixed vanishing order $k = 3$. The dashed curve corresponds to the critical value $a = a_{c,1}$ at which the profile transitions from being smooth with full-line support to being compactly supported.

equation (1.1), since Proposition 2.1 requires $\bar{c}_\omega < 0$ for a one-scale asymptotically self-similar blowup. Nevertheless, even when $a > a_{c,2}$, one can still obtain an exact self-similar blowup solution of (1.1) from the steady state $\bar{\Omega}$ computed via the dynamic rescaling equation (4.1). Define

$$\Omega^{\text{flip}}(X, \tau) := -\Omega(X, -\tau), \quad c_l^{\text{flip}} = -c_l(-\tau), \quad c_\omega^{\text{flip}} = -c_\omega(-\tau),$$

and correspondingly

$$\bar{\Omega}^{\text{flip}}(X) := -\bar{\Omega}(X), \quad \bar{c}_l^{\text{flip}} = -\bar{c}_l, \quad \bar{c}_\omega^{\text{flip}} = -\bar{c}_\omega.$$

Then, by the scaling invariance (2.9), the triple $(\bar{\Omega}^{\text{flip}}, \bar{c}_l^{\text{flip}}, \bar{c}_\omega^{\text{flip}})$ also solves the steady profile equation (2.8). Hence $\bar{\Omega}^{\text{flip}}$ is an exact self-similar blowup profile for (1.1). On the other hand, Ω^{flip} satisfies the dynamic rescaling equation with scaling factors c_l^{flip} and c_ω^{flip} :

$$\Omega_\tau^{\text{flip}} + (c_l^{\text{flip}} X + aU^{\text{flip}})\Omega_X^{\text{flip}} = (c_\omega^{\text{flip}} + U_X^{\text{flip}})\Omega^{\text{flip}},$$

where $U^{\text{flip}}(X, \tau) = -U(X, -\tau)$. The linearization of this flipped evolution about $\bar{\Omega}^{\text{flip}}$ has the opposite sign compared to the linearization of (2.7) about $\bar{\Omega}$. Therefore, the observed convergence of the

dynamic rescaling equation toward $\bar{\Omega}$ (i.e. stability of $\bar{\Omega}$) implies that $\bar{\Omega}^{\text{flip}}$ is unstable. Consequently, as a increases across $a_{c,2}$, the blowup transitions from stable to unstable, while the self-similar profile remains compactly supported. Below we plot the profiles $\bar{\Omega}$ for $a < a_{c,2}$ and the flipped profiles $\bar{\Omega}^{\text{flip}}$ for $a > a_{c,2}$ in Figure 4.4 to better illustrate the transition across $a_{c,2}$.

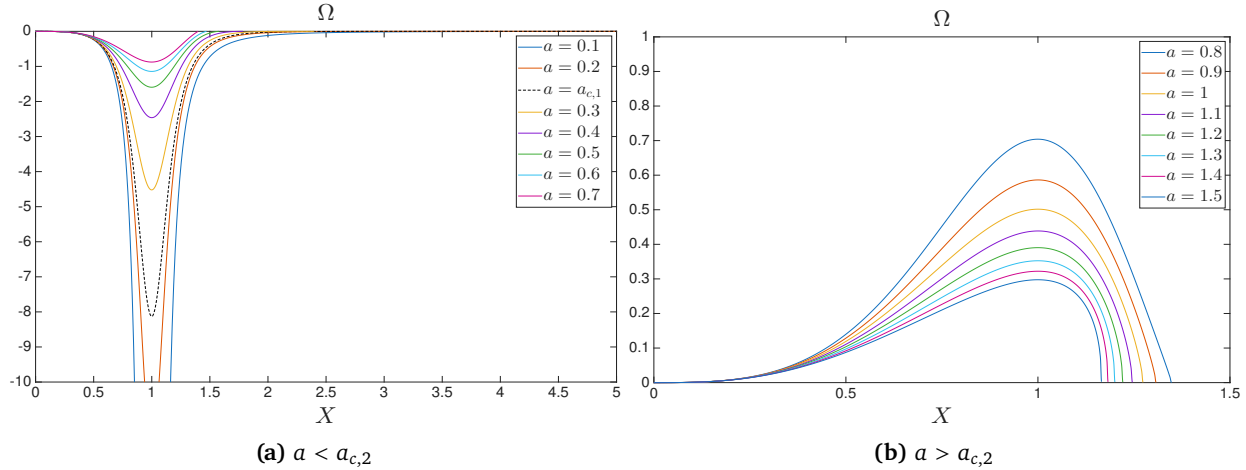


Figure 4.4: One-scale self-similar blowup profiles for fixed vanishing order $k = 3$: (a) $a < a_{c,2}$ and (b) $a > a_{c,2}$. In (b), we plot the flipped profiles $\bar{\Omega}^{\text{flip}}(X) := -\bar{\Omega}(X)$ since $\bar{c}_\omega > 0$ in these cases; these $\bar{\Omega}^{\text{flip}}$ correspond to unstable self-similar blowups.

4.3. Numerical results for different vanishing orders k with fixed $a = 0.5$. We next present dynamic rescaling results for initial data with different vanishing orders k at the origin, while keeping $a = 0.5$ fixed. The steady-state scaling factors for $k = 3, 5, 7, 9, 11$ are reported in Table 4.2, and the corresponding self-similar profiles are shown in Figure 4.5.

k	3	5	7	9	11
\bar{c}_l	-0.1288	-0.1052	-0.0497	-0.0168	-0.0044
\bar{c}_ω	-0.0872	-0.0193	-0.0016	6.7927×10^{-4}	3.7201×10^{-4}
$\bar{\gamma}$	-1.4771	-5.4586	-30.5045	24.7677	11.9515

Table 4.2: Scaling factors for profiles with vanishing orders $k = 3, 5, 7, 9, 11$ and fixed $a = 0.5$.

We observe that, for a fixed a , there can be multiple blowup profiles distinguished by their vanishing orders at the origin, and the associated scaling factors may differ substantially. As shown in Table 4.2, c_ω changes sign from negative to positive between $k = 7$ and $k = 9$. This transition suggests that, for $a = 0.5$, initial data with sufficiently high vanishing order (in particular, $k \geq 9$) may not exhibit the stable self-similar blowup behavior observed for smaller values of k .

4.4. Numerical results for various values of $a > 0$ and $k \geq 3$. Table 4.3 summarizes the measured shrinking rates $\bar{\gamma}$ for $0.1 \leq a \leq 1$ and vanishing orders $k \in \{3, 5, 7, 9, 11\}$. These data highlight a strong dependence of $\bar{\gamma}$ on both the advection parameter a and the vanishing order k . For each fixed k , as a varies from 0.1 to 1, $\bar{\gamma}$ may change sign multiple times, indicating transitions between focusing ($\bar{\gamma} > 0$) and expanding ($\bar{\gamma} < 0$) blowups. Likewise, for each fixed a , varying k can also induce sign changes in $\bar{\gamma}$, showing that the vanishing order at the origin can substantially affect the observed self-similar blowup behavior.

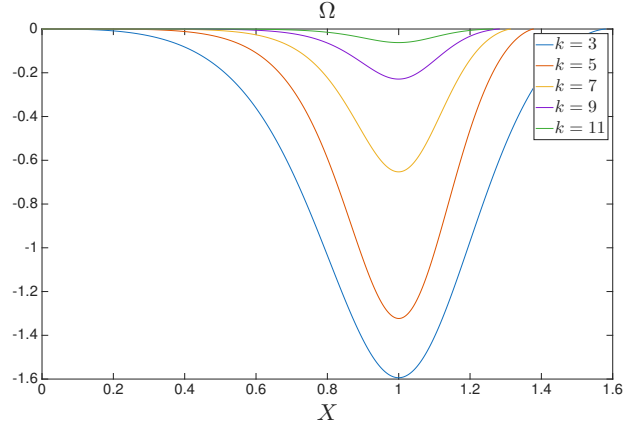


Figure 4.5: One-scale self-similar profiles $\Omega(X)$ for $k = 3, 5, 7, 9, 11$ with fixed $a = 0.5$.

$\bar{\gamma} \backslash a$ k	0.1	0.2	0.3	0.4	0.5
3	0.2816	0.0827	-0.2061	-0.6604	-1.4771
5	0.1201	-0.2000	-0.7406	-1.8523	-5.4586
7	0.0112	-0.4125	-1.2239	-3.4137	-30.5045
9	-0.0678	-0.5798	-1.6672	-5.5676	24.7677
11	-0.1292	-0.7152	-2.0756	-8.7223	11.9515

$\bar{\gamma} \backslash a$ k	0.6	0.7	0.8	0.9	1
3	-3.3734	-12.6465	16.2599	6.2550	4.2996
5	61.5417	6.9537	4.3061	3.3675	2.8870
7	8.3875	4.5758	3.4829	2.9737	2.6862
9	6.5143	4.5096	3.9087	3.7528	3.8290
11	11.4908	15.2982	222.7743	-13.4241	-6.2561

Table 4.3: Scaling factors $\bar{\gamma}$ for profiles with $0.1 \leq a \leq 1$ vanishing orders $k = 3, 5, 7, 9, 11$.

5. NUMERICAL RESULTS WITH DEGENERATE INITIAL DATA FOR $a < 0$

In this section, we present the numerical results of the dynamic rescaling simulations for the gCLM model (1.1) with degenerate initial data when $a < 0$.

Recall that ω_0 denotes the initial data of the gCLM model (1.1). In the following subsections, we consider the initial data in both the odd-symmetry case (Assumption 2.2) and the half-line case (Assumption 2.3) with the following subdivisions:

- Case 1.1: ω_0 is odd symmetric (i.e. $\omega_0(-x) = -\omega_0(x)$), $\omega_0'(0) = 0$, and $\omega_0(x) < 0$ for $x > 0$;
- Case 1.2: ω_0 is odd symmetric, $\omega_0(x) = 0$ on $[-1, 1]$, and $\omega_0(x) < 0$ for $x > 1$;
- Case 2.1: $\omega_0(x) = 0$ for $x \leq 0$, $\omega_0'(0) = 0$, and $\omega_0(x) < 0$ for $x > 0$;
- Case 2.2: $\omega_0(x) = 0$ for $x \leq 1$, and $\omega_0(x) < 0$ for $x > 1$.

In all four cases, the initial condition ω_0 is degenerate at the origin and C^∞ -smooth on the entire real line. Note that in the dynamic rescaling formulation, the initial condition ω_0 for the gCLM model (1.1) corresponds directly to the initial profile $\Omega_0 = \Omega(\cdot, 0)$ for the dynamic rescaling equation (2.7). The specific initial data chosen for these four cases are plotted in Figure 5.1. For Case 1.1, we select an initial datum with infinite vanishing order at the origin. This choice is motivated by our numerical

observation that, under our normalization conditions, all derivatives at the origin satisfy $\partial_X^j \Omega(0, \tau) \rightarrow 0$ as $\tau \rightarrow +\infty$. This suggests that the self-similar profile possesses infinite vanishing order at the origin, regardless of the specific vanishing order of the initial data. We will discuss such phenomenon further in Section 5.1.

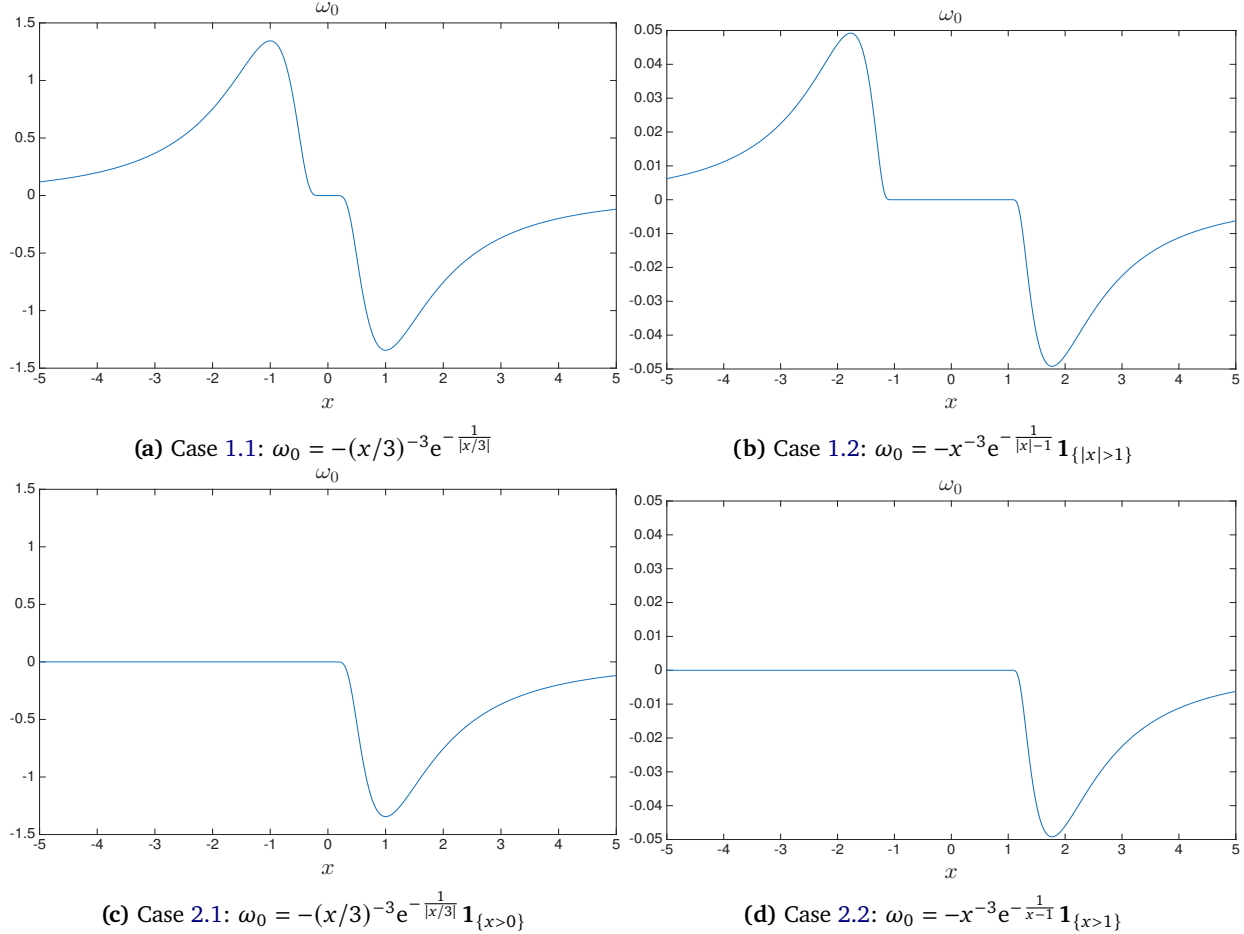


Figure 5.1: Initial data for $a < 0$. All the initial data are C^∞ -smooth, negative when $x > 0$, and has infinite vanishing order at the origin.

5.1. Numerical results for different $a < 0$ with odd symmetric degenerate initial data. Here we present numerical results from dynamic rescaling simulations for $a < 0$ with odd-symmetric degenerate initial data (under Assumption 2.2), corresponding to Cases 1.1 and 1.2. The normalization conditions used to close the dynamic rescaling equation (2.7) differ between these two cases. When $a < 0$, our simulations indicate that the rescaled profile Ω evolving from degenerate data develops *infinite* vanishing order at the origin (see further discussion below). Consequently, the normalization condition $\lim_{X \rightarrow 0} -\Omega(X, \tau)/X^k \equiv 1$ (which fixes a prescribed finite vanishing order) is not suitable in this case. We therefore adopt normalization conditions that do not depend on the local Taylor behavior at $X = 0$.

In particular, for Case 1.1, we choose to fix the value of the Hilbert transform at the origin, i.e. $H(\Omega)(0, \tau) \equiv H(\Omega_0)(0)$. Together with pinning the location of the minimum at $X = 1$, we impose

$$\partial_X \Omega(1, \tau) \equiv 0, \quad H(\Omega)(0, \tau) \equiv H(\Omega_0)(0). \quad (5.1)$$

For Case 1.2, since the initial data vanish on $[-1, 1]$, the condition $\partial_X \Omega(1, \tau) \equiv 0$ is not suitable for pinning the location of the minimum. Instead, we fix the boundary of the support of Ω at $X = 1$ by

imposing

$$c_l(\tau) + aU(1, \tau) \equiv 0,$$

which makes the convection speed in the dynamic rescaling equation (2.7) vanish at $X = 1$. As a result, the support boundary remains stationary at $X = 1$ throughout the evolution. Therefore, for Case 1.2, we impose

$$c_l(\tau) + aU(1, \tau) \equiv 0, \quad \mathbf{H}(\Omega)(0, \tau) \equiv \mathbf{H}(\Omega_0)(0). \quad (5.2)$$

Figures 5.2 and 5.3 display the evolution of the rescaled profile $\Omega(X, \tau)$ and the corresponding advection speed $c_l(\tau)X + aU(X, \tau)$ for $a = -1$ in Case 1.1 and Case 1.2, respectively. In Case 1.1, as τ increases, Ω develops an increasingly sharp front near $X = 1$ and appears to approach a singular limit there as $\tau \rightarrow +\infty$. At the same time, the profile on $[0, 1]$ flattens progressively and tends to vanish. This behavior is related to the evolution of the advection speed $c_lX + aU$. As we can see in Figure 5.2(b), $c_lX + aU$ remains positive for $X > 0$, decreases to 0 at $X = 1$ as τ grows, and develops a cusp-like shape near $X = 1$. The positivity of $c_lX + aU$ on $(0, 1)$ indicates that the degeneracy of Ω near $X = 0$ is transported toward $X = 1$, thus suppressing Ω on $[0, 1]$ and leading to the observed flattening. At the same time, the emergence of a stagnation point at $X = 1$ prevents the flattening from going beyond $X = 1$, allowing the profile Ω to form a singularity at $X = 1$. For $X > 1$, the velocity becomes positive again, transporting Ω away from the front and generating the observed tail.

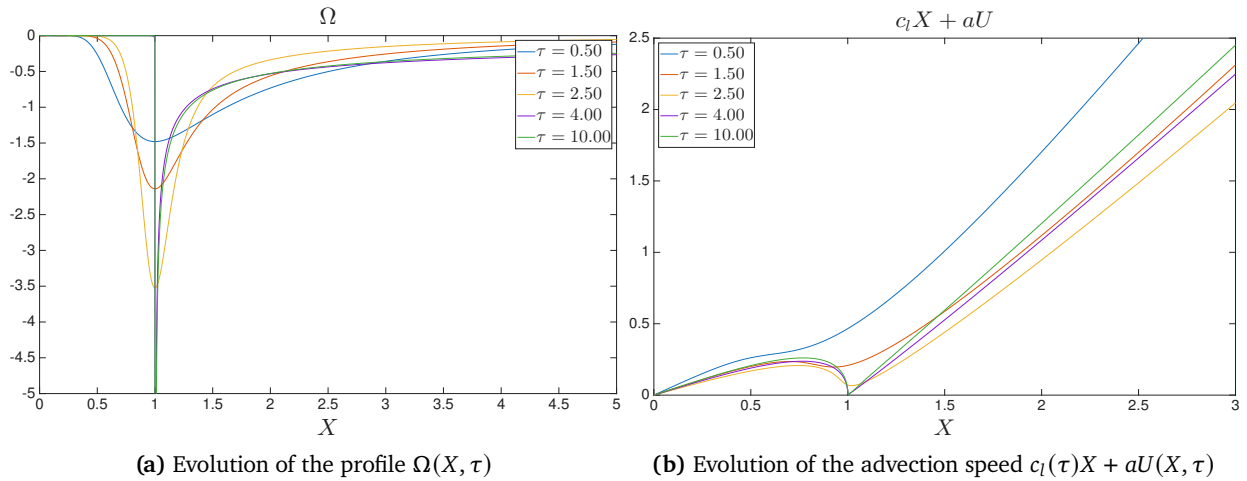


Figure 5.2: Dynamic rescaling simulation for $a = -1$ with odd-symmetric degenerate initial data supported on the whole real line (Case 1.1). We impose the normalization conditions $\partial_X \Omega(1, \tau) \equiv 0$ (pinning the minimum at $X = 1$) and $\mathbf{H}(\Omega)(0, \tau) \equiv \mathbf{H}(\Omega_0)(0)$.

In Case 1.2, by contrast, the profile stays identically zero on $[0, 1]$ for all τ . This is a direct consequence of the normalization $c_l(\tau) + aU(1, \tau) \equiv 0$, which pins the transition point at $X = 1$ and prevents transport across it. Meanwhile, Ω develops a sharp front to the right of $X = 1$, and this front travels toward the transition point as τ increases. Such behavior is also related to the structure of the advection speed $c_lX + aU$ displayed in Figure 5.3(b). In addition to the origin, $c_lX + aU$ has two other zeros on the half-line $X > 0$ before convergence, one at the fixed transition point $X = 1$ and the other located slightly to the right. The front of Ω consistently lies between these two zeros between which $c_lX + aU < 0$, and is therefore advected leftward. As $\tau \rightarrow +\infty$, the rightmost zero approaches $X = 1$, causing the front to concentrate at the transition point and producing the observed cusp-like behavior of $c_lX + aU$ near $X = 1$. Similar to Case 1.1, $c_lX + aU$ is positive beyond its rightmost zero, thus transporting the profile rightward and generating the observed tail. Numerically, the limiting profiles of Ω and $c_lX + aU$ in Cases 1.1 and 1.2 appear to coincide, suggesting the convergence to the same steady state with these two different choices of initial data and normalization conditions.

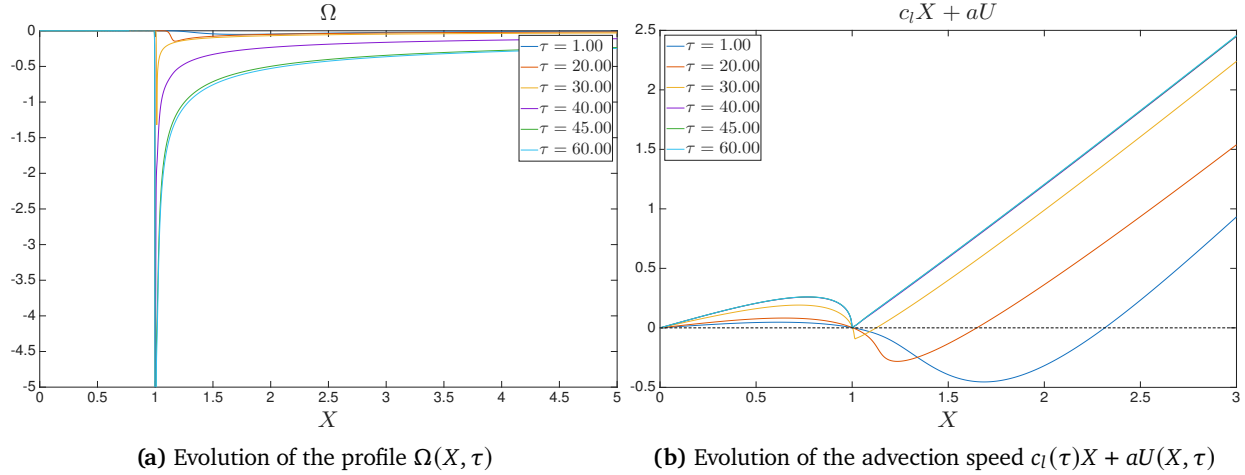


Figure 5.3: Dynamic rescaling simulation for $a = -1$ with odd-symmetric degenerate initial data that vanishes on $[-1, 1]$ (Case 1.2). We impose the normalization conditions $c_l(\tau) + aU(1, \tau) \equiv 0$ (pinning the transition point at $X = 1$) and $\mathbf{H}(\Omega)(0, \tau) \equiv \mathbf{H}(\Omega_0)(0)$.

To examine the convergence of the dynamic rescaling simulation in more detail, we use the case $a = -1$ with odd-symmetric degenerate initial data (Case 1.1) as a representative example. Figure 5.4 shows that, as $\tau \rightarrow +\infty$, the rescaled profile $\Omega(X, \tau)$ approaches a limiting shape, both in the near field (a) and in the far field (b). Meanwhile, the scaling factors $c_l(\tau)$ and $c_\omega(\tau)$, as well as the shrinking rate $\gamma(\tau) = -c_l(\tau)/c_\omega(\tau)$, converge to steady values, with limiting $\bar{c}_\omega < 0$. This stabilization provides numerical evidence that the rescaled solution approaches a steady state of (2.7), and hence corresponds to an asymptotically self-similar finite-time blowup of the original gCLM equation (1.1).

We next present numerical results for other values of $a < 0$ with odd-symmetric degenerate initial data. Specifically, we numerically solve the dynamic rescaling equation (2.7) for $a = -0.1, -0.2, \dots, -1$ in both Case 1.1 and Case 1.2, imposing the normalization conditions (5.1) and (5.2), respectively. For all these values of a , we observe convergence behavior qualitatively similar to the aforementioned case $a = -1$. To quantify convergence, we monitor the residual of the profile equation away from the singular points and declare convergence once

$$\left\| \Omega_\tau \mathbf{1}_{\{|X-1|>0.1, |X+1|>0.1\}} \right\|_{L^\infty} < 10^{-8}.$$

The resulting scaling factors for $-1 \leq a \leq -0.1$ in Case 1.1 are listed in Table 5.1. The corresponding values for Case 1.2 are nearly identical and are therefore omitted. The self-similar profiles for each a are shown in Figure 5.5.

a	-0.1	-0.2	-0.3	-0.4	-0.5
c_l	0.6189	0.7554	0.8060	0.8676	0.9580
c_ω	-0.7908	-0.8287	-0.7961	-0.7897	-0.8104
γ	0.7827	0.9114	1.0124	1.0986	1.1821
a	-0.6	-0.7	-0.8	-0.9	-1
c_l	1.0696	1.1718	1.2563	1.3576	1.4541
c_ω	-0.8368	-0.8437	-0.8455	-0.8557	-0.8634
γ	1.2782	1.3888	1.4858	1.5866	1.6841

Table 5.1: Scaling factors for $-1 \leq a \leq -0.1$ obtained from odd-symmetric degenerate initial data (Case 1.1). The corresponding values for Case 1.2 are nearly identical.

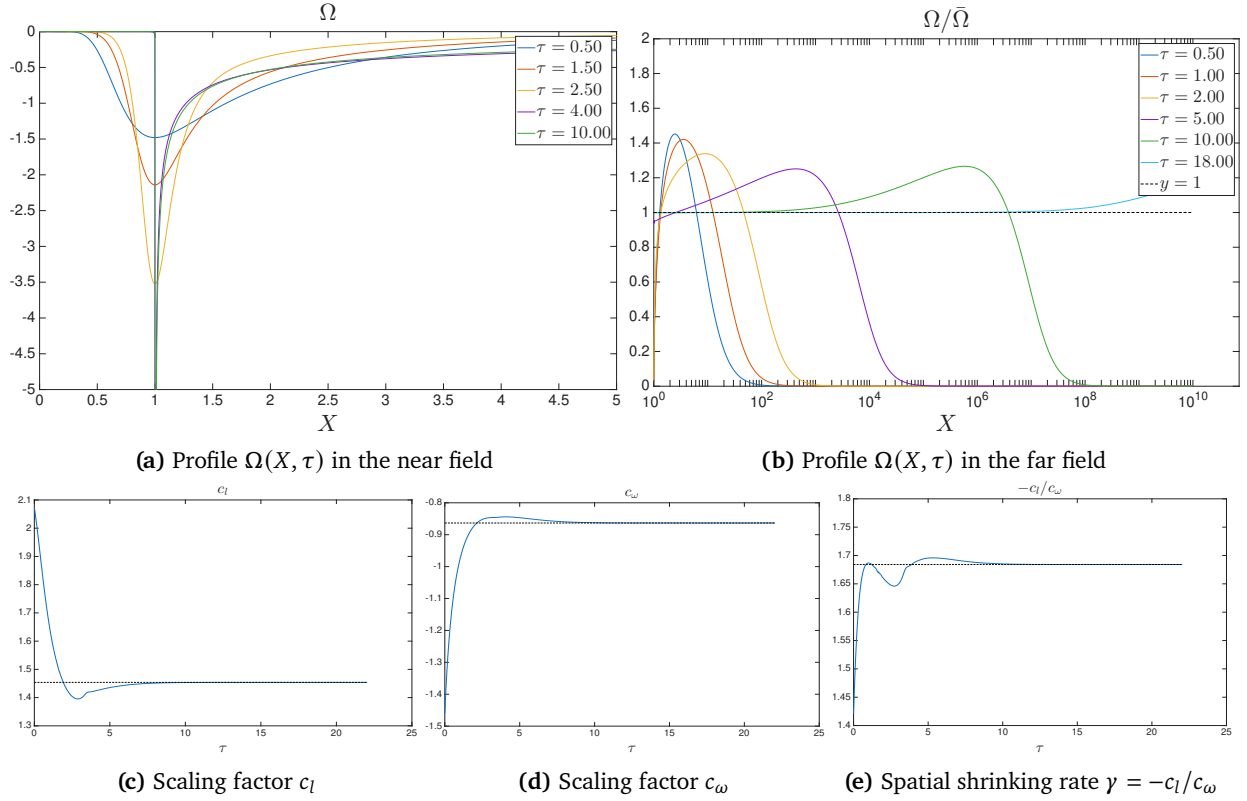


Figure 5.4: Convergence of the dynamic rescaling simulation for $a = -1$ with odd-symmetric degenerate initial data. As τ increases, the rescaled profile $\Omega(X, \tau)$ approaches a limiting shape in both the near field and the far field, while the scaling factors $c_l(\tau)$ and $c_\omega(\tau)$ (and the shrinking rate $\gamma(\tau) = -c_l(\tau)/c_\omega(\tau)$) stabilize. In (b), the reference steady profile $\bar{\Omega}(X)$ is taken to be the numerical profile at the first time when the profile equation, restricted away from the singularities, satisfies $\|\Omega_\tau \mathbf{1}_{\{|X-1|>0.1, |X+1|>0.1\}}\|_{L^\infty} < 10^{-8}$.

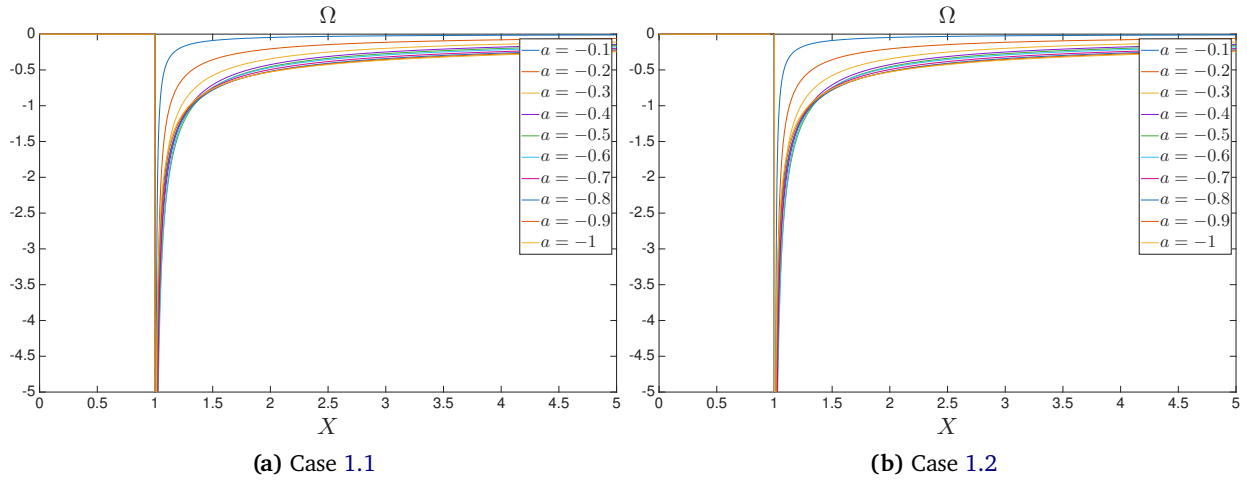


Figure 5.5: Singular limiting profiles $\bar{\Omega}(X)$ for $-1 \leq a \leq -0.1$ computed from odd-symmetric degenerate initial data. For each fixed a , the profiles obtained from Cases 1.1 and 1.2 coincide.

Figure 5.5 shows that, for each $a < 0$, the solution of the dynamic rescaling equation (2.7) converges to a self-similar profile $\bar{\Omega}(X)$ that develops singularities at $X = \pm 1$ and vanishes on $(-1, 1)$ (note that the odd symmetry of the initial data is preserved by the evolution). In Table 5.1 we also observe that the spatial shrinking rate γ increases as a becomes more negative. One possible explanation is that, as a becomes more negative, the advection term $au\omega_x$ in the original physical equation (1.1) becomes more inward-pushing, which enhances the focusing mechanism and leads to a faster spatial collapse. Moreover, for each fixed a , simulations in both Case 1.1 and Case 1.2 yield the same limiting profile and the same scaling factors up to numerical errors. This indicates that the self-similar blowup with a singular profile is robust with respect to the choice of degenerate initial data, hence suggesting stability of the observed blowup.

To conclude this subsection, we revisit and justify our choice of an initial profile with infinite vanishing order at the origin in Case 1.1. This choice is motivated by the following numerical observation for $a < 0$: under our normalization conditions, and provided the initial data vanish to at least third order at $X = 0$, all derivatives at the origin tend to zero,

$$\partial_X^j \Omega(0, \tau) \rightarrow 0 \quad \text{as } \tau \rightarrow +\infty, \quad \text{for every } j \geq 0.$$

In particular, the limiting self-similar profile $\bar{\Omega}$ appears to have infinite vanishing order at $X = 0$, regardless of the (finite) vanishing order of the initial data. To illustrate this, Figure 5.6 shows the profile evolution for $a = -1$ using the family of initial profiles

$$\Omega_0(X) = -\frac{3X^k}{3 + kX^{k+3}}, \quad k = 3, 5, 7, 9.$$

Despite the different choices of k , the corresponding solutions converge to the same limiting self-similar profile, and this limiting profile exhibits infinite vanishing order at the origin. We observe the same behavior for other negative values of a in our simulations.

5.2. Numerical results for different $a < 0$ with degenerate initial data supported inside \mathbb{R}_+ . In this subsection, we report numerical results from dynamic rescaling simulations for $a < 0$ with half-line degenerate initial data supported inside \mathbb{R}_+ (under Assumption 2.3), corresponding to Cases 2.1 and 2.2. For Case 2.1, we impose the same normalization conditions (5.1) as in Case 1.1, while for Case 2.2 we use the same normalization conditions (5.2) as in Case 1.2. Figures 5.7 and 5.8 show, for $a = -1$, the evolution of the rescaled profile $\Omega(X, \tau)$ together with the associated advection speed $c_l(\tau)X + aU(X, \tau)$. The dynamics are qualitatively analogous to those observed in the corresponding odd-symmetric cases.

Recall that for the half-line case, there is an explicit singular solution to the self-similar profile equation (2.8) given by Theorem 2.6. We briefly outline the derivation of this explicit solution here. For $\mu \in (0, 1)$ and $\theta \in [0, 2\pi)$, define a family of functions

$$\Phi_{\mu, \theta}(X) := \frac{\mathbf{1}_{\{X>0\}}(X) \cos \theta + \mathbf{1}_{\{X<0\}}(X) \cos(\theta - \pi\mu)}{|X|^\mu} = \begin{cases} |X|^{-\mu} \cos \theta & X > 0, \\ |X|^{-\mu} \cos(\theta - \pi\mu), & X < 0. \end{cases}$$

One can calculate that

$$H(\Phi_{\mu, \theta})(X) = \frac{\mathbf{1}_{\{X>0\}}(X) \sin \theta + \mathbf{1}_{\{X<0\}}(X) \sin(\theta - \pi\mu)}{|X|^\mu} = \begin{cases} |X|^{-\mu} \sin \theta & X > 0, \\ |X|^{-\mu} \sin(\theta - \pi\mu), & X < 0. \end{cases}$$

In fact, one can check that

$$\Phi_{\mu, \theta}(X) + iH(\Phi_{\mu, \theta})(X) = \varphi(X),$$

where

$$\varphi(z) = \frac{e^{i\theta}}{z^\mu},$$

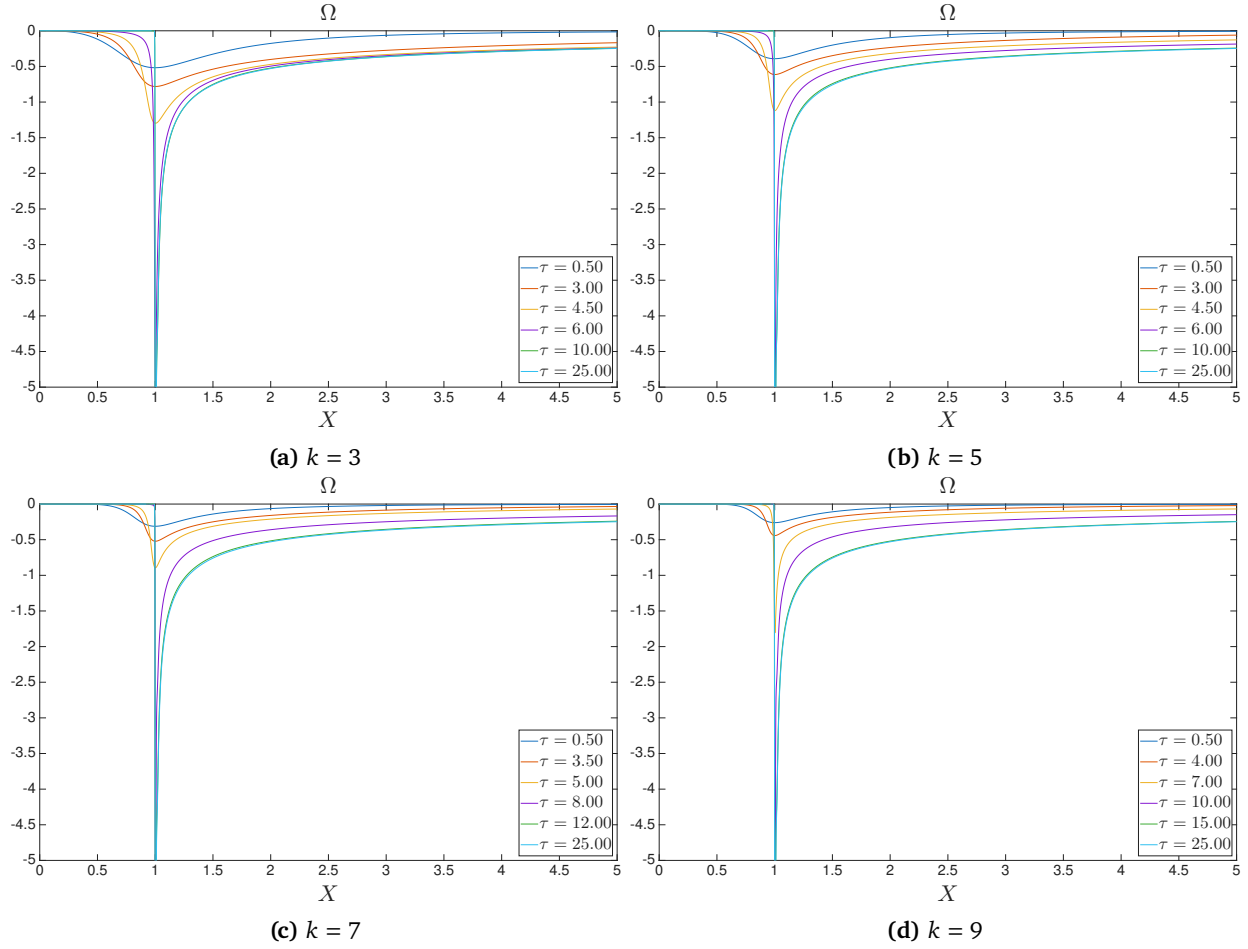


Figure 5.6: Evolution of the profile for $a = -1$ with different vanishing orders $k = 3, 5, 7, 9$ of the odd initial data. All the solutions converge to the same self-similar profile with infinite vanishing order at the origin.

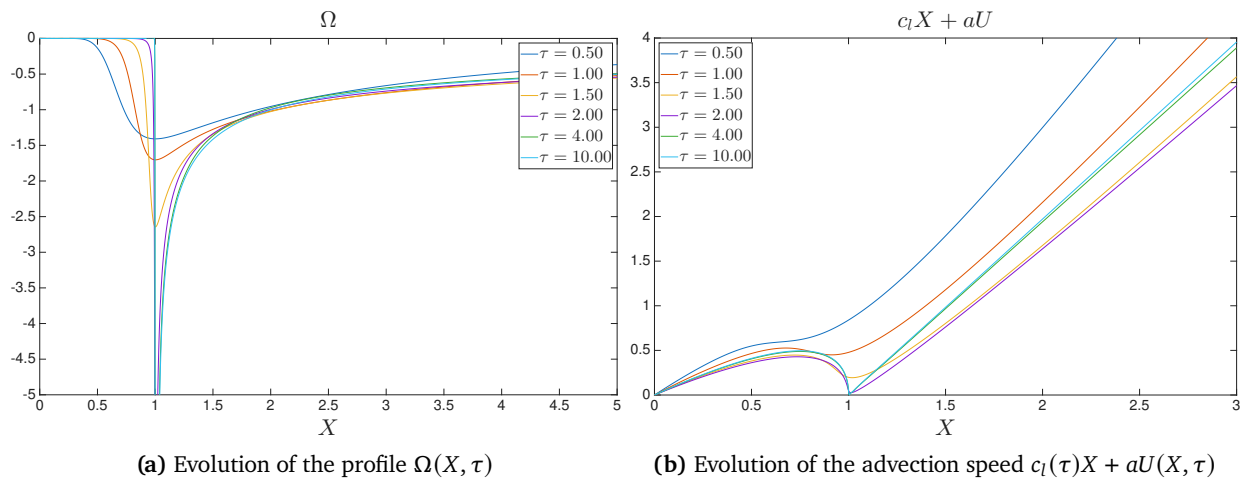


Figure 5.7: Dynamic rescaling simulation for $a = -1$ with degenerate initial data supported on the positive half-line \mathbb{R}_+ (Case 2.1). We impose the normalization conditions $\partial_X \Omega(1, \tau) \equiv 0$ (pinning the minimum at $X = 1$) and $H(\Omega)(0, \tau) \equiv H(\Omega_0)(0)$.

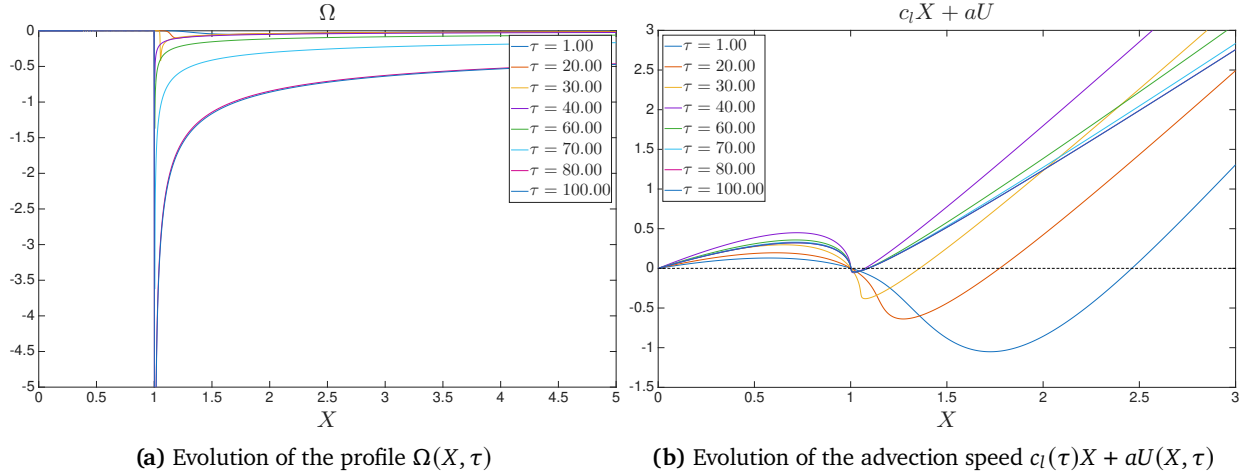


Figure 5.8: Dynamic rescaling simulation for $a = -1$ with degenerate initial data supported on $[1, +\infty)$ (Case 2.2). We impose the normalization conditions $c_l(\tau) + aU(1, \tau) \equiv 0$ (pinning the transition point at $X = 1$) and $H(\Omega)(0, \tau) \equiv H(\Omega_0)(0)$.

which is holomorphic in the interior of the upper half-space. Now, given any $a < 0$, we fix $\mu = 1/(1 - a)$ and $\theta = \pi/2$. Let

$$\bar{\Omega}_a(X) = -\Phi_{\mu, \theta}(1 - X) = -\frac{\mathbf{1}_{\{X > 1\}} \sin(\pi\mu)}{|1 - X|^\mu}. \quad (5.3)$$

Then the Hilbert transform of Ω is given by

$$H(\bar{\Omega}_a) = \frac{\mathbf{1}_{\{X < 1\}} + \mathbf{1}_{\{X > 1\}} \cos(\pi\mu)}{|1 - X|^\mu}.$$

One can verify that if we set

$$\bar{c}_{l,a} = 1 - a, \quad \bar{c}_{\omega,a} = -1, \quad (5.4)$$

then $(\bar{\Omega}_a, \bar{c}_{l,a}, \bar{c}_{\omega,a})$ solves the steady self-similar profile equation (2.8) with $\bar{\gamma}_a = -\bar{c}_{l,a}/\bar{c}_{\omega,a} = 1 - a$. See Appendix B for a detailed verification. This gives an explicit singular solution to the self-similar profile equation for each $a < 0$. In what follows, we show numerically that, for $a < 0$, the dynamic rescaling equation with half-line degenerate initial data (Cases 2.1 and 2.2) converges to the explicit singular profile (5.3) under proper normalization.

As an example, Figure 5.9 illustrates this convergence for $a = -1$ in the half-line setting (Case 2.1). As τ increases, the profile $\Omega(X, \tau)$ converges to the explicit singular profile $\bar{\Omega}_a$ in (5.3) in both the near field and the far field. At the same time, the scaling factors $c_l(\tau)$ and $c_\omega(\tau)$ stabilize and converge to the predicted (in (5.4)) steady-state values $\bar{c}_{l,a} = 1 - a = 2$ and $\bar{c}_{\omega,a} = -1$, so that the shrinking rate $\gamma(\tau) = -c_l(\tau)/c_\omega(\tau)$ converges to $\bar{\gamma} = 1 - a = 2$. Together, these observations provide numerical evidence that the dynamic rescaling evolution converges to the explicit steady state and thus corresponds to an asymptotically self-similar focusing finite-time blowup with a singular limiting profile. Note that the scalings of the limiting self-similar profile $\bar{\Omega}$ (in view of (2.9)) depend on how the initial profile Ω_0 is normalized, while the shape of the limiting profile and the limiting shrinking rate $\bar{\gamma}$ are uniquely given by (5.3) and (5.4) respectively in all our numerical tests.

For other negative values of a , we observe similar convergence of the dynamic rescaling simulation to the explicit singular profile (5.3) with the predicted scaling factors (5.4). We declare convergence when the residual of the profile equation, restricted away from the singularity at $X = 1$, drops below 10^{-8} , i.e.

$$\|\Omega_\tau \mathbf{1}_{\{|X-1| > 0.1\}}\|_{L^\infty} < 10^{-8}.$$

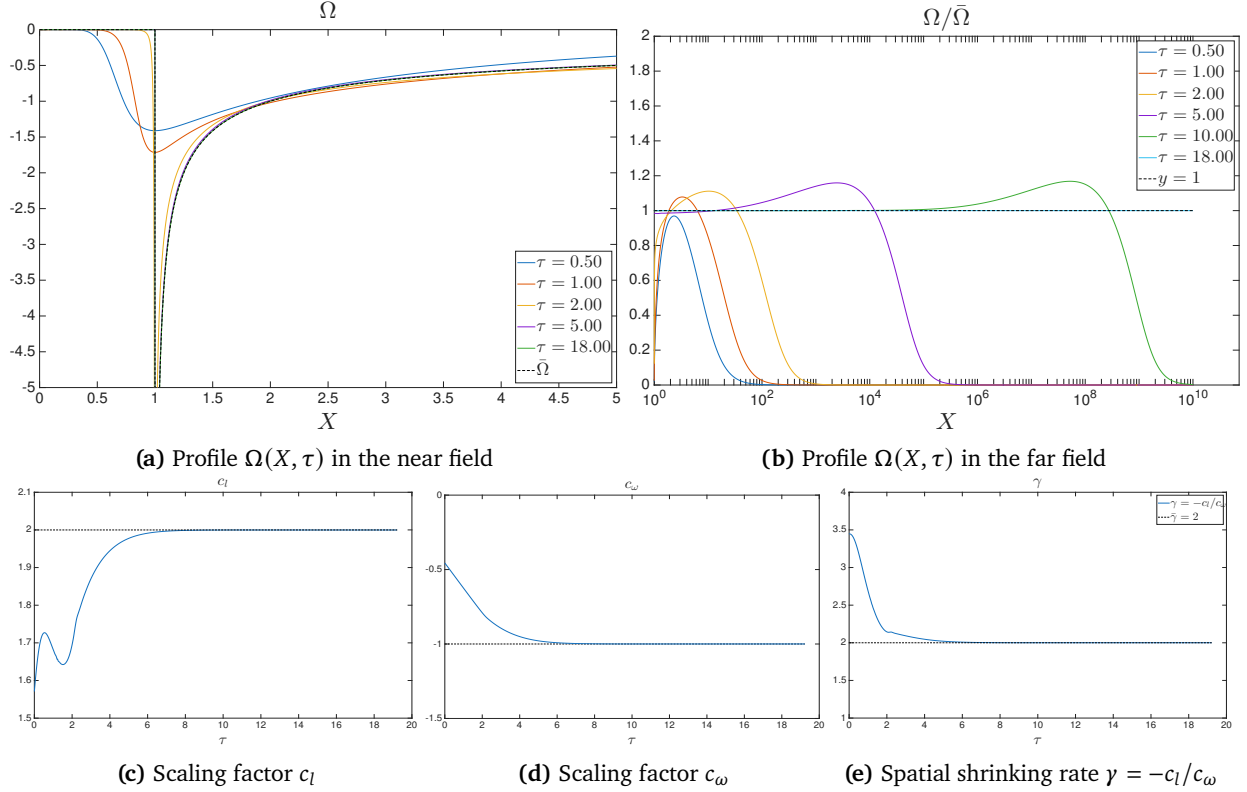


Figure 5.9: Convergence of the dynamic rescaling simulation for $a = -1$ with degenerate initial data supported on the positive half-line \mathbb{R}_+ (Case 2.1). As τ increases, the profile $\Omega(X, \tau)$ converges to the explicit singular steady profile (5.3) with $a = -1$, namely $\tilde{\Omega}(X) = -\mathbf{1}_{\{X>1\}}|1 - X|^{-1/2}$, in both the near field and the far field. Meanwhile, the scaling factors $c_l(\tau)$ and $c_\omega(\tau)$ (and hence the shrinking rate $\gamma(\tau) = -c_l(\tau)/c_\omega(\tau)$) converge to the predicted values $\bar{c}_l = 1 - a = 2$, $\bar{c}_\omega = -1$, and $\bar{\gamma} = 1 - a = 2$ given by (5.4) as $\tau \rightarrow +\infty$.

The limiting scaling factors for $-1 \leq a \leq -0.1$ in Case 2.1 are reported in Table 5.2; the results in Case 2.2 are nearly identical and are therefore not tabulated here. The corresponding limiting self-similar profiles are shown in Figure 5.10.

a	-0.1	-0.2	-0.3	-0.4	-0.5
c_l	1.1535	1.3350	1.2726	1.3846	1.5148
c_ω	-1.0588	-1.0883	-0.9654	-0.9959	-1.0142
γ	1.0895	1.2266	1.3182	1.3903	1.4936
$\bar{\gamma} = 1 - a$	1.1	1.2	1.3	1.4	1.5
a	-0.6	-0.7	-0.8	-0.9	-1
c_l	1.5997	1.6998	1.7961	1.9009	2.0000
c_ω	-0.9957	-1.0026	-0.9974	-1.0006	-1.0000
γ	1.6066	1.6954	1.8008	1.8998	2.0000
$\bar{\gamma} = 1 - a$	1.6	1.7	1.8	1.9	2

Table 5.2: Scaling factors for $-1 \leq a \leq -0.1$ obtained from half-line degenerate initial data (Case 2.1). The corresponding values for Case 2.2 are nearly identical. For each a , the converged shrinking rate γ agrees closely with the theoretical prediction $\bar{\gamma} = 1 - a$, supporting that the limiting profile is given by the explicit singular solution (5.3) with the scaling factors (5.4).

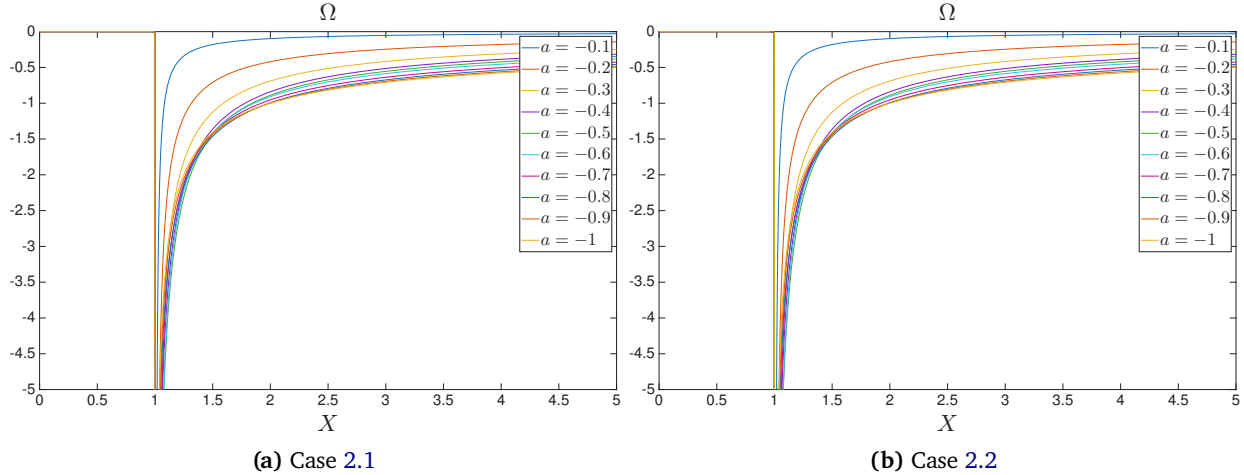


Figure 5.10: Singular one-scale profiles $\bar{\Omega}(X)$ for $-1 \leq a \leq -0.1$ computed from half-line initial data. For each fixed a , the profiles obtained from Cases 2.1 and 2.2 coincide.

Figure 5.10 suggests that, for each $a < 0$, the solution of the dynamic rescaling equation (2.7) converges to a limiting self-similar profile $\bar{\Omega}(X)$ that is singular at $X = 1$ and vanishes on $[0, 1)$. As in the odd-symmetric case, the spatial shrinking rate γ also increases as a decreases. Furthermore, the values of γ measured from the simulations are in close agreement with the theoretical prediction $\bar{\gamma} = 1 - a$, providing strong numerical evidence that the limiting profile is exactly the explicit singular solution given in (5.3) (up to rescaling) with the scaling factors in (5.4).

6. NUMERICAL INVESTIGATION OF THE TWO-SCALE FEATURE FOR $a < 0$

In this section, we present numerical evidence for the two-scale structure of the self-similar blowups with singular outer profiles, as discussed in Section 2. Recall that the two-scale scenario is described by the ansatz

$$\omega(x, t) = (T - t)^{\hat{\lambda}} \left(\widehat{\Omega} \left(\frac{x - r(t)(T - t)^{\hat{\gamma}}}{(T - t)^{\hat{\gamma}}} \right) + o(1) \right), \quad (6.1)$$

where $\widehat{\Omega}$ denotes the inner profile on the finer scale $(T - t)^{\hat{\gamma}}$. As discussed earlier, the leading-order inner dynamics suggests that $\widehat{\Omega}$ should satisfy the traveling-wave profile equation

$$(r\gamma + a\widehat{U})\widehat{\Omega}_X = \widehat{U}_X\widehat{\Omega}.$$

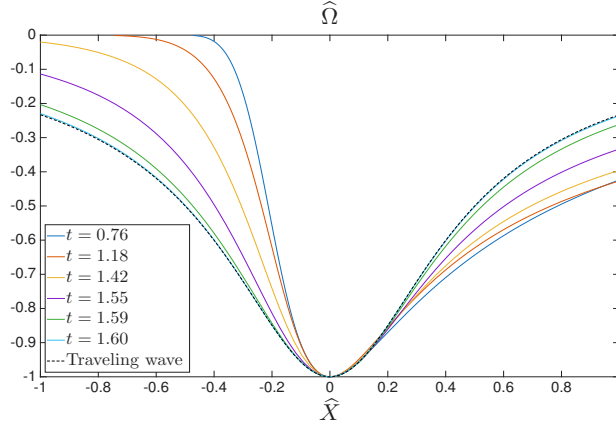
We proceed in three steps. First, we extract the inner profile from dynamic rescaling simulations by zooming in near the singular point of the outer profile, and we demonstrate that this inner profile remains smooth and converges to a stable limiting shape. Second, we compare the limiting inner profile with an independently computed traveling-wave solution obtained via an iterative method, and we find excellent agreement. This iterative method is based on our proof of the existence of traveling-wave solutions in Section 7, and detailed in Appendix C.3. The agreement supports our earlier analysis in Section 2.4 that the inner profile is governed by a traveling wave solution. Third, we fit the scaling exponents $\hat{\lambda}$, $\hat{\gamma}$, and γ in (6.1), and we verify that $\hat{\gamma} > \gamma$, i.e., the inner scale collapses faster than the outer scale, which quantitatively supports the two-scale ansatz.

6.1. Behavior of the inner profile for $a = -0.2$. We first show that an inner scale exists and converges to a steady profile. To resolve this inner-scale behavior, we zoom in near the point where the outer profile (obtained from the dynamic rescaling simulation with $a = -0.2$) attains its extremal magnitude. At each time, we translate this peak to the origin and rescale both its magnitude and spatial width

so that the resulting profile is $O(1)$ in size. More precisely, we define the normalized inner profile $\widehat{\Omega}$ (with inner coordinate \widehat{X}) by imposing the normalization

$$\widehat{\Omega}(0) = -1, \quad \left| \left\{ \widehat{X} : \widehat{\Omega}(\widehat{X}) < -0.5 \right\} \right| = 1. \quad (6.2)$$

With this normalization, $\widehat{\Omega}$ captures the local structure near the singular point of the outer profile. Numerically, we observe that $\widehat{\Omega}$ remains smooth for $\widehat{X} = O(1)$ and approaches a limiting shape as time evolves; see Figure 6.1. This provides evidence that, although the outer profile becomes singular, the solution develops a regular inner profile on a finer spatial scale. Furthermore, Figure 6.1 shows that



(a) Evolution of inner scale profile

Figure 6.1: Evolution of the inner-scale profile $\widehat{\Omega}$ for $a = -0.2$, computed from initial datum Case 1.1. The dashed line shows a traveling-wave profile obtained by the iterative method and rescaled according to (6.2). The inner-scale profile converges to the traveling-wave profile (dashed line)

the limiting inner-scale profile $\widehat{\Omega}$ matches closely the traveling-wave solution computed by the iterative method (dashed curve). This agreement provides numerical evidence supporting the two-scale ansatz (6.1).

6.2. Scaling analysis of two-scale blowup for $a = -0.2$. Here we further justify the two-scale blowup scenario for $a = -0.2$ by fitting the scaling factors $\hat{\lambda}, \hat{\gamma}$ in the two-scale ansatz (6.1). To this end, we follow the fitting method in [HH22]. Consider a solution quantity $v(t)$ that is expected to behave like a power law near the blowup time T , i.e.

$$v(t) \sim \alpha(T-t)^\eta \quad \text{as } t \rightarrow T^-, \quad (6.3)$$

where η is the power law exponent and $\alpha > 0$ is some constant. We first study the time derivative of the logarithm:

$$\frac{d}{dt} \ln v(t) = \frac{v'(t)}{v(t)} \sim \frac{-\eta\alpha(T-t)^{\eta-1}}{\alpha(T-t)^\eta} = -\frac{\eta}{T-t},$$

which naturally leads to a linear regression model

$$\text{mod}_1(t; v) := \frac{v(t)}{v'(t)} \sim -\frac{1}{\eta}(T-t) =: \tilde{a}t + \tilde{b}$$

with response variable y , explanatory variable t , and parameters \tilde{a}, \tilde{b} . We can then apply the ordinary least squares method to fit the parameters \tilde{a}, \tilde{b} and obtain an estimate of the power law exponent $\tilde{\eta} = 1/\tilde{a}$. The quality of the fit can be measured by the coefficient of determination R^2 , which is defined

as

$$R^2 = 1 - \frac{SS_{\text{err}}}{SS_{\text{tot}}}.$$

An R^2 value close to 1 indicates a high quality fitting. However, this procedure only provides a crude estimate of η , since the time derivative $v'(t)$ is computed by numerical differentiation and is subject to relatively large numerical errors. Moreover, the time step is chosen according to the CFL condition and is therefore non-uniform, which further affects the accuracy. To obtain a better approximation of η and further justify the power law behavior (6.3), we perform a local search near the crude estimate $\tilde{\eta}$ and find a finer estimate $\bar{\eta}$ by pursuing that the fitting model

$$\text{mod}_2(t; v) := v(t)^{1/\bar{\eta}} \sim \alpha^{1/\bar{\eta}}(T-t)^{\eta/\bar{\eta}} \sim \alpha^{1/\bar{\eta}}(T-t) =: \bar{a}t + \bar{b}$$

has the best linear regression fitness (the R^2) against a least-squares test. More precisely, we put a uniform mesh (with 101 points) over the interval $[\tilde{\eta} - 0.1, \tilde{\eta} + 0.1]$, compute the R^2 value for each candidate on this mesh, and select the one with the best R^2 value as our final estimate of the power law exponent $\bar{\eta}$. If $\tilde{\eta}$ falls into one of the endpoints of the interval, i.e. $\tilde{\eta} \pm 0.1$, we will perform a local search again around $\tilde{\eta}$ and update the interval to $[\tilde{\eta} - 0.1, \tilde{\eta} + 0.1]$ until $\tilde{\eta}$ is strictly inside the interval. This procedure allows us to obtain a more accurate estimate of the power law exponent η and further justify the power law behavior of $v(t)$ near the blowup time.

Although we do not directly simulate the gCLM equation (1.1) in the physical variables (x, t) , the solution in physical coordinates can be recovered by inverting the dynamic rescaling transformation (2.3). This reconstruction is used to estimate the blowup exponent $\hat{\lambda}$ and the inner-scale shrinking exponent $\hat{\gamma}$ in the two-scale ansatz (6.1). To fit $\hat{\lambda}$, we take

$$v(t) = \|\omega(\cdot, t)\|_{L^\infty}.$$

To fit $\hat{\gamma}$, we take

$$v(t) = |x_2(t) - x_1(t)|,$$

where $x_1(t) < x_2(t)$ are the two locations satisfying

$$\omega(x_1(t), t) = \omega(x_2(t), t) = -\frac{1}{2}\|\omega(\cdot, t)\|_{L^\infty}.$$

Thus $|x_2(t) - x_1(t)|$ measures the width of the thin peak (at half-maximum) and reflects the spatial size of the inner scale. We carry out the regressions over the time interval $[t_1, t_2] = [1.3, 1.55]$, which is close to the estimated blowup time $T \approx 1.6$ while still containing sufficiently many time samples for a robust fit. The fitting results are shown in Figures 6.2 and 6.3.

One can see from Figures 6.2 and 6.3 that the linear regression models match the data well, with R^2 values close to 1. This strong agreement supports the power-law behavior of $\|\omega(\cdot, t)\|_{L^\infty}$ and the thin-peak width $|x_2(t) - x_1(t)|$ as $t \rightarrow T^-$, as assumed by the two-scale ansatz (6.1). Moreover, the fitted exponent $\hat{\lambda} = -1.4691$ indicates a blowup rate faster than $(T-t)^{-1}$, while the fitted shrinking exponent $\hat{\gamma} = 1.8698$ shows that the inner scale collapses faster than the outer scale (recall $\gamma = 0.9114$ from Section 5.1). Together, these results provide further quantitative evidence for the two-scale nature of the blowup.

6.3. Scaling factors for $-1 \leq a \leq -0.1$. In this subsection, we present the scaling factors $\hat{\lambda}$, $\hat{\gamma}$, and γ of the two-scale blowup for $-1 \leq a \leq -0.1$. The parameters $\hat{\lambda}$ and $\hat{\gamma}$ are obtained by fitting the data using the procedure described in the previous subsection; the results are summarized in Table 6.1. For comparison, we also list the shrinking rate of the outer scale γ computed in Section 5.1. We observe that for all $a \in [-1, -0.1]$, the fitted factors satisfy $\hat{\lambda} < -1$, indicating that the magnitude of the solution grows faster than $(T-t)^{-1}$, and moreover $\hat{\gamma} > \gamma$, showing that the inner scale collapses faster than the outer scale. These features are consistent with the two-scale blowup scenario.

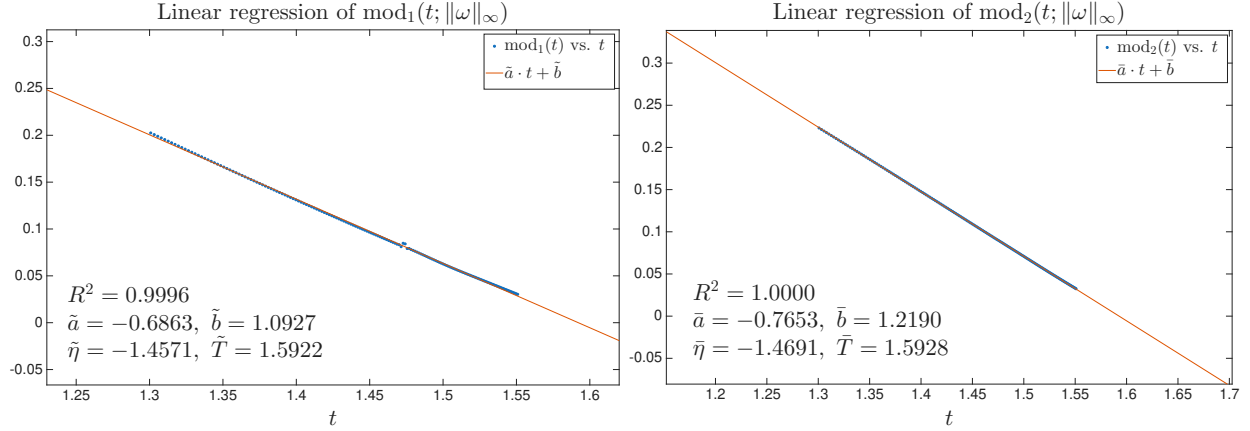


Figure 6.2: Fitting of the power law exponent η for $\|\omega(\cdot, t)\|_{L^\infty}$ with $a = -0.2$ over the time interval $[t_1, t_2] = [1.3, 1.55]$. Left: linear regression of $\text{mod}_1(t; \|\omega\|_{L^\infty})$. Right: linear regression of $\text{mod}_2(t; \|\omega\|_{L^\infty})$. The blue points are the data points obtained from our computation, and the red lines are the linear models (plotted on a larger time interval for clarity). The small jump near $t = 1.47$ is caused by an adaptive mesh update.

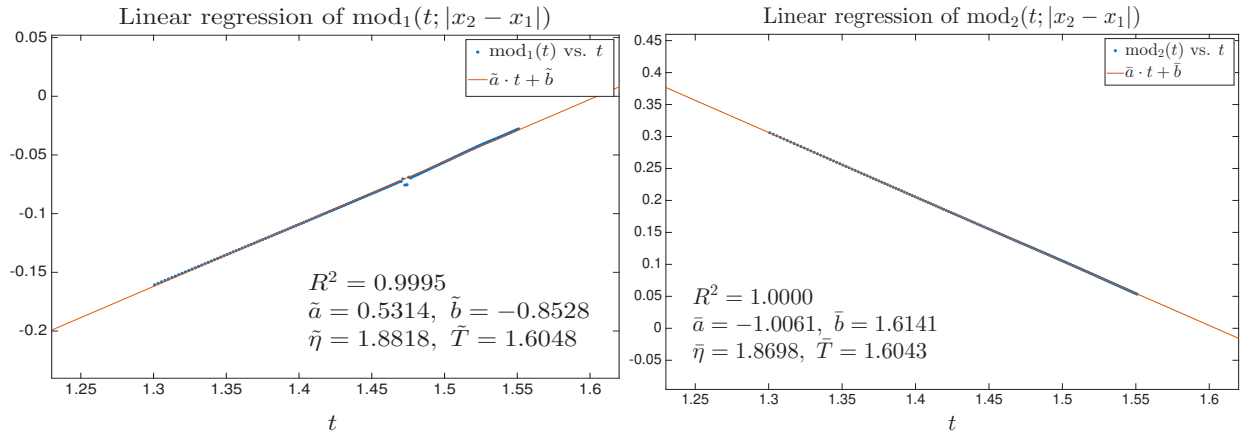


Figure 6.3: Fitting of the power law exponent η for $|x_2(t) - x_1(t)|$ with $a = -0.2$ over the time interval $[t_1, t_2] = [1.3, 1.55]$. Left: linear regression of $\text{mod}_1(t; |x_2 - x_1|)$. Right: linear regression of $\text{mod}_2(t; |x_2 - x_1|)$. The blue points are the data points obtained from our computation, and the red lines are the linear models (plotted on a larger time interval for clarity). The small jump near $t = 1.47$ is caused by an adaptive mesh update.

We also observe that, as a decreases, $|\hat{\lambda}|$ decreases (indicating a slower growth of $\|\omega(\cdot, t)\|_{L^\infty}$), while both $\hat{\gamma}$ and γ increase (indicating faster spatial collapsing on both the inner and outer scales).

7. EXISTENCE OF TRAVELING WAVE SOLUTIONS

The goal of this section is to prove the existence of traveling wave solutions for the gCLM equation (1.1) and discuss their properties. Recall that a traveling wave solution is a solution of the equation

$$(a\bar{u} - r)\bar{\omega}_{\tilde{x}} = \bar{u}_{\tilde{x}}\bar{\omega},$$

where $\tilde{x} = x - rt$ and $\bar{u}_{\tilde{x}}(\tilde{x}) = \mathbf{H}(\bar{\omega})(\tilde{x})$. For notational simplicity, we will still use ω, u, x for $\bar{\omega}, \bar{u}, \tilde{x}$ respectively. We aim to prove the existence of a solution (ω, u, r) to the profile equation

$$(au - r)\omega_x = u_x\omega, \quad u_x = \mathbf{H}(\omega) \quad (7.1)$$

a	-0.1	-0.2	-0.3	-0.4	-0.5
$\hat{\lambda}$	-1.4852	-1.4691	-1.3282	-1.2923	-1.2887
$\hat{\gamma}$	1.8577	1.8698	1.9635	2.0178	2.0678
γ	0.7827	0.9114	1.0124	1.0986	1.1821
a	-0.6	-0.7	-0.8	-0.9	-1
$\hat{\lambda}$	-1.2681	-1.2612	-1.2487	-1.2268	-1.2038
$\hat{\gamma}$	2.1580	2.2936	2.4178	2.4820	2.5562
γ	1.2782	1.3888	1.4858	1.5866	1.6841

Table 6.1: Scaling factors for $-1 \leq a \leq -0.1$. The initial data are chosen to be odd symmetric as in Case 1.1.

for all $a \in (-\infty, 1)$. For the $a = 0$ case, the profile equation (7.1) becomes

$$-r\omega_x = u_x\omega,$$

which admits an explicit solution

$$\omega(x) = \frac{1}{1+x^2}, \quad u(x) = \frac{1}{2} \ln(1+x^2), \quad r = \frac{1}{2}.$$

In general, the profile equation (7.1) is a nonlinear nonlocal equation, and it is difficult to find explicit solutions. In the remaining part of this section, we will prove the existence of non-trivial solutions to (7.1) for all $a \in (-\infty, 1)$ by a fixed-point method and discuss some properties of such solutions.

7.1. Existence of traveling wave solutions by a fixed-point method. To prove the nonlinear system (7.1) admits a non-trivial solution for each $a \in (-\infty, 1)$, we follow the idea of [HQWW24]: we reformulate the problem as a fixed-point problem of some non-linear map and then apply the Schauder fixed-point theorem to show the existence of fixed points. To this end, we need to select an appropriate function space in which we can establish the continuity and compactness of our nonlinear map.

Consider a Banach space of continuous even functions

$$\mathbb{V} := \{\omega \in C(\mathbb{R}) : \omega(-x) = \omega(x), \|\rho\omega\|_{L^\infty} < +\infty\},$$

endowed with a weighted L^∞ -norm $\|\rho\omega\|_{L^\infty}$, referred to as the L_ρ^∞ -norm, where $\rho(x) = (1+|x|)^{-1/2}$. Moreover, for each $a \in (-\infty, 1)$ we consider a closed (under the L_ρ^∞ -norm) and convex subset \mathbb{D}_a of \mathbb{V} . We define

$$\mathbb{D}_a := \{\omega \in \mathbb{V} : \omega(0) = 1, (1-x^2)_+ \leq \omega(x) \leq 1 \text{ for all } x,$$

$$\omega(x) \text{ is non-increasing on } [0, +\infty), \omega(\sqrt{s}) \text{ is convex in } s, \omega'_-(1/2) \leq -\eta_a\}.$$

Here $\eta_a = 1/(2^{9/2}(4+|a|)^3)$ is a constant depending on a , whose precise value is not important; it only matters that $\eta_a > 0$. In fact, one can check that $\omega(x) \in \mathbb{D}_a$ implies

$$(1-x^2)_+ \leq \omega(x) \leq \max\{1-\eta_a x^2, 1-\eta_a/4\} < 1, \quad x > 0,$$

where the second inequality follows from the assumptions that $\omega(\sqrt{s})$ is convex in s , $\omega'_-(1/2) \leq -\eta_a$, and $\omega(x)$ is non-increasing on $[0, +\infty)$. This avoids $\omega(x) \equiv 1$ being in \mathbb{D}_a .

Now we construct an a -dependent nonlinear map whose potential fixed points are the traveling wave solutions. For $\omega \in \mathbb{D}_a$, we first define a linear operator corresponding to the 1D Biot–Savart law in the gCLM equation

$$\mathbf{T}(\omega)(x) := (-\Delta)^{-1/2}\omega(x) = \frac{1}{\pi} \int_0^{+\infty} \ln \left| \frac{x^2 - y^2}{y^2} \right| \omega(y) dy.$$

Next, for $a \in (-\infty, 0) \cup (0, 1)$ we define

$$\mathbf{R}_a(\omega)(x) = \left(1 - \frac{aT(\omega)(x)}{r(\omega)}\right)_+^{\frac{1}{a}}, \quad \omega \in \mathbb{D}_a,$$

where

$$r(\omega) = \frac{1}{\pi} \int_0^{+\infty} \frac{\omega(0) - \omega(y)}{y^2} dy. \quad (7.2)$$

Note that $r(\omega) < +\infty$ holds for $\omega \in \mathbb{D}_a$ since $(1 - x^2)_+ \leq \omega(x) \leq 1$ for all x . For the special case $a = 0$, we define

$$\mathbf{R}_0(\omega)(x) = e^{-\frac{T(\omega)(x)}{r(\omega)}}, \quad \omega \in \mathbb{D}_0.$$

One can check that this definition is consistent with the definition of \mathbf{R}_a for $a \neq 0$ by taking the limit $a \rightarrow 0$.

We now aim to study the fixed-point problem

$$\mathbf{R}_a(\omega) = \omega, \quad \omega \in \mathbb{D}_a.$$

First we prove a proposition explaining how a fixed point of \mathbf{R}_a corresponds to a traveling wave solution.

Proposition 7.1. *For any $a \in (-\infty, 1)$, if $\omega \in \mathbb{D}_a$ is a fixed point of \mathbf{R}_a , i.e. $\mathbf{R}_a(\omega) = \omega$, then $(\omega, r(\omega))$ is a solution to the traveling wave profile equation (7.1).*

Conversely, if (ω, r) is a solution to (7.1) such that $\omega(x)$ is an even function of x , $\omega(x) \geq 0$ and $\omega'(x) \leq 0$ for all $x \geq 0$, $\omega(0) = 1$, and $\lim_{x \rightarrow 0} \omega'(x)/(2x) = -1$ (by re-normalization), then ω is a fixed point of \mathbf{R}_a , and r is related to ω as in (7.2).

Proof. If $\omega \in \mathbb{D}_a$ is a fixed point of \mathbf{R}_a , then we have

$$\omega(x) = \begin{cases} \left(1 - \frac{aT(\omega)(x)}{r(\omega)}\right)_+^{\frac{1}{a}}, & a < 1, a \neq 0, \\ e^{-\frac{T(\omega)(x)}{r(\omega)}}, & a = 0. \end{cases}$$

Such ω can be directly verified to be a solution to the profile equation (7.1) with $u = T(\omega)$ and $r = r(\omega)$.

Conversely, if $(\omega(x), r)$ is a solution to (7.1) satisfying the conditions in the proposition, then for x such that $\omega(x) \neq 0$, we have

$$\frac{\omega'}{\omega} = \frac{u'}{au - r}.$$

Solving this ODE gives

$$\omega(x) = \begin{cases} \left(1 - \frac{aT(\omega)(x)}{r(\omega)}\right)_+^{\frac{1}{a}}, & a < 1, a \neq 0, \\ e^{-\frac{T(\omega)(x)}{r(\omega)}}, & a = 0. \end{cases}$$

Moreover, we can show that

$$\lim_{x \rightarrow 0} \frac{\omega'(x)}{2x} = -1 \iff r = \frac{1}{\pi} \int_0^{+\infty} \frac{1 - \omega(y)}{y^2} dy.$$

We delay the details of showing this relation to the proof of Lemma 7.6 below. \square

7.1.1. *Properties of $r(\omega)$.* We provide an estimate of $r(\omega)$ that will be useful later.

Lemma 7.2. *For any $\omega \in \mathbb{D}_a$ and any $x > 0$,*

$$\frac{\eta_a}{\pi} \leq r(\omega) \leq \min \left\{ \frac{2(x+1)}{\pi x} (1 - \omega(x))^{1/2}, \frac{2}{\pi} \right\}.$$

Proof. The definition of \mathbb{D}_a implies that for any $x > 0$,

$$(1 - x^2)_+ \leq \omega(x) \leq \max \{1 - \eta_a x^2, 1 - \eta_a/4\} < 1.$$

Therefore, we have

$$\begin{aligned} r(\omega) &= \frac{1}{\pi} \int_0^{+\infty} \frac{1 - \omega(y)}{y^2} dy \leq \frac{1}{\pi} \int_0^1 1 dy + \frac{1}{\pi} \int_1^{+\infty} \frac{1}{y^2} dy = \frac{2}{\pi}, \\ r(\omega) &= \frac{1}{\pi} \int_0^{+\infty} \frac{1 - \omega(y)}{y^2} dy \geq \frac{1}{\pi} \int_0^{1/2} \eta_a dy + \frac{1}{\pi} \int_{1/2}^{+\infty} \frac{\eta_a}{4y^2} dy = \frac{\eta_a}{\pi}. \end{aligned}$$

Next, fix an arbitrary $x > 0$. For $0 \leq y \leq x$, $\omega(y) \geq \max\{(1 - y^2)_+, \omega(x)\}$, so $1 - \omega(y) \leq \min\{y^2, 1 - \omega(x)\}$. For $y \geq x$, the convexity of $\omega(\sqrt{s})$ implies that $(1 - \omega(y))/y^2 \leq (1 - \omega(x))/x^2$, and so $1 - \omega(y) \leq \min\{y^2(1 - \omega(x))/x^2, 1\}$. Combining these two estimates, we have

$$1 - \omega(y) \leq \min \{y^2, 1 - \omega(x)\} + \min \{y^2(1 - \omega(x))/x^2, 1\}, \quad y \geq 0.$$

We thus obtain that

$$\begin{aligned} r(\omega) &\leq \frac{1}{\pi} \int_0^{+\infty} \frac{\min \{y^2, 1 - \omega(x)\}}{y^2} dy + \frac{1}{\pi} \int_0^{+\infty} \frac{\min \{y^2(1 - \omega(x))/x^2, 1\}}{y^2} dy \\ &\leq \frac{2(x+1)}{\pi x} (1 - \omega(x))^{1/2}, \end{aligned}$$

which is the desired bound. \square

Lemma 7.3. $r(\omega) : \mathbb{D}_a \rightarrow \mathbb{R}$ is Hölder continuous in the L^∞ -norm. In particular,

$$|r(\omega_1) - r(\omega_2)| \lesssim \|\rho(\omega_1 - \omega_2)\|_{L^\infty}^{1/2},$$

for any $a \in (-\infty, 1)$ and $\omega_1, \omega_2 \in \mathbb{D}_a$.

Proof. Recall that $\rho = (1 + |x|)^{-1/2}$. Denote $\delta = \|\rho(\omega_1 - \omega_2)\|_{L^\infty} \leq 1$. Since $\omega_i \geq (1 - x^2)_+$ for $i = 1, 2$, we have

$$|\omega_1(x) - \omega_2(x)| \leq \min \{x^2, \delta(1 + |x|)^{1/2}\}.$$

Hence,

$$\begin{aligned} |r(\omega_1) - r(\omega_2)| &\leq \frac{1}{\pi} \int_0^{+\infty} \frac{|\omega_1(y) - \omega_2(y)|}{y^2} dy \leq \frac{1}{\pi} \left(\int_0^{\sqrt{\delta}} 1 dy + \int_{\sqrt{\delta}}^{+\infty} \frac{\delta(1+y)^{1/2}}{y^2} dy \right) \\ &= \frac{\sqrt{\delta}}{\pi} \left(1 + \sqrt{\sqrt{\delta} + 1} + \sqrt{\delta} \cdot \operatorname{arcsinh}(\delta^{-1/4}) \right) \leq \frac{1 + \sqrt{2} + \operatorname{arcsinh}(1)}{\pi} \sqrt{\delta}. \end{aligned}$$

This proves the lemma. \square

7.1.2. Properties of $T(\omega)$.

Lemma 7.4. For any $\omega \in \mathbb{D}_a$, $T(\omega)(0) = 0$, $T(\omega)'(x) \geq 0$ on $[0, +\infty)$, and $T(\omega)(\sqrt{s})$ is concave in s .

Proof. Taking $x = 0$ in the definition of $T(\omega)$ instantly leads to $T(\omega)(0) = 0$. To prove $T(\omega)'(x) \geq 0$, we use integration by parts to compute that

$$\begin{aligned} T(\omega)(x) &= \frac{1}{\pi} \int_0^{+\infty} \ln \left| \frac{x^2 - y^2}{y^2} \right| \omega(y) dy \\ &= \frac{1}{\pi} \int_0^{+\infty} \partial_y \left(x \ln \left| \frac{x+y}{x-y} \right| + y \ln \left| \frac{x^2 - y^2}{y^2} \right| \right) \omega(y) dy \\ &= -\frac{1}{\pi} \int_0^{+\infty} \left(x \ln \left| \frac{x+y}{x-y} \right| + y \ln \left| \frac{x^2 - y^2}{y^2} \right| \right) \omega'(y) dy. \end{aligned}$$

Therefore, we have

$$T(\omega)'(x) = -\frac{1}{\pi} \int_0^{+\infty} \ln \left| \frac{x+y}{x-y} \right| \omega'(y) dy \geq 0. \quad (7.3)$$

Next, we show that $T(\omega)(\sqrt{s})$ is concave in s . By approximation theory, we may assume that $\omega(\sqrt{s})$ is twice differentiable in s , so that the convexity of $\omega(\sqrt{s})$ is equivalent to $(\omega'(x)/x)' \geq 0$ for $x > 0$. Continuing the calculations above, we have

$$\begin{aligned} \left(\frac{T(\omega)'(x)}{x} \right)' &= -\frac{1}{\pi} \int_0^{+\infty} \partial_x \left(\frac{1}{x} \ln \left| \frac{x+y}{x-y} \right| \right) \omega'(y) dy \\ &= \frac{1}{\pi} \int_0^{+\infty} \left(\frac{2y}{x^3 - xy^2} + \frac{1}{x^2} \ln \left| \frac{x+y}{x-y} \right| \right) \omega'(y) dy \\ &= \frac{1}{\pi} \int_0^{+\infty} \left(\frac{2y^2}{x^3 - xy^2} + \frac{y}{x^2} \ln \left| \frac{x+y}{x-y} \right| \right) \frac{\omega'(y)}{y} dy \\ &= -\frac{1}{\pi} \int_0^{+\infty} \left(-\frac{y}{x} + \frac{x^2 + y^2}{2x^2} \cdot \ln \left| \frac{x+y}{x-y} \right| \right) \left(\frac{\omega'(y)}{y} \right)' dy \\ &= \frac{1}{\pi} \int_0^{+\infty} G(y/x) \left(\frac{\omega'(y)}{y} \right)' dy \leq 0, \end{aligned}$$

where the function G is defined as

$$G(t) = t - \frac{1+t^2}{2} \ln \left| \frac{1+t}{1-t} \right|. \quad (7.4)$$

The integration by parts and the final inequality follow from the properties of G collected in the next lemma. \square

Lemma 7.5. *The function G defined in (7.4) satisfies:*

- $G(0) = 0$ and $\lim_{t \rightarrow +\infty} G(t) = 0$;
- $G(t) \leq 0$ for all $t > 0$.

Proof. The identity $G(0) = 0$ is immediate. Moreover, applying L'Hôpital's rule gives

$$\lim_{t \rightarrow +\infty} G(t) = \lim_{t \rightarrow +\infty} \frac{\frac{t}{1+t^2} - \frac{1}{2} \ln \left| \frac{1+t}{1-t} \right|}{\frac{1}{1+t^2}} = \lim_{t \rightarrow +\infty} \frac{2t}{1-t^2} = 0.$$

Next, a direct computation yields

$$\left(\frac{G(t)}{1+t^2} \right)' = \frac{t^4 + 6t^2 + 1}{(t^2 + 1)^2(t+1)(t-1)}.$$

Since the numerator is positive for all t , we see that $\frac{G(t)}{1+t^2}$ is strictly decreasing on $(0, 1)$ and strictly increasing on $(1, +\infty)$. Together with

$$\lim_{t \rightarrow 0^+} \frac{G(t)}{1+t^2} = 0, \quad \lim_{t \rightarrow +\infty} \frac{G(t)}{1+t^2} = 0,$$

it follows that $\frac{G(t)}{1+t^2} \leq 0$ for all $t > 0$, and hence $G(t) \leq 0$ for all $t > 0$. \square

7.1.3. Properties of $R_a(\omega)$.

Lemma 7.6. *For any $a \in (-\infty, 1)$, R_a maps \mathbb{D}_a into itself.*

Proof. Given $\omega \in \mathbb{D}_a$, let $h(x) = R_a(\omega)(x)$. We prove this lemma through the following steps:

Step 1: Show that $h(0) = 1$ and $h'(x) \leq 0$ for $x \geq 0$. Since $T(\omega)(0) = 0$, $0 < r(\omega) < +\infty$ and $T(\omega)'(x) \leq 0$ for $x \geq 0$, we have for $a \in (-\infty, 0) \cup (0, 1)$

$$h(0) = \left(1 - \frac{aT(\omega)(0)}{r(\omega)}\right)_+^{\frac{1}{a}} = 1,$$

and

$$h'(x) = -\frac{T(\omega)'(x)}{r(\omega)} \left(1 - \frac{aT(\omega)(x)}{r(\omega)}\right)_+^{\frac{1}{a}-1} \leq 0.$$

It is also straightforward to verify that $h(0) = 1$ and $h'(x) \leq 0$ for the $a = 0$ case. Note that, if h is compactly supported on $[-L, L]$ for some $L > 0$, then $h'(x) = 0$ for $x > L$, $h'(L-) \leq 0$, and $h'(L+) = 0$.

Step 2: Show that $h(\sqrt{s})$ is convex in s . We only need to show that $(h'(x)/x)'$ is non-negative on $[0, +\infty)$. Continuing the calculations in step 1, we reach for $a \in (-\infty, 0) \cup (0, 1)$

$$\left(\frac{h'(x)}{x}\right)' = \left(1 - \frac{aT(\omega)(x)}{r(\omega)}\right)_+^{\frac{1}{a}-2} \left(-\frac{1}{r(\omega)} \left(\frac{T(\omega)'(x)}{x}\right)' \left(1 - \frac{aT(\omega)(x)}{r(\omega)}\right)_+ + \frac{1-a}{x} \left(\frac{T(\omega)'(x)}{r(\omega)}\right)^2\right) \geq 0,$$

as we have proved that $(T(\omega)'(x)/x)' \leq 0$ for $x \geq 0$. Similarly, for the special case $a = 0$ we have

$$\left(\frac{h'(x)}{x}\right)' = \left(-\frac{1}{r(\omega)} \left(\frac{T(\omega)'(x)}{x}\right)' + \frac{1}{x} \left(\frac{T(\omega)'(x)}{r(\omega)}\right)^2\right) e^{-\frac{T(\omega)(x)}{r(\omega)}} \geq 0.$$

Step 3: Show that $(1-x^2)_+ \leq h(x) \leq 1$. The fact that $h(x) \leq 1$ follows directly from step 1. To prove that $h(x) \geq (1-x^2)_+$, namely $h(\sqrt{s}) \geq (1-s)_+$ for $s \geq 0$, we only need to show that

$$\lim_{x \rightarrow 0} \frac{h'(x)}{2x} = \frac{d}{ds} h(\sqrt{s}) \Big|_{s=0} = -1$$

and then use the fact that $h(\sqrt{s})$ is convex in s (step 2). We can compute that

$$\lim_{x \rightarrow 0} \frac{T(\omega)'(x)}{x} = -\frac{1}{\pi} \lim_{x \rightarrow 0} \int_0^{+\infty} \frac{1}{x} \ln \left| \frac{x+y}{x-y} \right| \omega'(y) dy = -\frac{2}{\pi} \int_0^{+\infty} \frac{\omega'(y)}{y} dy = 2r(\omega) \quad (7.5)$$

since

$$r(\omega) = \frac{1}{\pi} \int_0^{+\infty} \frac{\omega(0) - \omega(y)}{y^2} dy.$$

Hence

$$\lim_{x \rightarrow 0} \frac{h'(x)}{2x} = -\frac{1}{2r(\omega)} \lim_{x \rightarrow 0} \frac{T(\omega)'(x)}{x} = -1. \quad (7.6)$$

Step 4: Show that $h'_-(1/2) \leq -\eta_a$. We first show that $h'(x)$ can be bounded in terms of $T(\omega)'(x)$. Using (7.5) and the fact that $T(\omega)(\sqrt{s})$ is concave in s , we have

$$T(\omega)(x) \leq T(\omega)(0) + r(\omega)x^2 = r(\omega)x^2.$$

Note that $T(\omega)(x) \geq 0$ for $x \geq 0$, thus for $a \leq 1$ we always have

$$(1 - |a|x^2)_+ \leq \left(1 - \frac{aT(\omega)(x)}{r(\omega)}\right)_+ \leq 1 + |a|x^2.$$

Combining (7.6) and the convexity of $h(\sqrt{s})$ leads to $h(x) \geq (1 - x^2)_+$ for $x \geq 0$. It follows that

$$h'(x) = -\frac{T(\omega)'(x)}{r(\omega)}h(x) \cdot \left(1 - \frac{aT(\omega)(x)}{r(\omega)}\right)_+^{-1} \leq -\frac{(1 - x^2)T(\omega)'(x)}{r(\omega)(1 + |a|x^2)}, \quad x \in [0, 1].$$

Next, we lower bound $T(\omega)'(x)$ in two ways. On one hand, by the monotonicity of $\omega'(x)/x$,

$$\begin{aligned} T(\omega)'(x) &= \frac{1}{\pi} \int_0^{+\infty} \ln \left| \frac{x+y}{x-y} \right| (-\omega'(y)) dy \geq \frac{1}{\pi} \int_0^x \ln \left| \frac{x+y}{x-y} \right| (-\omega'(y)) dy \\ &\geq \frac{1}{\pi} \int_0^x \ln \left| \frac{x+y}{x-y} \right| y \cdot \frac{-\omega'(x)}{x} dy = -\frac{x\omega'(x)}{\pi} \int_0^1 t \ln \left| \frac{1+t}{1-t} \right| dt = -\frac{x\omega'(x)}{\pi}. \end{aligned}$$

On the other hand, for any $0 < z < x$ we have

$$\begin{aligned} T(\omega)'(x) &\geq \frac{1}{\pi} \int_0^x \ln \left| \frac{x+y}{x-y} \right| (-\omega'(y)) dy \geq \frac{1}{\pi} \int_0^x \frac{2y}{x} (-\omega'(y)) dy \\ &\geq \frac{2}{\pi} \int_z^x \frac{z}{x} (-\omega'(y)) dy = \frac{2}{\pi} \cdot \frac{z}{x} (\omega(z) - \omega(x)) \geq \frac{2z}{\pi x} (1 - z^2 - \omega(x)). \end{aligned}$$

We then choose $z = ((1 - \omega(x))/2)^{1/2}$ to obtain

$$T(\omega)'(x) \geq \frac{1}{\sqrt{2\pi x}} (1 - \omega(x))^{3/2}.$$

Putting these together, we reach

$$T(\omega)'(x) \geq \left(\frac{1}{\sqrt{2\pi x}} \right)^{1/3} (1 - \omega(x))^{1/2} \cdot \left(\frac{x|\omega'(x)|}{\pi} \right)^{2/3} = \frac{1}{\pi} \left(\frac{x}{\sqrt{2}} \right)^{1/3} |\omega'(x)|^{2/3} (1 - \omega(x))^{1/2}.$$

Finally, by Lemma 7.2 we have

$$h'(x) \leq -\frac{(1 - x^2)T(\omega)'(x)}{r(\omega)(1 + |a|x^2)} \leq -\frac{x^{4/3}(1 - x)}{2^{7/6}(1 + |a|x^2)} |\omega'(x)|^{2/3}.$$

Plugging in $x = 1/2$ and using that $\omega'(1/2) \leq -\eta_a$ yields $h'(1/2) \leq -\eta_a^{1/3} |\omega'(1/2)|^{2/3} \leq -\eta_a$.

Combining these steps proves the lemma. \square

Next, we show that \mathbf{R}_a is continuous on \mathbb{D}_a in the L_ρ^∞ -topology.

Theorem 7.7. *For any $a \in (-\infty, 1)$, $\mathbf{R}_a : \mathbb{D}_a \rightarrow \mathbb{D}_a$ is continuous with respect to the L_ρ^∞ -norm.*

Proof. Recall that $\rho(x) = (1 + |x|)^{-1/2}$. Given any (fixed) $\omega_0 \in \mathbb{D}_a$, we only need to prove that \mathbf{R}_a is L_ρ^∞ -continuous at ω_0 . Let $\epsilon > 0$ be an arbitrarily small number. Since $\mathbf{R}_a(\omega_0)$ is bounded, continuous, and non-increasing on $[0, +\infty)$, there is some $X_0 > 1$ such that

$$\rho(X_0)\mathbf{R}_a(\omega_0)(X_0) = \epsilon.$$

This also means $\rho(x)\mathbf{R}_a(\omega_0)(x) \leq \epsilon$ for all $x \geq X_0$.

Let $\omega \in \mathbb{D}_a$ be an arbitrary function such that $\|\rho(\omega - \omega_0)\|_{L^\infty} \leq \delta$ for some sufficiently small $\delta > 0$. For any $x \geq 0$, we have

$$\begin{aligned} |\mathbf{T}(\omega)(x) - \mathbf{T}(\omega_0)(x)| &= \frac{1}{\pi} \left| \int_0^{+\infty} \ln \left| \frac{x^2 - y^2}{y^2} \right| \cdot (\omega(y) - \omega_0(y)) \right| dy \\ &\leq \frac{1}{\pi} \int_0^{+\infty} \left| \ln \left| \frac{x^2 - y^2}{y^2} \right| \cdot \delta(1+y)^{1/2} \right| dy \\ &= \frac{\delta}{\pi} \cdot x \int_0^{+\infty} \left| \ln \left| \frac{1-t^2}{t^2} \right| \right| \cdot (1+tx)^{1/2} dt \\ &\leq \frac{\delta}{\pi} \cdot x(1+x)^{1/2} \int_0^{+\infty} \left| \ln \left| \frac{1-t^2}{t^2} \right| \right| \cdot (1+t)^{1/2} dt \\ &\lesssim \delta x(1+x)^{1/2}. \end{aligned}$$

The last integral of t above is finite since $\ln |(1-t^2)/t^2| \sim -2 \ln t$ as $t \rightarrow 0$ and $\ln |(1-t^2)/t^2| = O(t^{-2})$ as $t \rightarrow +\infty$. Recall that for any $\omega \in \mathbb{D}_a$ we have $\omega(x) \leq 1$, so a similar argument shows that $|\mathbf{T}(\omega)(x)|, |\mathbf{T}(\omega_0)(x)| \lesssim x$. Combining these estimates with Lemma 7.2 and Lemma 7.3, we obtain

$$\begin{aligned} \left| \frac{\mathbf{T}(\omega)(x)}{r(\omega)} - \frac{\mathbf{T}(\omega_0)(x)}{r(\omega_0)} \right| &\leq \left(\left| \frac{\mathbf{T}(\omega) - \mathbf{T}(\omega_0)}{r(\omega_0)} \right| + \left| \frac{\mathbf{T}(\omega)}{r(\omega)r(\omega_0)} \right| \cdot |r(\omega) - r(\omega_0)| \right) \\ &\lesssim (\delta x(1+x)^{1/2} + \delta^{1/2}x) \lesssim \delta^{1/2}x(1+x)^{1/2}. \end{aligned}$$

For the general case $a \in (-\infty, 0) \cup (0, 1)$, we denote

$$g_0 := \left(1 - \frac{a\mathbf{T}(\omega_0)(x)}{r(\omega_0)} \right)_+, \quad g := \left(1 - \frac{a\mathbf{T}(\omega)(x)}{r(\omega)} \right)_+.$$

Then it follows directly

$$|g(x) - g_0(x)| \leq |a| \cdot \left| \frac{\mathbf{T}(\omega)(x)}{r(\omega)} - \frac{\mathbf{T}(\omega_0)(x)}{r(\omega_0)} \right| \lesssim |a| \delta^{1/2} x(1+x)^{1/2},$$

which implies that, for $x \in [0, X_0]$,

$$\begin{aligned} \rho(x) |\mathbf{R}_a(\omega)(x) - \mathbf{R}_a(\omega_0)(x)| &\leq \rho(x) \left| g^{1/a}(x) - g_0^{1/a}(x) \right| \\ &\leq \frac{1}{|a|} \rho(x) |g(x) - g_0(x)| \cdot \left(g^{(1-a)/a}(x) + g_0^{(1-a)/a}(x) \right) \\ &\lesssim \delta^{1/2} x \leq \delta^{1/2} X_0, \end{aligned}$$

since $g, g_0 \leq 1$ when $a \in (0, 1)$, and $g, g_0 \geq 1$ when $a \in (-\infty, 0)$. As for the case $a = 0$, we have

$$\begin{aligned} \rho(x) |\mathbf{R}_0(\omega)(x) - \mathbf{R}_0(\omega_0)(x)| &= \rho(x) \left| e^{-\frac{\mathbf{T}(\omega)(x)}{r(\omega)}} - e^{-\frac{\mathbf{T}(\omega_0)(x)}{r(\omega_0)}} \right| \leq \rho(x) \left| \frac{\mathbf{T}(\omega)(x)}{r(\omega)} - \frac{\mathbf{T}(\omega_0)(x)}{r(\omega_0)} \right| \\ &\lesssim \delta^{1/2} x \leq \delta^{1/2} X_0. \end{aligned}$$

The first inequality comes from $\mathbf{T}(\omega)/r(\omega), \mathbf{T}(\omega_0)/r(\omega_0) \geq 0$. Hence we have $\rho(x) |\mathbf{R}_a(\omega)(x) - \mathbf{R}_a(\omega_0)(x)| \lesssim \delta^{1/2} X_0$ for any $a \in (-\infty, 1)$. Again, provided that δ is sufficiently small, we can have $\rho(X_0) \mathbf{R}_a(\omega)(X_0) \leq 2\epsilon$. By the monotonicity of $\mathbf{R}_a(\omega)$, we also have $\rho(x) \mathbf{R}_a(\omega)(x) \leq 2\epsilon$ for all $x \geq X_0$. Therefore, we can choose δ small enough ($\delta \lesssim \epsilon^2 X_0^{-2}$) such that

$$\|\rho(\mathbf{R}_a(\omega) - \mathbf{R}_a(\omega_0))\|_{L^\infty} \lesssim \epsilon$$

for all $\omega \in \mathbb{D}_a$ with $\|\rho(\omega - \omega_0)\|_{L^\infty} \leq \delta$. This proves the L^∞ -continuity of \mathbf{R}_a at ω_0 . \square

One last ingredient for establishing the existence of a fixed point of \mathbf{R}_a is the compactness of the set \mathbb{D}_a .

Lemma 7.8. *For any $a \in (-\infty, 1)$, \mathbb{D}_a is compact in the L_ρ^∞ -topology.*

Proof. For any $\omega \in \mathbb{D}_a$, we use convexity and monotonicity to obtain

$$-\frac{\omega'(x)}{2x} \leq \frac{\omega(0) - \omega(x)}{x^2} \leq \min \left\{ 1, \frac{1}{x^2} \right\}, \quad x > 0, \quad (7.7)$$

implying that $|\omega'(x)| \leq \min \{2x, 2x^{-1}\} \leq 2$. Based on this, we show that \mathbb{D}_a is sequentially compact.

Let $\{\omega_n\}_{n=1}^{+\infty}$ be an arbitrary sequence in \mathbb{D}_a . Initialize $n_{0,k} = k$, $k \geq 1$. For each integer $m \geq 1$, let $\epsilon_m = 2^{-m}$, and $L_m = \epsilon_m^{-2}$. It follows that $\rho(x)\omega_n(x) \leq \rho(x) \leq \epsilon_m$ for all $x \geq L_m$. Furthermore, since $|\omega'_n(x)| \leq 2$ on $[0, L_m]$, we can apply Ascoli's theorem to obtain a subsequence $\{\omega_{n_{m,k}}\}_{k=1}^{+\infty}$ of $\{\omega_{n_{m-1,k}}\}_{k=1}^{+\infty}$ such that $\|\rho(\omega_{n_{m,i}} - \omega_{n_{m,j}})\|_{L^\infty} \leq 2\epsilon_m$ for any $i, j \geq 1$. Then the diagonal sub-sequence $\{\omega_{n_{m,m}}\}_{m=1}^{+\infty}$ is a Cauchy sequence in the L_ρ^∞ -norm. This proves that \mathbb{D}_a is sequentially compact. \square

We are now ready to prove the existence of fixed points of \mathbf{R}_a for any $a \in (-\infty, 0) \cup (0, 1)$ using the Schauder fixed-point theorem.

Theorem 7.9. *For any $a \in (-\infty, 1)$, there exists a fixed point $\omega_a \in \mathbb{D}_a$ of \mathbf{R}_a , i.e. $\mathbf{R}_a(\omega_a) = \omega_a$. As a corollary, for any $a \in (-\infty, 1)$, (7.1) admits a solution (ω_a, r_a) with $r_a = r(\omega_a)$.*

Proof. By Theorem 7.7 and Lemma 7.8, \mathbb{D}_a is convex, closed and compact in the L_ρ^∞ -norm, and \mathbf{R}_a continuously maps \mathbb{D}_a into itself. The Schauder fixed-point theorem then implies that there exists a fixed point $\omega_a \in \mathbb{D}_a$ such that $\mathbf{R}_a(\omega_a) = \omega_a$. The corollary follows from Proposition 7.1. \square

7.2. Properties of the traveling wave solution $\omega(x)$.

7.2.1. *Explicit solution for the $a = 0$ case.* In this subsection, we will show that the only fixed point of \mathbf{R}_0 is the explicit solution

$$\omega(x) = \frac{1}{1+x^2}.$$

Let ω_0 be a fixed point of \mathbf{R}_0 . Then the convexity of $\omega_0(\sqrt{s})$ implies that $\omega_0(x)$ is differentiable almost everywhere, and

$$\omega_0(x) = \mathbf{R}_0(\omega_0)(x) = e^{-\frac{T(\omega_0)(x)}{r(\omega_0)}}$$

implies that ω_0 does not have any zero on \mathbb{R} . Therefore, by the result established in [HQW25] we have

$$\omega_0(x) = \frac{2cr(\omega_0)}{1+c^2x^2}$$

for some constant $c > 0$. Recall that we have shown $\omega_0(0) = 1$ and $\lim_{x \rightarrow 0} \omega'_0(x)/(2x) = -1$ in the proof of Lemma 7.6, it then directly follows that $2cr(\omega_0) = 1$ and $c = 1$. Hence we have $\omega_0(x) = 1/(1+x^2)$.

7.2.2. *Asymptotic behavior.* Here we classify and characterize the tail behavior of the fixed point $\omega(x)$ as $x \rightarrow +\infty$ depending on the sign of parameter a . One interesting phenomenon is that the decay rate of $\omega(x)$ shows a jump discontinuity at $a = 0$: the limit of decay rate is -1 as $a \rightarrow 0$ from below, while the decay rate is -2 for the $a = 0$ case.

Theorem 7.10. *Let ω be a fixed point of \mathbf{R}_a for some $a \in (-\infty, 1)$. Then, one of the following happens:*

- (1) $a < 0$: there exist constants $\bar{C}_a, \tilde{C}_a > 0$ depending on a such that $\bar{C}_a x^{-1/(1+|a|)} \leq \omega(x) \leq \tilde{C}_a x^{-1/(1+|a|)}$ for all $x \geq 1$.
- (2) $a = 0$: $\omega(x) \sim x^{-2}$ as $x \rightarrow +\infty$.

(3) $0 < a < 1$: ω is compactly supported on $[-L_\omega, L_\omega]$, where $L_\omega := \sup\{x : f(x) > 0\}$.

Proof. The asymptotic behavior of the $a = 0$ case directly follows from the explicit solution $\omega(x) = 1/(1+x^2)$. Hence we only need to prove the first and third cases.

(1): We first show that $\omega'(x) < 0$ for all $x > 0$. Recall that if $\omega \in \mathbb{D}_a$ is a fixed point of \mathbf{R}_a , we have

$$\omega(x) = \left(1 - \frac{a\mathbf{T}(\omega)(x)}{r(\omega)}\right)_+^{\frac{1}{a}} = \left(1 + \frac{|a|\mathbf{T}(\omega)(x)}{r(\omega)}\right)^{-\frac{1}{|a|}},$$

here the subscript $+$ is omitted since $1 + |a|\mathbf{T}(\omega)(x)/r(\omega) \geq 1$. Then we have

$$\omega'(x) = -\frac{\mathbf{T}(\omega)'(x)}{r(\omega)} \left(1 + \frac{|a|\mathbf{T}(\omega)(x)}{r(\omega)}\right)^{-\frac{1+|a|}{|a|}}.$$

We can use the calculations in the proof of Lemma 7.6 to show that for any $x > 0$,

$$\begin{aligned} \mathbf{T}(\omega)'(x) &= \frac{1}{\pi} \int_0^{+\infty} \ln \left| \frac{x+y}{x-y} \right| (-\omega'(y)) \, dy \geq \frac{1}{\pi} \int_0^{1/2} \ln \left| \frac{x+y}{x-y} \right| (-\omega'(y)) \, dy \\ &\geq \frac{1}{\pi} \int_0^{1/2} y \ln \left| \frac{x+y}{x-y} \right| \cdot (-2\omega'(1/2)) \, dy \geq \frac{2\eta_a x^2}{\pi} \int_0^{\frac{1}{2x}} \ln \left| \frac{1+t}{1-t} \right| \, dt > 0, \end{aligned}$$

which leads to $\omega'(x) < 0$ for all $x > 0$.

Next we prove the lower and upper bounds of $\omega(x)$. Similarly we have

$$\begin{aligned} \mathbf{T}(\omega)'(x) &= \frac{1}{\pi} \int_0^{+\infty} \ln \left| \frac{x+y}{x-y} \right| (-\omega'(y)) \, dy \geq \frac{1}{\pi} \int_0^x \ln \left| \frac{x+y}{x-y} \right| (-\omega'(y)) \, dy \\ &\geq \frac{1}{\pi} \int_0^x y \ln \left| \frac{x+y}{x-y} \right| \cdot \left(-\frac{\omega'(x)}{x}\right) \, dy = -\frac{x\omega'(x)}{\pi} \int_0^1 \ln \left| \frac{1+t}{1-t} \right| \, dt = -\frac{x\omega'(x)}{\pi}, \end{aligned}$$

hence

$$-\omega'(x) = \frac{\mathbf{T}(\omega)'(x)}{r(\omega)} \left(1 + \frac{|a|\mathbf{T}(\omega)(x)}{r(\omega)}\right)^{-\frac{1+|a|}{|a|}} \geq -\frac{x\omega'(x)}{\pi r(\omega)} \left(1 + \frac{|a|\mathbf{T}(\omega)(x)}{r(\omega)}\right)^{-\frac{1+|a|}{|a|}},$$

which provides the upper bound

$$\omega(x) = \left(1 + \frac{|a|\mathbf{T}(\omega)(x)}{r(\omega)}\right)^{-\frac{1}{|a|}} \leq \left(\frac{x}{\pi r(\omega)}\right)^{-\frac{1}{1+|a|}} \leq \left(\frac{x}{2\eta_a}\right)^{-\frac{1}{1+|a|}}.$$

On the other hand, by the definition of $\mathbf{T}(\omega)$,

$$\begin{aligned} \mathbf{T}(\omega)(x) &= \frac{1}{\pi} \int_0^{+\infty} \ln \left| \frac{x^2 - y^2}{y^2} \right| \omega(y) \, dy \leq \frac{1}{\pi} (2\eta_a x)^{-\frac{1}{1+|a|}} \int_0^{+\infty} \ln \left| \frac{x^2 - y^2}{y^2} \right| \left(\frac{y}{x}\right)^{-\frac{1}{1+|a|}} \, dy \\ &= \frac{1}{\pi} (2\eta_a)^{-\frac{1}{1+|a|}} x^{\frac{|a|}{1+|a|}} \int_0^{+\infty} \ln \left| \frac{1-t^2}{t^2} \right| t^{-\frac{1}{1+|a|}} \, dt. \end{aligned}$$

Denote

$$C_a = \frac{1}{\pi} (2\eta_a)^{-\frac{1}{1+|a|}} \int_0^{+\infty} \ln \left| \frac{1-t^2}{t^2} \right| t^{-\frac{1}{1+|a|}} \, dt,$$

we have

$$\omega(x) \geq \left(1 + \frac{|a|C_a x^{\frac{|a|}{1+|a|}}}{r(\omega)}\right)^{-\frac{1}{|a|}} \geq \left(x^{\frac{|a|}{1+|a|}} + \frac{|a|C_a \pi x^{\frac{|a|}{1+|a|}}}{\eta_a}\right)^{-\frac{1}{|a|}} = \left(1 + \frac{|a|C_a \pi}{\eta_a}\right)^{-\frac{1}{|a|}} x^{-\frac{1}{1+|a|}}$$

for all $x \geq 1$. We have used Lemma 7.2 to bound $r(\omega)$ from below.

(3): By the convexity of $\omega(\sqrt{s})$ and $\omega'(1/2) \leq -\eta_a$, we have for $0 < x < 1/2$,

$$\omega'(x) \leq 2\omega'(1/2)x \leq -2\eta_a x,$$

which implies that

$$T(\omega)'(x) = \frac{1}{\pi} \int_0^{+\infty} \ln \left| \frac{x+y}{x-y} \right| (-\omega'(y)) dy \geq \frac{1}{\pi} \int_0^{1/2} \ln \left| \frac{x+y}{x-y} \right| (2\eta_a y) dy,$$

hence

$$\begin{aligned} T(\omega)(x) &\geq \frac{1}{\pi} \int_0^{1/2} \left(x \ln \left| \frac{x+y}{x-y} \right| + y \ln \left| \frac{x^2-y^2}{y^2} \right| \right) (2\eta_a y) dy \\ &= \frac{2\eta_a}{\pi} x^3 \int_0^{1/2x} \left(t \ln \left| \frac{1+t}{1-t} \right| + t^2 \ln \left| \frac{1-t^2}{t^2} \right| \right) dt. \end{aligned}$$

We use L'Hopital's rule to compute the limit

$$\begin{aligned} \lim_{x \rightarrow +\infty} x^3 \int_0^{1/2x} \left(t \ln \left| \frac{1+t}{1-t} \right| + t^2 \ln \left| \frac{1-t^2}{t^2} \right| \right) dt &= \lim_{x \rightarrow +\infty} \frac{-\frac{1}{2x^2} \left(\frac{1}{2x} \ln \left| \frac{2x+1}{2x-1} \right| + \frac{1}{4x^2} \ln |4x^2 + 1| \right)}{-3x^{-4}} \\ &= \lim_{x \rightarrow +\infty} \frac{x}{12} \ln \left| \frac{2x+1}{2x-1} \right| + \lim_{x \rightarrow +\infty} \frac{1}{24} \ln |4x^2 + 1| = +\infty. \end{aligned}$$

This shows that $T(\omega)(x) \rightarrow +\infty$ as $x \rightarrow +\infty$. Note that the continuity of ω implies

$$T(\omega)(x) = \frac{1}{\pi} \int_0^{+\infty} \ln \left| \frac{x^2-y^2}{y^2} \right| \omega(y) dy$$

is continuous. Hence by the monotonicity of $T(\omega)$ and $T(\omega)(0) = 0$, there exists some $L_\omega > 0$ such that $T(\omega)(x) < r(\omega)/a$ for $x \in (0, L_\omega)$, and $T(\omega)(x) \geq r(\omega)/a$ for $x \geq L_\omega$, which implies that ω is compactly supported on $[-L_\omega, L_\omega]$. \square

7.2.3. Regularity. In this subsection we discuss the regularity of a solution $\omega(x)$ to the traveling wave profile equation (7.1) with $\omega \in \mathbb{D}_a$ being the fixed point of \mathbf{R}_a for some $a \in (-\infty, 0) \cup (0, 1)$. We shall always denote

$$g = \left(1 - \frac{aT(\omega)}{r(\omega)} \right)_+$$

in the sequel. Recall that

$$\omega(x) = \mathbf{R}_a(\omega)(x) = \left(1 - \frac{aT(\omega)(x)}{r(\omega)} \right)_+^{\frac{1}{a}},$$

which leads to

$$\omega'(x) = -\frac{T(\omega)'(x)}{r(\omega)} \left(1 - \frac{aT(\omega)(x)}{r(\omega)} \right)_+^{\frac{1}{a}-1} = -\frac{T(\omega)'(x)}{r(\omega)} \frac{\omega(x)}{g(x)}. \quad (7.8)$$

Since (7.7) yields $|\omega'(x)| \leq 2 \min\{x, x^{-1}\}$, it is not hard to check by formula (7.3) that $T(\omega) \in C^1(\mathbb{R})$, and thus $g \in C^1([-L_\omega, L_\omega])$, where

$$L_\omega = \sup\{x : g(x) > 0\} = \sup\{x : \omega(x) > 0\}.$$

Clearly $L_\omega \geq 1$ since $\omega(x) \geq (1-x^2)_+$, and $L_\omega = +\infty$ if ω is strictly positive on \mathbb{R} . Note that $\omega/g \in C([-L_\omega, L_\omega])$. We then obtain from (7.8) that $\omega(x) \in C^1([-L_\omega, L_\omega])$.

To obtain higher regularity of ω , we apply some boot-strapping technique.

Theorem 7.11. *Let $\omega \in \mathbb{D}_a$ be a fixed point of \mathbf{R}_a for some $a \in (-\infty, 0) \cup (0, 1)$. Denote $L = \sup\{x : f(x) > 0\}$. Then depending on the sign of a , one of the following happens:*

(1) $a < 0$: ω is strictly positive on \mathbb{R} , and $\omega' \in H^k(\mathbb{R})$ for any $k \geq 0$.

(2) $0 < a < 1$: ω is compactly supported on $[-L_\omega, L_\omega]$, and ω is smooth in the interior of $(-L_\omega, L_\omega)$.

Proof. (1): Note that in this case $\omega \leq 1$ and $g(x) \geq 1$ for $x \in [0, +\infty)$, which implies that ω and $1/g$ both belong to $L^\infty(\mathbb{R})$. Then, by (7.8) together with the well-known identity $\|T(\omega)''\|_{H^k(\mathbb{R})} = \|H(\omega')\|_{H^k(\mathbb{R})} = \|\omega'\|_{H^k(\mathbb{R})}$ for any integer $k \geq 0$, we see that $\omega' \in H^k(\mathbb{R})$ implies $\omega' \in H^{k+1}(\mathbb{R})$ for any $k \geq 0$. By (7.7), we have $|\omega'(x)| \leq 2 \min\{x, x^{-1}\}$, and hence $\omega' \in L^2(\mathbb{R})$. Therefore, by a standard induction argument, we conclude that $\omega' \in H^k(\mathbb{R})$ for every $k \geq 0$.

(2): In this case $g'(x) = -aT(\omega)'(x)/r(\omega) \leq 0$ for $x \in [0, L_\omega]$, then for any $0 < L' < L_\omega$, $g(x) \geq g(L') > 0$ for $x \in [-L', L']$. It follows straightforwardly from Lemma D.1 that if $\omega \in H_{loc}^k(-L', L')$ for some integer $k \geq 0$, then $\omega \in H_{loc}^{k+1}(-L', L')$. Since $\omega \in C^1([-L', L']) \subset H^1([-L', L'])$, we immediately obtain by recursion that $\omega \in H^k([-L', L'])$ for any integer $k \geq 0$. This further implies that $\omega \in H^k(-L_\omega, L_\omega)$ for any integer $k \geq 0$ since $L' < L$ is arbitrary, and thus ω is smooth in the interior of $(-L_\omega, L_\omega)$. \square

APPENDIX A. TRANSLATION INVARIANCE

The following lemma shows that solutions of the gCLM model with the same initial data but different choices of x_0 such that $u(x_0, t) = 0$ differ only by a time-dependent translation in x .

Lemma A.1. *Let ω_0 be some suitable initial data and x_1, x_2 be two continuous trajectories. Suppose that $(\omega_i, u_i)_{i=1,2}$ are the solutions to the gCLM model (1.1) with $u_i(x_i, t) = 0$, respectively, both starting from the same initial data ω_0 . Let $c(t)$ be a time-dependent quantity that satisfies the following ODE:*

$$c'(t) = -u_1(x_2 - c(t), t) = -\frac{1}{\pi} \ln \left| \frac{x_2 - c(t) - y}{x_1 - y} \right| \omega_1(y, t) dy,$$

Then it holds that

$$(\omega_2(x, t), u_2(x, t)) = (\omega_1(x - c(t), t), u_1(x - c(t), t) - u_1(x_2 - c(t), t)).$$

Proof. Recall that u is recovered from ω as

$$u(x, t) = \int_{x_0}^x H(\omega)(y, t) dy = \int_{\mathbb{R}} \ln \left| \frac{x - y}{x_0 - y} \right| \omega(y, t) dy. \quad (\text{A.1})$$

We only need to show that there is some time-dependent translation $c(t)$ such that

$$\omega_2(x, t) = \omega_1(x - c(t), t). \quad (\text{A.2})$$

In fact, if (A.2) holds, then by (A.1) we have

$$\begin{aligned} u_2(x, t) &= \frac{1}{\pi} \int_{\mathbb{R}} \ln \left| \frac{x - y}{x_2 - y} \right| \omega_2(y, t) dy \\ &= \frac{1}{\pi} \int_{\mathbb{R}} \ln \left| \frac{(x - c(t)) - (y - c(t))}{(x_2 - c(t)) - (y - c(t))} \right| \omega_1(y - c(t), t) dy \\ &= \frac{1}{\pi} \int_{\mathbb{R}} \ln \left| \frac{x - c(t) - y}{x_1 - y} \right| \omega_1(y, t) dy - \frac{1}{\pi} \ln \left| \frac{x_2 - c(t) - y}{x_1 - y} \right| \omega_1(y, t) dy \\ &= u_1(x - c(t), t) - u_1(x_2 - c(t), t). \end{aligned}$$

Substituting this into the gCLM equation for ω_2 and comparing it with that for ω_1 , we find that (A.2) holds provided that $c(t)$ satisfies the ODE

$$c'(t) = -u_1(x_2 - c(t), t) = -\frac{1}{\pi} \ln \left| \frac{x_2 - c(t) - y}{x_1 - y} \right| \omega_1(y, t) dy.$$

Note that $c(0) = 0$ since both solutions start from the same initial data. The existence and uniqueness of $c(t)$ then follows from the standard ODE theory. It is thus proved that solutions of the gCLM model with the same initial data but different choices of x_0 differ only by a time-dependent translation in x . \square

APPENDIX B. EXPLICIT SINGULAR SOLUTION TO THE PROFILE EQUATION WHEN $a < 0$

We verify that the explicit singular function given in Theorem 2.6 is a solution to the self-similar profile (2.8). Recall that for a fixed $a < 0$, the expressions of $(\bar{\Omega}_a, \bar{c}_{l,a}, \bar{c}_{\omega,a})$ are given by

$$\bar{\Omega}_a(X) = -\frac{\mathbf{1}_{\{X>1\}} \sin(\pi\mu)}{|1-X|^\mu}, \quad \bar{c}_{l,a} = 1-a, \quad \bar{c}_{\omega,a} = -1,$$

where $\mu = 1/(1-a) > 0$. Then the Hilbert transform of $\bar{\Omega}_a$ is

$$(\bar{U}_a)_X = \mathbf{H}(\bar{\Omega}_a)(X) = \frac{\mathbf{1}_{\{X<1\}} + \mathbf{1}_{\{X>1\}} \cos(\pi\mu)}{|1-X|^\mu}.$$

Proof of Theorem 2.6. We can calculate that for $X \neq 1$,

$$(\bar{\Omega}_a)_X(X) = \frac{\mu \mathbf{1}_{\{X>1\}} \sin(\pi\mu)}{|1-X|^{1+\mu}},$$

and for all $X \in \mathbb{R}$,

$$\begin{aligned} \bar{U}_a(X) &= \int_0^X (\bar{U}_a)_X(Y) dY = \frac{1}{1-\mu} + \frac{|1-X|^{1-\mu}}{1-\mu} (\mathbf{1}_{\{X>1\}} \cos(\pi\mu) - \mathbf{1}_{\{X<1\}}) \\ &= \frac{1}{1-\mu} + \frac{X-1}{1-\mu} (\bar{U}_a)_X(X). \end{aligned}$$

We then compute that

$$\begin{aligned} & -\bar{c}_{l,a}X(\bar{\Omega}_a)_X + \bar{c}_{\omega,a}\bar{\Omega}_a + (\bar{U}_a)_X\bar{\Omega}_a - a\bar{U}_a(\bar{\Omega}_a)_X \\ &= -\bar{c}_{l,a}X \cdot \frac{\mu \mathbf{1}_{\{X>1\}} \sin(\pi\mu)}{|1-X|^{1+\mu}} - \bar{c}_{\omega,a} \cdot \frac{\mathbf{1}_{\{X>1\}} \sin(\pi\mu)}{|1-X|^\mu} - \frac{\mathbf{1}_{\{X>1\}} \sin(\pi\mu) \cos(\pi\mu)}{|1-X|^{2\mu}} \\ & \quad + \frac{\mathbf{1}_{\{X>1\}} \sin(\pi\mu)}{|1-X|^{1+\mu}} + \frac{\mathbf{1}_{\{X>1\}} \sin(\pi\mu) \cos(\pi\mu)}{|1-X|^{2\mu}} \\ &= (-\bar{c}_{l,a}\mu X - \bar{c}_{\omega,a}(X-1) + 1) \frac{\mathbf{1}_{\{X>1\}} \sin(\pi\mu)}{|1-X|^{1+\mu}} \\ &= 0. \end{aligned}$$

Therefore, $(\bar{\Omega}_a, \bar{c}_{l,a}, \bar{c}_{\omega,a})$ exactly solves the self-similar profile equation (2.8) for all $a < 0$. \square

APPENDIX C. DETAILS OF THE NUMERICAL IMPLEMENTATION

C.1. Numerical method for computing the Hilbert transform and its integral. Here we describe the numerical method we use for computing the Hilbert transform $\mathbf{H}(f)(x)$ for a given function f . We approximate f on the computing domain $[-M, M]$ using cubic splines as

$$f(x) = f_i P_i(x) + f_{i+1} P_{i+1}(x) + f'_i Q_i(x) + f'_{i+1} Q_{i+1}(x), \quad x \in [x_i, x_{i+1}), \quad (\text{C.1})$$

where $\{x_i\}_{i=0}^N$ is the grid points with $x_0 = -M$, $x_N = M$, f_i are the function values at the grid points, and

$$P_i(x) = \left(1 + 2\frac{x-x_i}{x_{i-1}-x_i}\right) \left(\frac{x-x_{i-1}}{x_i-x_{i-1}}\right)^2 \mathbf{1}_{\{x_{i-1} \leq x < x_i\}} + \left(1 + 2\frac{x-x_i}{x_{i+1}-x_i}\right) \left(\frac{x-x_{i+1}}{x_i-x_{i+1}}\right)^2 \mathbf{1}_{\{x_i \leq x < x_{i+1}\}},$$

$$Q_i(x) = (x-x_i) \left(\frac{x-x_{i-1}}{x_i-x_{i-1}}\right)^2 \mathbf{1}_{\{x_{i-1} \leq x < x_i\}} + (x-x_i) \left(\frac{x-x_{i+1}}{x_i-x_{i+1}}\right)^2 \mathbf{1}_{\{x_i \leq x < x_{i+1}\}}$$

are sum of the Hermite basis functions on $[x_{i-1}, x_i]$ and $[x_i, x_{i+1}]$. We consider P_i, Q_i rather than the standard Hermite basis functions since they are C_0^1 functions, which makes their Hilbert transforms bounded. The derivatives on the grid points f'_i are computed using the standard cubic spline method with end conditions $f''(x_0) = f''(x_N) = 0$. Then for each P_i, Q_i , we compute their Hilbert transforms analytically. We have

$$H(P_i)(x) = A(l) - A(r), \quad H(Q_i)(x) = (x_{i-1} - x_i)B(l) - (x_{i+1} - x_i)B(r),$$

where

$$l = \frac{x_{i-1} - x_i}{x - x_i}, \quad r = \frac{x_{i+1} - x_i}{x - x_i},$$

$$A(s) = \frac{-5s^3 - 12s^2 + 12s + 6(s^3 - 3s + 2) \ln |1 - s|}{6\pi s^3}, \quad B(s) = \frac{2s^3 - 9s^2 + 6s + 6(s-1)^2 \ln |1 - s|}{6\pi s^3}.$$

Note that when $s \rightarrow 0$ $A(s)$ tends to 0, while

$$\frac{-5s^3 - 12s^2 + 12s}{6\pi s^3}, \quad \frac{6(s-1)^2 \ln |1 - s|}{6\pi s^3}$$

both tend to ∞ , and such behavior would lead to large numerical errors introduced by cancellation. Hence to compute $A(s)$ and $B(s)$ accurately when s is close to 0, we use the following minimax approximation for $(s-1)(\ln |1-s| + s + s^2/2 + s^3/3)/s^4$ on $[-0.5, 0.5]$ computed by Mathematica 14.2:

$$\frac{(s-1) \left(\ln |1-s| + s + \frac{s^2}{2} + \frac{s^3}{3} \right)}{s^4} \approx R_1(s)$$

$$= 0.25 - 0.049999999999999866s - 0.0333333333333338085s^2 - 0.02380952381002668s^3$$

$$- 0.01785714284817429s^4 - 0.01388888883280194s^5 - 0.0111111117723456s^6$$

$$- 0.00909091199993801s^7 - 0.007575732470825958s^8 - 0.006410171819766842s^9$$

$$- 0.005495065477419788s^{10} - 0.004763424514296551s^{11} - 0.0041587945938036s^{12}$$

$$- 0.003658683032021482s^{13} - 0.003340203914467509s^{14} - 0.00306305502520356s^{15}$$

$$- 0.002195292685440593s^{16} - 0.001652974757186405s^{17} - 0.003865944631093168s^{18}$$

$$- 0.004466133542538447s^{19} + 0.002210270189446115s^{20} + 0.003532901236598389s^{21}$$

$$- 0.006394622541761529s^{22} - 0.006964811435003471s^{23}$$

with a maximum absolute error $2.011826942268783 \times 10^{-16}$. Using this approximation we can compute $A(s)$ and $B(s)$ accurately for $s \in [-0.5, 0.5]$:

$$A(s) \approx -\frac{3s^2 + 2s^3}{6\pi} + \frac{-2s + s^2 + s^3}{\pi} R_1(s), \quad B(s) \approx \frac{s - 2s^2}{6\pi} + \frac{-s + s^2}{\pi} R_1(s).$$

Finally, for the grid point x_i , both l and r tend to infinity, hence we need to compute the limit explicitly. By taking the limit $x \rightarrow x_i$ yields

$$\mathbf{H}(P_i)(x_i) = \frac{1}{\pi} \ln \left| \frac{x_{i-1} - x_i}{x_{i+1} - x_i} \right|, \quad \mathbf{H}(Q_i)(x_i) = \frac{x_{i-1} - x_{i+1}}{3\pi}$$

for $i = 1, 2, \dots, N - 1$. Using the above formulas we can compute $\mathbf{H}(f)(x_i)$ for any grid point $x_i \in [-M, M]$ accurately.

To compute the integral of the Hilbert transform, we still use the cubic spline approximation (C.1) for f and integrate $\mathbf{H}(P_i)(x)$ and $\mathbf{H}(Q_i)(x)$ analytically:

$$\begin{aligned} (-\Delta)^{-1/2} P_i(x) &= \int \mathbf{H}(P_i)(x) dx = C(x_i - x_{i-1}, l) + C(x_{i+1} - x_i, r), \\ (-\Delta)^{-1/2} Q_i(x) &= \int \mathbf{H}(Q_i)(x) dx = D(x_i - x_{i-1}, l) - D(x_{i+1} - x_i, r), \end{aligned}$$

where

$$\begin{aligned} C(d, s) &= \frac{d \left(-19s^4 + 8s^3 + 18s^2 - 12s + (12s^4 - 24s^3 + 24s - 12) \ln |1 - s| + 12s^4 \ln \left| \frac{d}{s} \right| \right)}{24\pi s^4}, \\ D(d, s) &= \frac{d^2 \left(13s^4 + 36s^3 - 78s^2 + 36s + (-12s^4 + 72s^2 - 96s + 36) \ln |1 - s| - 12s^4 \ln \left| \frac{d}{s} \right| \right)}{144\pi s^4}. \end{aligned}$$

For s close to 0, we use the minimax approximation for $(s - 1)^3 (\ln |1 - s| + s + s^2/2 + s^3/3)/s^4$ on $[-0.5, 0.5]$ computed by Mathematica 14.2:

$$\begin{aligned} \frac{(s - 1)^3 \left(\ln |1 - s| + s + \frac{s^2}{2} + \frac{s^3}{3} \right)}{s^4} &\approx R_2(s) \\ &= 0.25 - 0.55000000000000005s + 0.31666666666666673s^2 - 0.007142857142718389s^3 \\ &\quad - 0.003571428571658581s^4 - 0.001984126996758493s^5 - 0.001190476169455116s^6 \\ &\quad - 0.0007575752302443226s^7 - 0.0005050513541658974s^8 - 0.0003496624830794595s^9 \\ &\quad - 0.0002497317240860826s^{10} - 0.0001829814020322089s^{11} - 0.0001376024384624091s^{12} \\ &\quad - 0.0001065281770442371s^{13} - 0.00007978095495689995s^{14} - 0.00005609995868764908s^{15} \\ &\quad - 0.00006109725530208673s^{16} - 0.00007171425465849955s^{17} \\ &\quad - 6.388916781803325 \times 10^{-6}s^{18} + 0.00003490077048616611s^{19} \\ &\quad - 0.00006504398511532267s^{20} - 0.0000856727088008827s^{21} \end{aligned}$$

with a maximum absolute error $4.143007531279983 \times 10^{-17}$. Then we can compute $C(d, s)$ and $D(d, s)$ accurately for $s \in [-0.5, 0.5]$:

$$\begin{aligned} C(d, s) &\approx \frac{d \left(-3 + 2s^2 - 4s^3 + 12 \ln \left| \frac{d}{s} \right| \right)}{24\pi} + \frac{d(1 + s)}{2\pi} R_2(s), \\ D(d, s) &\approx \frac{d^2 \left(9 - 12s + 6s^2 + 4s^3 - 12 \ln \left| \frac{d}{s} \right| \right)}{144\pi} - \frac{d^2(3 + s)}{12\pi} R_2(s). \end{aligned}$$

For the grid point x_i , taking the limit $x \rightarrow x_i$ yields

$$\begin{aligned} (-\Delta)^{-1/2} P_i(x_i) &= \frac{-19(d_1 + d_2) + 12d_1 \ln d_1 + 12d_2 \ln d_2}{24\pi}, \\ (-\Delta)^{-1/2} Q_i(x_i) &= \frac{13d_1^2 - 13d_2^2 - 12d_1^2 \ln d_1 + 12d_2^2 \ln d_2}{144\pi}, \end{aligned}$$

where $d_1 = x_i - x_{i-1}$, $d_2 = x_{i+1} - x_i$.

C.2. Numerical method for simulating the dynamic rescaling equation. Here we describe our numerical approach for solving the dynamic rescaling equation (2.7). To prevent round-off and discretization errors from degrading the prescribed high-order vanishing of the solution at the origin, we evolve

$$f(X, \tau) = \frac{\Omega(X, \tau)}{X^k}$$

instead of Ω itself, where $k \geq 3$ is an odd integer. Substituting $\Omega = X^k f$ into (2.7) gives

$$f_\tau + (c_l X + aU) f_X = \left(c_\omega + U_X - k \left(c_l + a \frac{U}{X} \right) \right) f.$$

The choice of k depends on the sign of a . For $a > 0$, we choose k to match the vanishing order of the initial data. For $a < 0$, we fix $k = 3$, since the computations in Section 5 indicate that the evolving profile develops infinite vanishing order at the origin, provided the initial data vanish to order at least 3. The velocity U and its derivative U_X are computed from $\Omega = X^k f$ using the method described in Appendix C.1. We discretize the advection term $(c_l X + aU) f_X$ using a fifth-order WENO scheme [JW99] and advance in time with the ten-stage, fourth-order Strong Stability Preserving Runge–Kutta method SSPRK(10, 4) [GKS11].

For $a > 0$, the convergence criterion is set as $\|f_\tau\|_{L^\infty} < 10^{-8}$. For $a < 0$, since the profile becomes singular at $X = 1$ under our normalization conditions, we exclude the neighborhood of the singularity from the convergence criterion and use

$$\|f_\tau \mathbf{1}_{\{0 \leq X < 0.9 \text{ or } X > 1.1\}}\|_{L^\infty} < 10^{-8}.$$

In Section 6, to better resolve the developing singularity for $a < 0$, we use an adaptive mesh refinement strategy. The grid points X are generated from a uniformly discretized computational coordinate $\rho \in [0, \rho_{\max}]$ via

$$X(\rho) = X_m(1 - \cosh \rho) + \sqrt{c + X_m^2} \sinh \rho,$$

where X_m denotes the location where $|\Omega|$ attains its maximum. The parameter c controls the mesh concentration near X_m and is chosen so that $N_{\text{bulk}} = 600$ grid points lie in the interval $[X_1, X_2]$ capturing the thin peak of the solution, defined by

$$|\Omega(X_1)| = |\Omega(X_2)| = 0.5 \|\Omega\|_{L^\infty}.$$

We truncate the domain at $M = 10^{10}$ by choosing ρ_{\max} such that $X(\rho_{\max}) = M$, and we use a uniform step size $\Delta\rho = 0.01$. During the evolution, we track X_m and the width of the thin peak $X_2 - X_1$. We regenerate the mesh and interpolate the solution onto the new grid using cubic splines whenever (i) X_m drifts by more than 25% of the current width of the thin peak, or (ii) the width shrinks by more than 50%. For the $a > 0$ case (Section 4), the profile remains smooth, so we use a fixed mesh generated by the same procedure, with $X_1 = 0.99$, $X_2 = 1.01$, and $X_m = 1$ chosen manually. In Section 5, we focus on the outer profile and do not explicitly zoom in near the singularity at $X = 1$; accordingly, we again use a fixed mesh generated from the initial data, and rely on the WENO5 discretization to capture the sharp front near $X = 1$.

C.3. The iterative method for computing the traveling wave profile. Recall the nonlinear operator R_a introduced in Section 7:

$$R_a(\omega)(x) = \left(1 - \frac{aT(\omega)(x)}{r(\omega)}\right)_+^{\frac{1}{a}},$$

where

$$T(\omega)(x) = \frac{1}{\pi} \int_0^{+\infty} \ln \left| \frac{x^2 - y^2}{y^2} \right| \omega(y) dy, \quad r(\omega) = \frac{1}{\pi} \int_0^{+\infty} \frac{\omega(0) - \omega(y)}{y^2} dy.$$

By Proposition 7.1, any fixed point of R_a corresponds to a traveling-wave profile of the gCLM model. To compute such a profile numerically, we apply the fixed-point iteration

$$\omega^{(n+1)} = R_a(\omega^{(n)}), \quad n = 0, 1, 2, \dots,$$

initialized with

$$\omega^{(0)}(x) = \frac{1}{1+x^2}.$$

At each step, the operator $T(\omega)$ is evaluated using the method described in Appendix C.1. The iteration is terminated once the increment satisfies

$$\|\omega^{(n+1)} - \omega^{(n)}\|_{L^\infty(\mathbb{R})} < 10^{-8}.$$

APPENDIX D. ON THE HILBERT TRANSFORM

Lemma D.1. *Given a function ω , suppose that $\|x^\delta \omega\|_{L^\infty(\mathbb{R})} = \sup_{x \in \mathbb{R}} |x|^\delta |\omega(x)| < +\infty$ for some $\delta > 0$. If $\omega \in H_{loc}^k(A, B)$ for some $A < B$ and some integer $k \geq 0$, then $\mathbf{H}(\omega) \in H_{loc}^k(A, B)$.*

Proof. We first prove a formula for the k -th derivative of the Hilbert transform $\mathbf{H}(\omega)$. If $\omega \in H_{loc}^k(A, B)$, then for any $A < a < b < B$ and any $x \in (a, b)$,

$$\mathbf{H}(\omega)^{(k)}(x) = \mathbf{H}(\mathbf{1}_{\{a \leq x \leq b\}} \omega^{(k)})(x) + g_{a,b}^{(k)}(x) + \sum_{j=0}^{k-1} f_{a,b,j}^{(k-j)}(x), \quad (\text{D.1})$$

where the summation is 0 if $k = 0$, and

$$\begin{aligned} \mathbf{H}(\mathbf{1}_{\{a \leq x \leq b\}} \omega^{(k)})(x) &= \frac{1}{\pi} P.V. \int_a^b \frac{\omega^{(k)}(y)}{x-y} dy, \\ g_{a,b}(x) &= \frac{1}{\pi} \int_{-\infty}^a \frac{\omega(y)}{x-y} dy + \frac{1}{\pi} \int_b^{+\infty} \frac{\omega(y)}{x-y} dy, \\ f_{a,b,j}(x) &:= \frac{1}{\pi} \left(\omega^{(j)}(a) \ln|x-a| - \omega^{(j)}(b) \ln|x-b| \right), \quad j = 0, 1, 2, \dots \end{aligned}$$

We prove this formula by induction. The base $k = 0$ is trivial:

$$\mathbf{H}(\omega)(x) = \frac{1}{\pi} P.V. \int_{-\infty}^{+\infty} \frac{\omega(y)}{x-y} dy = \frac{1}{\pi} \int_a^b \frac{\omega(y)}{x-y} dy + g_{a,b}(x).$$

Now suppose that (D.1) holds for some integer $k \geq 0$, we need to show that it is then also true for $k + 1$. Under the assumption that $\omega \in H_{loc}^{k+1}(A, B)$, we can use integration by parts to rewrite the first

term on the right-hand side of (D.1) as

$$\begin{aligned} \mathbf{H}(\mathbf{1}_{\{a \leq x \leq b\}} \omega^{(k)})(x) &= \frac{1}{\pi} P.V. \int_a^b \frac{\omega^{(k)}(y)}{x-y} dy \\ &= -\frac{1}{\pi} \omega^{(k)}(y) \ln|x-y| \Big|_{y=a}^{y=b} + \frac{1}{\pi} \int_a^b \omega^{(k+1)}(y) \ln|x-y| dy \\ &= f_{a,b,k}(x) + \frac{1}{\pi} \int_a^b \omega^{(k+1)}(y) \ln|x-y| dy. \end{aligned}$$

Note that $\omega^{(k)}(a)$ and $\omega^{(k)}(b)$ are finite since $\omega \in H_{loc}^{k+1}(A, B)$. It then follows from the induction hypothesis that, for $x \in (a, b)$,

$$\begin{aligned} \mathbf{H}(\omega)^{(k+1)}(x) &= \left(\mathbf{H} \left(\mathbf{1}_{\{a \leq x \leq b\}} \omega^{(k)} \right) (x) \right)' + \left(g_{a,b}^{(k)}(x) + \sum_{j=0}^{k-1} f_{a,b,j}^{(k-j)}(x) \right)' \\ &= f'_{a,b,k}(x) + \frac{1}{\pi} P.V. \int_a^b \frac{\omega^{(k+1)}(y)}{x-y} dy + g_{a,b}^{(k+1)}(x) + \sum_{j=0}^{k-1} f_{a,b,j}^{(k+1-j)}(x) \\ &= \frac{1}{\pi} P.V. \int_a^b \frac{\omega^{(k+1)}(y)}{x-y} dy + g_{a,b}^{(k+1)}(x) + \sum_{j=0}^k f_{a,b,j}^{(k+1-j)}(x). \end{aligned}$$

Hence (D.1) holds for $k+1$. This completes the induction.

We then use (D.1) to prove the lemma. Note that under the assumptions of the lemma, it is easy to see that $g_{a,b}(x)$ and $f_{a,b,j}(x)$, $j = 0, 1, \dots, k-1$, are infinitely smooth in the interior of (a, b) , and thus $g_{a,b}, f_{a,b,j} \in H_{loc}^k(A, B)$. As for the first term on the right-hand side of (D.1), we have

$$\left\| \mathbf{H} \left(\mathbf{1}_{\{a \leq x \leq b\}} \omega^{(k)} \right) \right\|_{L^2([a,b])} \leq \left\| \mathbf{H} \left(\mathbf{1}_{\{a \leq x \leq b\}} \omega^{(k)} \right) \right\|_{L^2(\mathbb{R})} = \left\| \mathbf{1}_{\{a \leq x \leq b\}} \omega^{(k)} \right\|_{L^2(\mathbb{R})} = \|\omega\|_{\dot{H}^k([a,b])} < +\infty.$$

Therefore, (D.1) implies that $\mathbf{H}(\omega)^{(k)} \in H_{loc}^k(A, B)$. Since this is true for any $A < a < b < B$, we immediately have $\mathbf{H}(\omega)^{(k)} \in H_{loc}^k(A, B)$. \square

Acknowledgement. The authors are supported by the National Key R&D Program of China under the grant 2021YFA1001500. DH and XW are also supported by the National Natural Science Foundation of China under the grant NSFC No. 12288101.

REFERENCES

- [CC09] A. Castro and D. Córdoba. Self-similar solutions for a transport equation with non-local flux. *Chinese Annals of Mathematics, Series B*, 30(5):505–512, 2009.
- [CGMN23] C. Collot, T.-E. Ghoul, N. Masmoudi, and V. T. Nguyen. Collapsing-ring blowup solutions for the Keller–Segel system in three dimensions and higher. *Journal of Functional Analysis*, 285(7):110065, 2023.
- [CH22] J. Chen and T. Y. Hou. Stable nearly self-similar blowup of the 2D Boussinesq and 3D Euler equations with smooth data. *arXiv preprint arXiv:2210.07191*, 2022.
- [CH25] J. Chen and T. Y. Hou. Singularity formation in 3D Euler equations with smooth initial data and boundary. *Proceedings of the National Academy of Sciences*, 122(27):e2500940122, 2025.
- [Che20] J. Chen. Singularity formation and global well-posedness for the generalized Constantin–Lax–Majda equation with dissipation. *Nonlinearity*, 33(5):2502, 2020.
- [CHH21] J. Chen, T. Y. Hou, and D. Huang. On the finite time blowup of the De Gregorio model for the 3D Euler equations. *Communications on pure and applied mathematics*, 74(6):1282–1350, 2021.

- [CHH22] J. Chen, T. Y. Hou, and D. Huang. Asymptotically self-similar blowup of the Hou–Luo model for the 3D Euler equations. *Annals of PDE*, 8(2):24, 2022.
- [CLM85] P. Constantin, P. D. Lax, and A. Majda. A simple one-dimensional model for the three-dimensional vorticity equation. *Communications on pure and applied mathematics*, 38(6):715–724, 1985.
- [CMZZ25] D. Córdoba, L. Martínez-Zoroa, and F. Zheng. Finite time singularities to the 3D incompressible Euler equations for solutions in $C^\infty(\mathbb{R}^3 \setminus \{0\}) \cap C^{1,\alpha} \cap L^2$. *Annals of PDE*, 11(2):19, 2025.
- [DG90] S. De Gregorio. On a one-dimensional model for the three-dimensional vorticity equation. *Journal of statistical physics*, 59(5):1251–1263, 1990.
- [DG96] S. De Gregorio. A partial differential equation arising in a 1D model for the 3D vorticity equation. *Mathematical methods in the applied sciences*, 19(15):1233–1255, 1996.
- [dPLM⁺20] M. del Pino, C.-C. Lai, M. Musso, J. Wei, and Y. Zhou. New type II finite time blow-up for the energy supercritical heat equation. *arXiv preprint arXiv:2006.00716*, 2020.
- [dPMWZ20] M. del Pino, M. Musso, J. Wei, and Y. Zhou. Type II finite time blow-up for the energy critical heat equation in \mathbb{R}^4 . *Discrete Contin. Dyn. Syst*, 40(6):3327–3355, 2020.
- [EGM21] T. M. Elgindi, T.-E. Ghouli, and N. Masmoudi. Stable self-similar blow-up for a family of nonlocal transport equations. *Analysis & PDE*, 14(3):891–908, 2021.
- [EJ20] T. M. Elgindi and I.-J. Jeong. On the effects of advection and vortex stretching. *Archive for Rational Mechanics and Analysis*, 235(3):1763–1817, 2020.
- [Elg21] T. M. Elgindi. Finite-time singularity formation for $C^{1,\alpha}$ solutions to the incompressible Euler equations on \mathbb{R}^3 . *Annals of Mathematics*, 194(3):647–727, 2021.
- [GKS11] S. Gottlieb, D. I. Ketcheson, and C.-W. Shu. *Strong stability preserving Runge–Kutta and multistep time discretizations*. World Scientific, 2011.
- [HH22] T. Y. Hou and D. Huang. A potential two-scale traveling wave singularity for 3D incompressible Euler equations. *Physica D: Nonlinear Phenomena*, 435:133257, 2022.
- [HQW25] D. Huang, X. Qin, and X. Wang. Multiscale self-similar finite-time blowups of the Constantin–Lax–Majda model for the three-dimensional Euler equations. *SIAM Journal on Mathematical Analysis*, 57(4):4068–4096, 2025.
- [HQWW24] D. Huang, X. Qin, X. Wang, and D. Wei. Self-similar finite-time blowups with smooth profiles of the generalized Constantin–Lax–Majda model. *Archive for Rational Mechanics and Analysis*, 248(2):22, 2024.
- [HTW23] D. Huang, J. Tong, and D. Wei. On self-similar finite-time blowups of the De Gregorio model on the real line. *Communications in Mathematical Physics*, 402(3):2791–2829, 2023.
- [JW99] G.-S. Jiang and C.-c. Wu. A high-order WENO finite difference scheme for the equations of ideal magnetohydrodynamics. *Journal of Computational Physics*, 150(2):561–594, 1999.
- [LPSS88] M. J. Landman, G. C. Papanicolaou, C. Sulem, and P.-L. Sulem. Rate of blowup for solutions of the nonlinear Schrödinger equation at critical dimension. *Physical Review A*, 38(8):3837, 1988.
- [LSS21] P. M. Lushnikov, D. A. Silantyev, and M. Siegel. Collapse versus blow-up and global existence in the generalized Constantin–Lax–Majda equation. *Journal of Nonlinear Science*, 31(5):1–56, 2021.
- [MPSS86] D. W. McLaughlin, G. C. Papanicolaou, C. Sulem, and P.-L. Sulem. Focusing singularity of the cubic Schrödinger equation. *Physical Review A*, 34(2):1200, 1986.
- [OSW08] H. Okamoto, T. Sakajo, and M. Wunsch. On a generalization of the Constantin–Lax–Majda equation. *Nonlinearity*, 21(10):2447, 2008.

- [WBM⁺25] Y. Wang, M. Bennani, J. Martens, S. Racanière, S. Blackwell, A. Matthews, S. Nikolov, G. Cao-Labora, D. S. Park, M. Arjovsky, et al. Discovery of unstable singularities. *arXiv preprint arXiv:2509.14185*, 2025.
- [WLGSB23] Y. Wang, C.-Y. Lai, J. Gómez-Serrano, and T. Buckmaster. Asymptotic self-similar blow-up profile for three-dimensional axisymmetric Euler equations using neural networks. *Physical Review Letters*, 130(24):244002, 2023.
- [Zhe23] F. Zheng. Exactly self-similar blow-up of the generalized De Gregorio equation. *Nonlinearity*, 2023.